

May 2018

Studies in Gravitational-wave Astronomy and Tests of General Relativity

Hong Qi

University of Wisconsin-Milwaukee

Follow this and additional works at: <https://dc.uwm.edu/etd>

 Part of the [Astrophysics and Astronomy Commons](#), and the [Physics Commons](#)

Recommended Citation

Qi, Hong, "Studies in Gravitational-wave Astronomy and Tests of General Relativity" (2018). *Theses and Dissertations*. 1901.
<https://dc.uwm.edu/etd/1901>

This Dissertation is brought to you for free and open access by UWM Digital Commons. It has been accepted for inclusion in Theses and Dissertations by an authorized administrator of UWM Digital Commons. For more information, please contact open-access@uwm.edu.

STUDIES IN GRAVITATIONAL-WAVE ASTRONOMY AND TESTS OF
GENERAL RELATIVITY

by

Hong Qi

A DISSERTATION SUBMITTED IN
PARTIAL FULFILLMENT OF THE
REQUIREMENTS FOR THE DEGREE OF

DOCTOR OF PHILOSOPHY
IN PHYSICS

at

The University of Wisconsin–Milwaukee
May 2018

ABSTRACT

STUDIES IN GRAVITATIONAL-WAVE ASTRONOMY AND TESTS OF GENERAL RELATIVITY

by
Hong Qi

The University of Wisconsin–Milwaukee, May 2018
Under the Supervision of Professor Patrick Brady

Modern astronomical data sets provide the opportunity to test our physical theories of the Universe at unprecedented levels of accuracy. This dissertation examines approaches to testing gravitational theories using a) observations of stars orbiting the center of the Milky Way; b) observations of the pulsations of Cepheid variable stars in dwarf galaxies; and c) gravitational-wave observations of compact binary mergers.

Observations of stars orbiting the center of the Milky Way have been used to infer the mass of the putative black hole that exists there. I discuss how well present and future measurements of stellar orbits can constrain the black hole properties: both its mass and its spin. Specifically, I used a Markov-Chain Monte Carlo (MCMC) code to compare real and synthetic astrometric and radial velocity data with models for the stellar orbits and black hole mass, accounting for differences in reference frame between different observational campaigns. Unlike previous investigations, our model includes leading order post-Newtonian corrections to the orbit from the black hole's mass, spin, and quadrupole moment, as well as the impact of unknown non-quadrupole internal and exterior potentials. I present strategies for future observations to measure the Galactic Center black hole spin and even the black hole No-hair Theorem.

Chameleon field theory is one of the attempts to explain the observed acceleration of our universe. I demonstrate the testing of chameleon field theory on stellar structure scales with the distance indicator Cepheid variable stars. Using the numerical results obtained for the evolutions of stars from MESA, I calculate the pulsation rates of Cepheid variable stars with both the theory of general relativity (GR) and the chameleon field

theory. I find that the period-temperature relation is not that simple as we previously thought, which assumed that the equivalent effect of a chameleon field is an enhancement of gravity and should result in faster pulsations of the Cepheids. I discuss strategies to use observations of Cepheids to test chameleon fields.

The first direct detection of gravitational waves was made on Sep 14, 2015 by the two advanced detectors of the Laser Interferometer Gravitational-wave Observatory (LIGO). The waves came from the coalescence of a binary black hole (BBH) system. Since then, the LIGO-Virgo Collaboration's (LVC) has reported multiple detections of binary black hole mergers. On August 17, 2017 a binary neutron star (BNS) merger was detected by LIGO and Virgo. Subsequently, an electromagnetic (EM) counterpart was observed in the host galaxy NGC4993. The unprecedented event provides brand new insights into astrophysics and cosmology. I present an approach to using gravitational waves to measure the expansion of the Universe. The methods have been tested in end-to-end simulations of the gravitational-wave analysis chain. After we detected the BNS and its EM counterpart, I applied my tools on the event and constrained H_0 . I also present studies of the statistical method of measuring H_0 carried out in collaboration with the LVC Cosmology group.

TABLE OF CONTENTS

1	Introduction	1
1.1	General Relativity and Gravitational Waves	2
1.1.1	Linearized gravity	3
1.1.2	Gravitational waves: solution to linearized Einstein field equations	4
1.1.3	Sources of gravitational waves	6
1.2	Dissertation Outline	8
2	Constrain the Relativity and Astrophysics with Galactic Center Stellar Orbits: Calibrating A Fisher Matrix Method Against Markov Chain Monte Carlo	10
2.1	Introduction	10
2.2	Statement of the problem	12
2.2.1	What do astronomers observe	12
2.2.2	Simplified models of stellar orbits	13
2.2.3	Relationship between real observation and theoretical model . . .	14
2.3	Measuring parameters	17
2.3.1	Bayesian formalism	17
2.3.2	Fisher matrix	18
2.3.3	Results on the real data	20
2.4	Testing various Hypotheses	23
2.4.1	Bayesian hypothesis selection	23
2.4.2	Does the Galactic center BH have spin	23
2.4.3	No-hair theorem	26
2.5	Conclusions	29
	Appendix 2.A Equations of motion	30
	2.A.1 Post-Newtonian Two-body equations of motion	30

2.A.2	Post-Newtonian N-body equations of motion	32
Appendix 2.B	Fisher matrix for Newtonian orbits	32
2.B.1	Fisher matrix for Keplerian orbits	32
2.B.2	Unknown black hole mass	35
2.B.3	Unknown black hole spin	35
Appendix 2.C	Likelihood and MCMC	37
2.C.1	Bayesian formalism	37
2.C.2	Fisher matrix	38
2.C.3	Toy model: tests in \vec{r} using MCMC	40
3	Testing Chameleon Field Theory with Cepheids in Extragalactic Dwarf Galaxies	41
3.1	Introduction	41
3.1.1	History of the Problem	41
3.1.2	Chameleon Field Theory	42
3.1.3	Cepheid Pulsations in GR	42
3.2	Methods	43
3.2.1	Building Stars in Chameleon Gravity	43
3.2.2	Radial Pulsations in Chameleon Gravity	44
3.3	Results	45
3.3.1	Stellar Structures in GR and MG	45
3.3.2	Eigenmodes of a Cepheid in GR and MG	45
3.3.3	Comparison with JVS ansatz	47
3.3.4	Effects of metallicity	50
3.4	Discussions	51
Appendix 3.A	Matrix Method	51
4	Determining Hubble Constant With Gravitational-wave and Electromagnetic Observations	57
4.1	Introduction	57

4.2	Methodology	60
4.2.1	Single observation	61
4.2.2	Multiple observations	62
4.2.3	Prior	62
4.3	Mock Data Challenge	64
4.3.1	Simulation	64
4.3.2	Found injections	65
4.3.3	Galaxy catalogs	66
4.3.4	Combined H_0 posterior	67
4.4	Results with electromagnetic counterparts for GW170817	70
4.5	H_0 statistical results for GW170817	71
5	Conclusions	75
5.1	Summary	75
5.2	Future Work	77
	Curriculum Vitae	84

LIST OF FIGURES

1	A ring of freely-falling test particles is affected as shown for a purely plus and a purely cross polarized gravitational waves, traveling into the page. The diagram shows snapshot at a quarter of period intervals.	5
2	A chirp waveform as a function of time is shown. Credit: https://www.ligo.org/science/GW-Inspiral.php	7
3	Relative magnitude of different effects: A plot of different characteristic rates of change for stellar orbits around supermassive black holes, versus semilatus rectum. Solid curves show analytic results; dotted curves were derived from our time-domain evolution code, as validation. The solid green, blue, an purple curves show A_S, A_J, A_Q implicitly defined in Eq. (2.2.2). The cyan curves show the influence of an external quadrupolar potential from ambient stars at a distance of 30 kilo-masses of black hole.	15
4	The figure shows the marginalized posteriors of dimensionless spin $\chi = J/M^2$ with different injected values χ_{inj} and their corresponding quadruple variables $Q_2 = -J_{inj}^2/M$. The range of spin J is $[0, M^2]$, where $M = 1.15M_*$ and $M_* = 4.0 \times 10^6 M_\odot$. The measurement uncertainties $\{\sigma_{\Delta\alpha} = \sigma_{\Delta\delta} = 10 \mu as, \sigma_{v_r} = 500 m/s\}$ are the limit of GRAVITY at the distance of 8 kpc. The star has an S2-ish orbit and is observed once per day for an entire orbit of 16 years.	24
5	Peak value and 90% credible interval as a function of injected dimensionless spin χ_{inj} for the best achievable measurement accuracies of GRAVITY using Galactic center orbits in the near future with $\{\sigma_{\Delta\alpha} = \sigma_{\Delta\delta} = 10 \mu as, \sigma_{v_r} = 500 m/s\}$. Dots show the maxima of posterior estimates of χ ; bars indicate the 90% confidence interval.	25



- 6 The top figure shows the marginalized posteriors of quadrupole Q_2 with different injected values χ_{inj} and their corresponding injected quadruple values $Q_{2,inj} = -\chi_{inj}^2 M^3$, where $M = 1.2M_*$. The bottom figure shows the posteriors of dimensionless spin χ for different injected values of χ . The measurement uncertainties are $\{\sigma_{\Delta\alpha} = \sigma_{\Delta\delta} = 10 \mu as, \sigma_{v_r} = 500 m/s\}$. The star has an orbit that is half the semi-major axis of S2 and the other parameters the same. It is observed once per week for an entire orbit of 300 weeks. 28
- 7 Measuring properties of an orbit and a BH: circular orbits: *Top panel:* Demonstration of how accurately a Newtonian circular orbits' radius can be measured, assuming the only unknown parameter is the orbital radius (black) and assuming no parameters are known (blue). For comparison, the dotted curves show the results of our Fisher matrix calculations. This figure uses simplified measurement model of Eq. (2.C.1), with $a = 2800M, N = 700, \sigma_r = 1.0M, e = 0.01, T = 100 weeks, \Delta t = 1 day$. *Bottom panel:* Demonstration of how accurately the black hole spin J can be measured, assuming the only unknown parameter is the black hole spin magnitude $\chi = J/M^2$ and assuming both the orbit and black hole spin vector are unknown (blue). Evaluated using the same initial parameters as above, except $\sigma_r = 0.1M$ and evolved according to Eq. (2.2.1). 39
- 8 The profiles of effective gravitational constant $G(r)$ for stars of $6M_\odot$ at $T_{\text{eff}} \approx 6000K$. The solid lines have metallicity $Z = 0.002$ and the dashed line has $Z = 0.02$. They are a third crossing Cepheids for $Z = 0.002$ and $\phi_* = 10^{-6}$ and a first crossing Cepheid for $Z = 0.02$ because they do not have the second crossings. The rest are second crossing Cepheids with $Z = 0.002$ 46

- 9 The post-main sequence HR diagram (L - T_{eff}) for stars of masses $5M_{\odot}$ (green), $6M_{\odot}$ (blue), $8M_{\odot}$ (purple), and $10M_{\odot}$ (red) in both GR (dashed lines) and MG (solid lines) regimes. The chameleon field is $\alpha_c = \frac{1}{3}$ and $\phi_* = 10^{-7}$ 47
- 10 The change in unperturbed radius, $\xi = dr/r_0$, of a $6M_{\odot}$ Cepheid as a function of radius and eigenmodes of Cepheids with metallicity $Z = 0.002$ in different chameleon fields, where $\alpha_c = \frac{1}{3}$ and ϕ_* varies. The stars on the top panel are at $T_{\text{eff}} \approx 5900K$ and the ones on the bottom panel (commented out in the draft) are at $T_{\text{eff}} \approx 6200K$. The dotted, dashed, and solid lines correspond to $\phi_* = 10^{-8}$, $\phi_* = 10^{-7}$, and $\phi_* = 10^{-6}$, respectively. The blue, purple, and green lines are fundamental modes, first overtones, and second overtones, respectively. The second and third crossings of instability strips are within the range of $3.73 < \log T_{\text{eff}} < 3.83$ or $5370K < T_{\text{eff}} < 6760K$ 48
- 11 The change in fundamental period $\Delta\Pi/\Pi_{\text{GR}}$ versus T_{eff} relations for stars of $5M_{\odot}$, $6M_{\odot}$, $8M_{\odot}$, and $10M_{\odot}$ with $\alpha_c = \frac{1}{3}$. Metallicity $Z = 0.002$ unless specified. The top figure has $\phi_* = 10^{-8}$, the middle figure has $\phi_* = 10^{-7}$, and the bottom figure has $\phi_* = 10^{-6}$. Solid lines are our MG results and dashed lines are plotted from JVS ansatz. The Cepheids in the first two subfigures are all at second crossings and in the third one are at the third crossings. In the second subfigure, the difference $\Delta\Pi$ are between $Z = 0.004$ and $z = 0.002$ in GR for the two dotted lines. 49
- 12 The dependence of $\Delta\frac{\Pi_1}{\Pi_0}/(\frac{\Pi_1}{\Pi_0})_{\text{GR}}$ vs T_{eff} relation on metallicity in GR regime, and on with and without a chameleon field of $\alpha_c = \frac{1}{3}$, $\phi_* = 10^{-7}$ for stars of $6M_{\odot}$ 50
- 13 The dependence of $\Delta\frac{\Pi_1}{\Pi_0}/(\frac{\Pi_1}{\Pi_0})_{\text{GR}}$ vs T_{eff} relation on metallicity in GR regime, and on with and without a chameleon field of $\alpha_c = \frac{1}{3}$, $\phi_* = 10^{-7}$ for stars of $10M_{\odot}$ 51

14	The eigenmodes of Polytrope $n = 3.0$ with Hong's code. ($n = 3.5$, and $n = 4.0$ are commented out.)	56
15	The normalized histogram of the distances of the found injections (blue) and test galaxy catalog (orange) from the 2016 MDC simulation set. The blue line is uses the gravitational-wave detection efficiency $\epsilon(r)$ while the red line is just a simple r^2 curve.	65
16	For the galaxy catalog in the MDC v1, the function $f(H_0)$ determined to produce a uniform prior $p_H(H_0)$ compared with a power-law in H_0 . The cubic scaling is expected for a smooth, uniform in volume distribution at large luminosity distance.	66
17	The posterior distribution of H_0 using the KDE method for the 250 coming from the MDC simulation with an empty galaxy catalog.	68
18	The posterior distribution of H_0 using the KDE method for the 250 coming from the MDC simulation. The angular selection uses all galaxies having a posterior sample within 80 kpc/ r of the galaxy center. The catalog used to determine the spatial distribution of signals is also used in the recovery step. The red vertical line corresponds to the peak value. The light lines are the posteriors as each event is added.	69
19	The peak values and one-sigma errors of Hubble constant as a function of the number of GW events in MDC simulations starting from MDC 1 and moving up in number to MDC 250 using the KDE method. The "real value" or the injected value for the simulations is 70km/s/Mpc . The colored bars show the one-sigma errors of H_0 measured by other teams, where the blue and the cyan colors correspond to results in Riess et al. (2016), and Planck Collaboration (2016), respectively.	70
20	The log-log plot of the one-sigma error of Hubble constant and its standard deviation (error bars) as a function of the number of GW events in MDC simulations using the KDE method.	71

21	The posterior distributions of H_0 using the KDE method for the 250 coming from the F2Y's MDC simulation with the 75%, 50%, 25% complete galaxy catalogs.	72
22	The posterior over H_0 using the information from the identification of the electromagnetic counterpart. The gravitational-wave samples were generated using the fixed position of the counterpart in NGC4993.	73
23	Cumulative blue luminosity as a function of redshift.	73
24	The posterior over H_0 using Glade v2.2. The gravitational-wave samples, generated using standard uniform in volume priors, were used to build a KDE of the posterior distribution from the gravitational-wave data and the galaxies were approximated as delta functions.	74

LIST OF TABLES

1	Orbital parameters for S2 and the black hole properties with Keck data and VLT data	22
2	The changes in effective G for different values of parameters α_c and ϕ_* for a $6M_\odot$ Cepheid at $T_{\text{eff}} \approx 6000K$ on the third crossing.	46
3	Comparison of Analytic and Numerical Solutions to Fundamental Periods of Selected Stellar Models in GR.	56

CONVENTIONS

- Greek letters (α, β, γ , etc) are used to indicate spacetime indices, which are summed over 0, 1, 2, 3, and Latin letters (a, b, c , etc) are used to indicate spatial indices, which are summed over 1, 2, 3.
- The Einstein summation convention is used where there is an implied sum over indices. For instance, $\eta_{\alpha\beta}T^\beta = \sum_{\beta=0}^3 \eta_{\alpha\beta}T^\beta$.
- Bold font is used to indicate a vector, such as spin vector **J** and position vector **x**.

ACKNOWLEDGMENTS

First and foremost I would like to thank Dr. Canbin Liang who taught me general relativity (GR) and Dr. Bernard Schutz who gave lectures on gravitational waves when I was enrolled in a PhD program in Astrophysics in National Astronomical Observatories of China in Beijing. After auditing GR course for a year and going to lectures on detecting gravitational waves with space detectors, I was captured by gravitational waves and decided to graduate with a Master's and do my PhD in the United States to study gravitational waves. Without them, I would never have known that my life in 5 years could have been learning in a pioneering team that opened a new era of astronomy.

Next I would like to thank Dr. Richard O'Shaughnessy, who has been like my second advisor and trained me on programming, applications of statistics to astrophysics, and has kept me more interested in General Relativity and physics since I started my research at UWM. He is a go-to person whenever I have a question related to gravitational wave physics or my academic career. Next I would like to thank my Graduate Advisor Dr. Patrick Brady for his insights in astrophysics topics and directions, and his charisma in leading, co-leading, and coordinating several teams in our CGCA and in the LSC - it is always good to have an example to learn from. He did a lot to help me with my academic career by including me into several research projects, guiding me to learn to collaborate within the LIGO team, as well as supporting my conference travels.

I would like to thank Dr. Jolien Creighton for answering the questions I had with LIGO data analysis softwares and making physics easier to understand. I would like to thank Dr. David Kaplan for supporting my research financially and always maintaining an encouraging research environment. I would like to thank Dr. Phil Chang for hands-on trainings on astrophysics and programming, and a lot of help with my academic career. I would like to thank Dr. John Friedman for his expertise in neutron stars. He could point out correctly where to examine within a few minutes after I stated a project problem that puzzled me and my collaborator for a week. I would also like to thank Dr. Paul Lyman for being my PhD committee member and Dr. Xavier Siemens for his advice in my development.

I would like to thank postdocs Dr. Chris Pankow and Dr. Sarah Caudill for their help with data analysis techniques. Chris was a go-to person whenever I had questions with data analysis pipelines and coding.

I would like to thank my fellow graduate students and friends Dr. Xiaoying Lin, Matt Brinson, Alex Urban, and Kristina Islo. Xiaoying has been a best friend since I came to US, always there to listen and help when I had ups and downs. Matt and Alex were good friends to hang out with and listen to music together with. Kristina was a good study buddy and friend.

I would also like to thank all the people in the CGCA and the Physics Department. I'd also like to thank the administration staff at the Physics Department. Thank you all.

I would also like to thank all my collaborators in the LIGO-Virgo Collaboration, especially the GstLAL team, rapidPE team, and Cosmology team.

Last but most importantly I would like to thank my family. I thank my parents for raising me up. I especially thank my mom for all the efforts she made to ensure me a place to live and to get educated, and for her enormous help of taking care of my son Maverick who is 17 month old now since even before he was born. I thank my son Maverick for being the perfect one. He has made me think a lot of meaningful things that the younger me had not. I thank my husband Ren for all the supports he has given throughout undergrad and grad schools and for his accompany of growing up together since we were undergrads. I would like to thank all the supportive family members we have. Special thanks to my elementary school math teacher Daofen who patiently taught me middle school math outside of class because I was interested. Special thanks to the kind-hearted Ke-E, who generously provided me financial supports in the first couple of years of my undergrad studying.

Chapter 1

Introduction

Newton's law of universal gravitation states that a mass attracts any other masses in the Universe. The attractive force between two masses is proportional to the product of the masses and inversely proportional to the square of the distance between the masses. The space and time are declared to be absolute and independent of the masses. This theory requires that the information about one mass be instantaneously conveyed to the other mass, and thus violates causality. Einstein's gravitation is described as a geometric property of spacetime. Einstein's theory of general relativity states that masses tell spacetime how to curve and in return spacetime tells masses how to move. Everything that moves freely throughout spacetime follows geodesics. More massive objects can change spacetime metric more extensively.

When massive objects accelerate, they perturb spacetime and change its metric, radiating energy to other regions of spacetime. The energy propagates in the form of gravitational radiation, known as gravitational waves, at the speed of light. Gravitational waves can be produced by any accelerating masses, but the more violent the motions, such as the inspiral of two black holes, the stronger the gravitational waves are produced. Daily activities such as a person writing her dissertation can also produce gravitational waves and leave some marks in spacetime even though these waves are too tiny to be detected.

1.1 General Relativity and Gravitational Waves

In this section, we will briefly review general relativity that is necessary for the derivation of GWs. We assume a basic knowledge of general relativity, for more detailed description one can refer to textbooks (Hartle 2003; Wald 1984). For gravitational-wave physics, I will summarize the necessary concepts for basic understanding of GWs and the research work stated in the dissertation. For a more detailed introduction, see a standard textbook (Creighton & Anderson 2011).

General relativity describes spacetime with the geometry of a four-dimensional manifold. The fundamental concept is the distance or spacetime interval between two points in spacetime. The spacetime interval is defined through the spacetime metric

$$ds^2 = g_{\mu\nu} dx^\mu dx^\nu \quad (1.1.1)$$

where $g_{\mu\nu}$ is known as the spacetime metric and dx^μ is the infinitesimal coordinate interval between two points. Repeated indices are summed from 0 to 3. An example is flat spacetime with no curvature present, where the space interval is given by

$$ds^2 = \eta_{\alpha\beta} dx^\alpha dx^\beta = -c^2(dt)^2 + (dx)^2 + (dy)^2 + (dz)^2 \quad (1.1.2)$$

where the symbol $\eta_{\alpha\beta}$ is the flat spacetime metric and it is defined as

$$\eta_{\alpha\beta} = \begin{bmatrix} -c^2 & 0 & 0 & 0 \\ 0 & 1 & 0 & 0 \\ 0 & 0 & 1 & 0 \\ 0 & 0 & 0 & 1 \end{bmatrix} \quad (1.1.3)$$

in Cartesian coordinates. The $t, x, y,$ and z are the time coordinate plus the three-dimensional space coordinates. The spacetime metric is usually a 4×4 matrix and not necessarily diagonal in general. The metric describes the curvature of spacetime that will tell matter how to move. In response, the matter will tell spacetime how to curve through stress-energy tensor $T_{\alpha\beta}$ that satisfies the continuity equation $\nabla^a T_{\alpha\beta} = 0$ for continuous matter and fields distributions.

The Einstein field equations that connect spacetime and matter are

$$G_{\alpha\beta} = R_{\alpha\beta} - \frac{1}{2}g_{\alpha\beta}R = \frac{8\pi G}{c^4}T_{\alpha\beta} \quad (1.1.4)$$

where $G_{\alpha\beta}$ is the Einstein tensor, $R_{\alpha\beta}$ is the Ricci tensor and R is the Ricci scalar. The latter two are contractions of the Riemann curvature tensor $R_{\alpha\beta\gamma\delta}$,

$$R_{\alpha\beta} = g^{\mu\nu}R_{\alpha\mu\beta\nu} \quad (1.1.5)$$

$$R = g^{\mu\nu}R_{\mu\nu} \quad (1.1.6)$$

In general relativity, test masses that fall freely through spacetime will follow the geodesics of that spacetime. The equations of motion for a freely-falling particle in a metric $g_{\alpha\beta}$ are

$$\frac{d^2x^\alpha}{d\tau^2} = -\Gamma_{\mu\nu}^\alpha \frac{dx^\mu}{d\tau} \frac{dx^\nu}{d\tau} \quad (1.1.7)$$

where τ is the proper time or the time measured by the particle if it carries a clock and $\Gamma_{\alpha\beta}^\gamma$ are the Christoffel symbols

$$\Gamma_{\alpha\beta}^\gamma = \frac{1}{2}g^{\gamma\delta} \left(\frac{\partial}{\partial x^\alpha}g_{\beta\delta} + \frac{\partial}{\partial x^\beta}g_{\delta\alpha} - \frac{\partial}{\partial x^\delta}g_{\alpha\beta} \right) \quad (1.1.8)$$

1.1.1 Linearized gravity

Linearized gravity is the weak-field approximation where the metric is taken to be a small linear perturbation from the flat spacetime metric. This approximation is good enough to describe the detection process for all existing ground based GW detectors. We write it as

$$g_{\alpha\beta} = \eta_{\alpha\beta} + h_{\alpha\beta} \quad (1.1.9)$$

where $h_{\alpha\beta}$ is the small perturbation away from the flat metric. Substituting it into Einstein's field equations, keeping linear orders of h and ignoring all $\mathcal{O}(h^2)$ terms, Einstein's field equations become

$$-\eta^{\mu\nu} \frac{\partial^2 \bar{h}_{\alpha\beta}}{\partial x^\mu \partial x^\nu} - \eta_{\alpha\beta} \frac{\partial^2 \bar{h}^{\mu\nu}}{\partial x^\mu \partial x^\nu} + \frac{\partial^2 \bar{h}^\mu_\beta}{\partial x^\alpha \partial x^\mu} + \frac{\partial^2 \bar{h}^\mu_\alpha}{\partial x^\mu \partial x^\beta} = \frac{16\pi G}{c^4}T_{\alpha\beta} \quad (1.1.10)$$

where $\bar{h}_{\alpha\beta}$ is the trace reversed metric and is defined $\bar{h}_{\alpha\beta} \equiv h_{\alpha\beta} - \frac{1}{2}\eta_{\alpha\beta}h$. The Einstein field equations can be further simplified by applying a gauge transformation into the Lorenz

gauge. The Lorenz gauge condition is defined as $\partial_\alpha \bar{h}^{\alpha\beta} = 0$. The linearized Einstein field equations with the Lorenz gauge are

$$-\square \bar{h}_{\alpha\beta} = \frac{16\pi G}{c^4} T_{\alpha\beta} \quad (1.1.11)$$

where $\square = \eta^{\mu\nu} \partial_\mu \partial_\nu$ is the d'Alembertian operator in flat spacetime.

1.1.2 Gravitational waves: solution to linearized Einstein field equations

For linearized gravity, the vacuum Einstein field equations are

$$\square \bar{h}_{\alpha\beta} = 0 \quad (1.1.12)$$

in the Lorenz gauge. The scenario to apply this is when an observer is far away from the matter source that generates these gravitational waves. We can assume that the spacetime far away is vacuum. The solution is a plane wave traveling at the speed of light.

There is an extra gauge freedom in the Lorenz gauge that can simplify things further. To remove the freedom, we choose a gauge in which the metric perturbation is both traceless ($h = \bar{h} = 0$) and purely spatial ($h_{\alpha 0} = 0$); this is known as transverse-traceless (TT) gauge. The metric's t and z components are then all zero under this gauge and four components are non-zero: $h_{11}^{\text{TT}}, h_{22}^{\text{TT}}, h_{12}^{\text{TT}}, h_{21}^{\text{TT}}$.

Because the metric is traceless, we have

$$h_{11}^{\text{TT}} = -h_{22}^{\text{TT}} \equiv h_+ \quad (1.1.13)$$

and because the metric is symmetric,

$$h_{12}^{\text{TT}} = h_{21}^{\text{TT}} \equiv h_\times \quad (1.1.14)$$

The h_+ and h_\times are the two possible polarizations of a gravitational wave. The definitions of “+” and “ \times ” are derived from their effects on matter. If we move into the TT gauge, for a freely-falling particle we deduce its equations of motion Eq. (1.1.7)

$$\frac{d^2 x^\alpha}{dt^2} = 0 \quad (1.1.15)$$

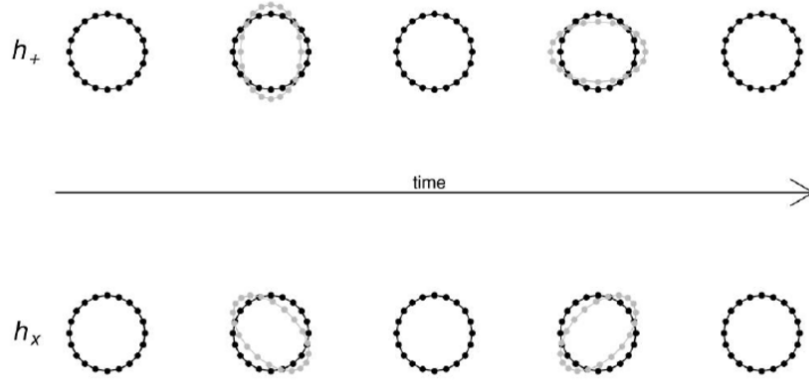


Figure 1 : A ring of freely-falling test particles is affected as shown for a purely plus and a purely cross polarized gravitational waves, traveling into the page. The diagram shows snapshot at a quarter of period intervals.

This means that in the TT gauge the test particles will not experience any coordinate acceleration due to gravitational waves. However, gravitational waves do have a physical effect on the motion of test particles by changing the *proper* distance between them. For a gravitational wave traveling along the z -axis, the proper distance along the x -axis between two freely-falling particles that has physical separation of L'_1 and located at x -axis is

$$L_1(t) \approx L'_1 \left[1 + \frac{1}{2} h_{11}^{\text{TT}}(t) \right] \quad (1.1.16)$$

For particles located on the y -axis and separated by L'_2 , the proper distance is

$$L_2(t) \approx L'_2 \left[1 + \frac{1}{2} h_{22}^{\text{TT}}(t) \right] \quad (1.1.17)$$

Fig.1 shows how a ring of test particles will be affected by a purely $+$ polarized gravitational wave and by a purely \times polarized one, respectively. You can see that the names $+$ and \times actually come from the physical effects.

We can use an interferometer to detect these changes in proper distances. In this case, the proper distance between an end mirror of the interferometer and the beam splitter will be perturbed by a gravitational wave that passes through. For a gravitational wave propagating along the z axis and perpendicular to the two arms of the interferometer, the difference between the length of each arm is known as gravitational-wave *strain*

$$\frac{\Delta L(t)}{L} \equiv \frac{L_1(t) - L_2(t)}{L} \approx h_+(t) \quad (1.1.18)$$

where L is the unperturbed arm length.

Generally a gravitational wave passing through an interferometer is a combination of the $+$ and \times polarizations. Using the antenna patterns (the mapping of polarizations onto strain), F_+ and F_\times , we can write the strain as

$$\frac{\Delta L(t)}{L} \approx h(t) = F_+(\theta, \phi, \psi)h_+(t) + F_\times(\theta, \phi, \psi)h_\times(t) \quad (1.1.19)$$

where (θ, ϕ) are the sky location of the GW source, and ψ is the polarization angle.

1.1.3 Sources of gravitational waves

Any binary system in which massive objects orbit each other generates gravitational waves. These systems are called compact binary systems. When stellar mass black holes and/or neutron stars orbit, they can get close enough together to generate waves in LIGO's band. Ground-based detectors such as advanced LIGO (The LIGO Scientific Collaboration 2015) are most sensitive to waves in $10 - 2000 \text{ Hz}$ range. On Sep 14, 2015 LIGO made the first detection of gravitational waves from a binary black hole (BBH) system (Abbott 2016a). Since then LIGO and Virgo have reported four more binary black hole mergers (Abbott 2016b, 2017a,b,c). On Aug 17, 2017 LIGO and Virgo detected the first binary neutron star (BNS) merger (Abbott 2017a).

A compact binary system is approximated by two point particles orbiting around each other, with masses m_1 and m_2 , orbital separation a , and orbital speed ω . The solution for the trace-reversed metric perturbation can be found using Green's functions

$$\bar{h}_{\alpha\beta}(t, \mathbf{x}) = \frac{4G}{c^4} \int \frac{\tau_{\alpha\beta}(t - \|\mathbf{x} - \mathbf{x}'\|/c, \mathbf{x}')}{\|\mathbf{x} - \mathbf{x}'\|} d^3x' \quad (1.1.20)$$

where $\tau_{\alpha\beta}$ is the effective stress-energy tensor. For the far-field regime, $\|\mathbf{x} - \mathbf{x}'\| \approx r$. The non-zero components of the quadrupole tensor are

$$I_{11} = \frac{1}{2}\mu a^2 \frac{(1 + \cos^2 \iota)}{2} (1 + \cos 2\phi) \quad (1.1.21)$$

$$I_{22} = \frac{1}{2}\mu a^2 \frac{(1 + \cos^2 \iota)}{2} (1 - \cos 2\phi) \quad (1.1.22)$$

$$I_{12} = I_{21} = \frac{1}{2}\mu a^2 \cos \iota \sin 2\phi \quad (1.1.23)$$

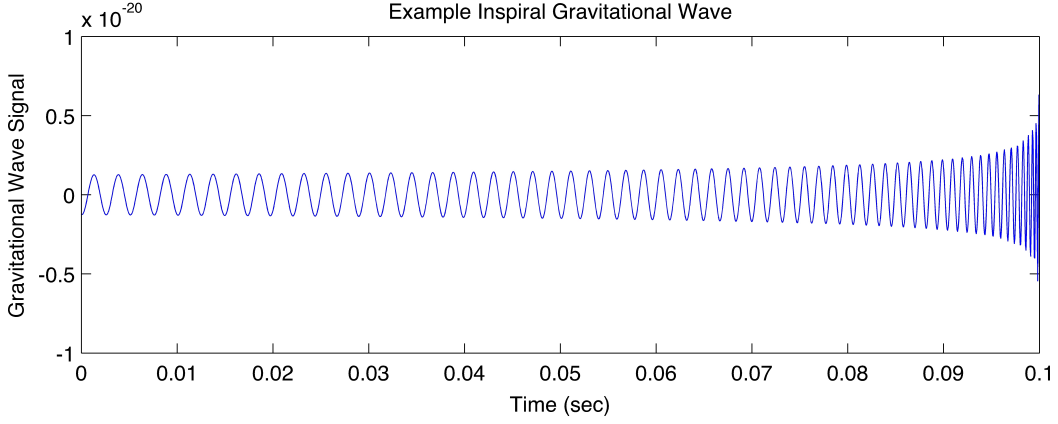


Figure 2 : A chirp waveform as a function of time is shown. Credit: <https://www.ligo.org/science/GW-Inspiral.php>

where $\mu = m_1 m_2 / (m_1 + m_2)$ is the reduced mass, ι is the inclination angle of the observer from the orbital axis, and phase $\phi = \int \omega dt$. The two polarizations are

$$h_+ = h_{11}^{\text{TT}} = -h_{22}^{\text{TT}} = -\frac{4G\mu a^2 \omega^2}{c^4 r} \frac{(1 + \cos^2 \iota)}{2} \cos 2\phi \quad (1.1.24)$$

$$h_\times = h_{12}^{\text{TT}} = h_{21}^{\text{TT}} = -\frac{4G\mu a^2 \omega^2}{c^4 r} \cos \iota \sin 2\phi . \quad (1.1.25)$$

and in terms of the orbital speed $v = a\omega$

$$h_+ = -\frac{2G\mu}{c^2 r} \left(\frac{v}{c}\right)^2 (1 + \cos^2 \iota) \cos 2\phi \quad (1.1.26)$$

$$h_\times = -\frac{4G\mu}{c^2 r} \left(\frac{v}{c}\right)^2 \cos \iota \sin 2\phi \quad (1.1.27)$$

The orbital separation of a compact binary system decays over time because the gravitational wave it radiates carries energy away. When the two objects of the system merge, it is called the coalescence. The time it takes the system to get to coalescence from some initial velocity v_0 is

$$t_c = \frac{5}{256\eta} \frac{GM}{c^3} \left(\frac{v_0}{c}\right)^{-8} \quad (1.1.28)$$

where $M = m_1 + m_2$ is the total mass.

The phase ϕ and speed v evolve over time as the orbit decays. For a binary system the two polarizations as a function of time to the leading order are (Creighton & Anderson

2011)

$$h_+(t) = -\frac{GM}{c^2 r} \frac{1 + \cos^2 \iota}{2} \left(\frac{c^3(t_c - t)}{5GM} \right)^{-1/4} \cos \left[2\phi_c - 2 \left(\frac{c^3(t_c - t)}{5GM} \right)^{5/8} \right] \quad (1.1.29)$$

$$h_\times(t) = -\frac{GM}{c^2 r} \cos \iota \left(\frac{c^3(t_c - t)}{5GM} \right)^{-1/4} \sin \left[2\phi_c - 2 \left(\frac{c^3(t_c - t)}{5GM} \right)^{5/8} \right] \quad (1.1.30)$$

where t_c and ϕ_c are the time and phase of coalescence, respectively, and \mathcal{M} is the chirp mass

$$\mathcal{M} = \frac{(m_1 m_2)^{3/5}}{M^{1/5}} \quad (1.1.31)$$

A generic gravitational wave produces on a detector a strain as a function of time, $h(t)$, which is called the gravitational waveform. For a CBC system,

$$h(t) = -\frac{GM}{c^2 D_{\text{eff}}} \left[\frac{c^3(t_0 - t)}{5GM} \right]^{-1/4} \cos \left(2\phi_0 - 2 \left[\frac{c^3(t_0 - t)}{5GM} \right]^{5/8} \right) \quad (1.1.32)$$

where t_0 is the termination time, i.e., the time of coalescence as observed in the detector $t < t_0$ and

$$\phi_0 = \phi_c - \frac{1}{2} \tan^{-1} \left(\frac{F_\times 2 \cos \iota}{F_+(1 + \cos^2 \iota)} \right) \quad (1.1.33)$$

$$D_{\text{eff}} = r \left[F_+^2 \left(\frac{1 + \cos^2 \iota}{2} \right)^2 + F_\times^2 \cos^2 \iota \right]^{-1/2} \quad (1.1.34)$$

An example waveform is shown in Fig. 2. Note that the frequency is in the range of human hearing so we often make an audio for a CBC waveform and it sounds like a chirp.

1.2 Dissertation Outline

This dissertation describes my contributions to LIGO's gravitational-wave science as well as tests of general relativity and theories of modified gravity. Chapter 2 discusses the work of testing general relativity with Galactic Center stellar orbits. Recent investigations have provided proof-of-principle calculations suggesting measurements of stellar or pulsar orbits near the Galactic Center could strongly constrain the properties of the Galactic Center black hole, local matter, and even the theory of gravity itself. We use a Markov Chain Monte Carlo to quantify what properties of the Galactic Center environment that measurements can constrain. We also used the Fisher matrix to understand

what correlations are well-constrained and why. Using both tools, we conclude that existing astrometric measurements cannot constrain the spin of the Galactic Center black hole. Extrapolating to the precision and cadence of future experiments, we anticipate that the black hole spin can be measured, extending previously-observed stellar orbits. Our simulations also give strategies of testing the black hole No-hair theorem if we have a tighter orbit in the future. Chapter 3 discusses testing modified gravity called chameleon field theory using Cepheid variable stars in extragalactic dwarf galaxies. Chameleon field theory is one of the attempts to explain the observed acceleration of our universe. We demonstrate the testing of chameleon field theory on stellar structure scales with the distance indicator Cepheid variable stars. Using the numerical results obtained for the evolutions of stars from MESA, we calculate the pulsation rates of Cepheid variable stars with both the theory of GR and the chameleon field theory. We then studied how well we could constrain the parameters that describe the chameleon fields and several factors that could impact our conclusion. Chapter 4 demonstrates a statistical method of measuring the expansion of our Universe using both gravitational-wave and electromagnetic observations. This method is complementary to the method using a standard siren (gravitational wave and its EM counterpart) and can be applied to future gravitational waves as well as be extended to studies of other cosmological parameters. Much of this work was carried out in collaboration with the LIGO-Virgo Cosmology group and will be part of a paper which is in preparation. Finally, in Chapter , I summarize the results obtained in this dissertation.

Chapter 2

Constrain the Relativity and Astrophysics with Galactic Center Stellar Orbits: Calibrating A Fisher Matrix Method Against Markov Chain Monte Carlo

2.1 Introduction

The supermassive black hole at the center of our galaxy provides unique opportunities to unambiguously investigate dynamics near a strongly-gravitating source (Psaltis & Johannsen 2011). Eventually, radio telescopes (Falcke et al. 2000) will image the immediate vicinity of the black hole, allowing direct constraints on the strong field of the black hole (via imaging accretion flows; (Falcke et al. 2000)) and the local density of massive companions (via limiting recoil effects from neighboring bodies (Broderick et al. 2011)). At present, however, the best opportunities to constrain the galactic center come from long-term monitoring of known stars (Gillessen et al. 2009). These measurements can also identify effects from the strong gravitational field (Zucker et al. 2006; Zucker & Alexander

2007) and the properties of the supermassive black hole (Weinberg et al. 2005; Will 2008; Merritt et al. 2010; Will & Maitra 2017). Even stronger constraints would be possible with a well-timed pulsar orbiting the galactic center (Liu et al. 2012; Rea et al. 2013a; Wex et al. 2013; Wharton et al. 2012), at separations comparable to a recently-discovered object (Rea et al. 2013b). High precision inference from stellar orbits, however, must account for many nearby perturbers, including the local stellar density of visible stars and compact objects (Merritt et al. 2010). Unfortunately, existing observations do not adequately constrain the perturbing density. For example, dynamical processes have long been expected to produce a high density of nearby massive objects, as yet inaccessible to direct electromagnetic observation (Freitag et al. 2006; Preto & Amaro-Seoane 2010; Alexander & Hopman 2009; Merritt 2010; Merritt et al. 2010; Genzel et al. 2010; Alexander & Pfuhl 2014). This likely-anisotropic dark density is most likely to be constrained indirectly, via its gravitational effects (e.g., (Alexander & Pfuhl 2014), though cf (Bartos et al. 2013)). Anisotropies in the ambient density can partially mimic the effects of modified theories of gravity; for example, a quadrupolar gravitational perturbation could be sourced by the black hole or an external cluster density.

In this chapter we assess how well present and future measurements of stellar orbits can constrain the black hole properties: its mass and particularly its spin. Specifically, we use a Markov-Chain Monte Carlo code to compare real and synthetic astrometric and radial velocity data with models for the stellar orbits and black hole mass, accounting for differences in reference frame between different observational campaigns. Unlike previous investigations, our model includes leading order post Newtonian corrections to the orbit from the black hole’s mass, spin, and quadrupole moment, as well as the impact of unknown non-quadrupole internal and exterior potentials. Our goal is to determine whether, despite the extremely low orbital velocity $v/c \simeq 0.02$, future measurements can significantly constrain strong-field features of the galactic center black hole. We compare our MCMC results against a detailed Fisher matrix analysis, both to validate our results and allow the reader to easily extrapolate to future measurement scenarios.

This chapter is organized as follows. In Section 2.2 we review a simplified model

for stellar dynamics near supermassive black holes (justified at length in Appendix 2.A); introduce simplified and realistic models for the process of measuring stellar orbits, including error; and review observations and theory of stellar and compact-object populations near the galactic center. In Section 2.3 we describe two techniques to assess how well measurements can constrain properties of stellar orbits and the supermassive black hole. The first technique is a simplified, approximate Fisher matrix. The second method, which provides definitive conclusions, uses detailed Markov-Chain Monte Carlo simulations of synthetic data to determine how well different parameters can be measured and why. After validating our procedure using analytically tractable toy models with a handful of parameters, we perform full-scale simulations. Using plausible choices of parameters, we discuss how the black hole spin and quadrupole moment can be measured. At its fundament, our study relies on well-established foundations in the astronomical literature on how to reconstruct stellar and planetary orbits from position measurements (astrometry); from radial velocity measurements, most famously via the Hulse-Taylor binary pulsar (Hulse & Taylor 1975); and from pulsar timing, including relativistic propagation effects (Liu et al. 2012).

2.2 Statement of the problem

2.2.1 What do astronomers observe

There are observations of stellar orbits within 1 arc second of Galactic center in infrared (Ghez et al. 2008; Gillessen et al. 2009). In this chapter, we are analyzing two data references from Ghez's (Ghez et al. 2008) and Gillessen's (Gillessen et al. 2009) groups. The motions of stars in the immediate vicinity of Sgr A* have been observed in infrared bands by NTT/VLT since 1992 and by Keck telescope since 1995. The two data sets we use are the Keck data from 1995 to 2007 and the VLT data from 1992 to 2009. Massive young stars are found closely orbiting the black hole at the center of our Milky Way. The locations of the stars, i.e., the astrometric positions, right ascensions (RA) and declinations (DEC) are recorded at different epochs. Therefore, the two groups measured

the relative positions of stars to the radio source Sgr A*, i.e., the offsets of RA and DEC. They also did spectroscopy from the observations of the star's frequency spectra to determine the radial velocities, i.e., the line of sight components of the velocities relative to the observers, of a star at different epochs.

2.2.2 Simplified models of stellar orbits

The approximations involved in deriving and justifying our equations of motion are provided in Appendix 2.A. Neglecting the black hole's recoil or the effect of ambient material, each star's position \mathbf{x} evolves according to leading-order post-Newtonian equations of motion (Will 2008; Merritt 2013; Will 1985)

$$\begin{aligned} \mathbf{a} = & -\frac{M\mathbf{x}}{r^3} + \frac{M\mathbf{x}}{r^3} \left(4\frac{M}{r} - v^2\right) + 4\frac{M\dot{r}}{r^2}\mathbf{v} \\ & - \frac{2J}{r^3} [2\mathbf{v} \times \hat{\mathbf{J}} - 3\dot{r}\mathbf{n} \times \hat{\mathbf{J}} - 3\mathbf{n}(\mathbf{L} \cdot \hat{\mathbf{J}})/r] \\ & + \frac{3Q_2}{2r^4} [5\mathbf{n}(\mathbf{n} \cdot \hat{\mathbf{J}})^2 - 2(\mathbf{n} \cdot \hat{\mathbf{J}})\hat{\mathbf{J}} - \mathbf{n}] \end{aligned} \quad (2.2.1)$$

where $\mathbf{v} = \partial_t \mathbf{x}$, $\mathbf{a} = \partial_t^2 \mathbf{x}$ are the (harmonic) coordinate velocity and acceleration; where $r = |\mathbf{x}|$ is the coordinate distance from the black hole and $\mathbf{n} = \mathbf{x}/r$ is a unit vector pointing towards it; and where $M, \mathbf{J}, \mathbf{Q}$ are the mass, spin angular momentum, and quadrupole moment from the black hole. Equivalently, each particle evolves according to a post-Newtonian Hamiltonian in (Tichy & Flanagan 2011); higher-order hamiltonians that have been derived and exhaustively discussed in the post-Newtonian literature.

For the proof-of-concept analytic calculations described below, rather than work with the full hamiltonian, following standard practice in celestial mechanics we separate timescales by *orbit-averaging*. For analytic simplicity, we will furthermore treat all perturbations at leading order, therefore performing an orbit average using a Newtonian orbit; for example, at leading order an equatorial orbit has form $r(t) = p/(1 + e \cos \Phi(t))$ where p is a semilatus rectum. Using standard methods of celestial mechanics (Will 2008; Sadeghian & Will 2011), we find secular equations of motion for the orbit average ($\langle X \rangle$) of each star's Newtonian orbital angular momentum $L_N \equiv \mu \mathbf{x} \times \mathbf{v}$ and Newtonian

Runge-Lenz vector $\mathbf{A}_N \equiv \mu^2[\mathbf{v} \times (\mathbf{x} \times \mathbf{v}) - GM\hat{n}]$:

$$\partial_t \langle \mathbf{L}_N \rangle = \vec{\Omega} \times \langle \mathbf{L}_N \rangle \quad (2.2.2)$$

$$\partial_t \langle \mathbf{A}_N \rangle = \vec{\Omega} \times \langle \mathbf{A}_N \rangle \quad (2.2.3)$$

$$\vec{\Omega} = \vec{\Omega}_S + \vec{\Omega}_J + \vec{\Omega}_Q \quad (2.2.4)$$

$$\vec{\Omega}_S = \hat{L}_N \frac{A_S}{P} = \hat{L}_N \frac{3}{p(a/M)^{3/2}} \quad (2.2.5)$$

$$\vec{\Omega}_J = [\hat{J} - 3\hat{L}(\hat{L} \cdot \hat{J})] \frac{A_J}{P} = [\hat{J} - 3\hat{L}\hat{L} \cdot \hat{J}] \frac{2J/M}{(Mp^3)^{1/2}(a/M)^{3/2}} \quad (2.2.6)$$

$$\vec{\Omega}_Q = -(\hat{J}(\hat{J} \cdot \hat{L}) + \frac{1}{2}\hat{L}(1 - 3(\hat{L} \cdot \hat{J})^2)) \frac{A_Q}{P}$$

$$A_Q = \frac{3}{2} \frac{Q_2}{p^2(a/M)^{3/2}} \quad (2.2.7)$$

where the expressions A_S, A_J, A_Q are provided as in (Will 2008) and as implicitly defined above; see also (Iorio 2011) The factors A_S, A_J, A_Q are shown in Figure 3. These orbit-averaged precession equations imply a straightforward procedure for the (linear) perturbation due to Ω , starting from a Newtonian solution $\vec{r}_o(t)$:

$$\vec{r}(t) \simeq R(t)\vec{r}_o(t) \quad (2.2.8)$$

where $R(t)$ is the rotation generated by the (orbit-averaged) $\vec{\Omega}$. Specifically, again working to first order in the orbit-averaged perturbations, the secular rotation $R(t)$ on short timescales is determined by the generators \mathcal{L}_α of rotations:

$$R(t) \simeq \mathbf{1} - it\mathcal{L}_\alpha\Omega^\alpha \quad (2.2.9)$$

$$\vec{r}(t) \simeq r_o(t) - it\Omega^\alpha\mathcal{L}_\alpha r_o \quad (2.2.10)$$

2.2.3 Relationship between real observation and theoretical model

In order to use real data to measure the parameters of the whole system, we have to convert the measurements in the theoretical model in the Cartesian coordinates that originated at the black hole center to the real observed data form, RA and DEC offsets that are relative to Sgr A* in the Equatorial coordinate system which is centered at the Earth.

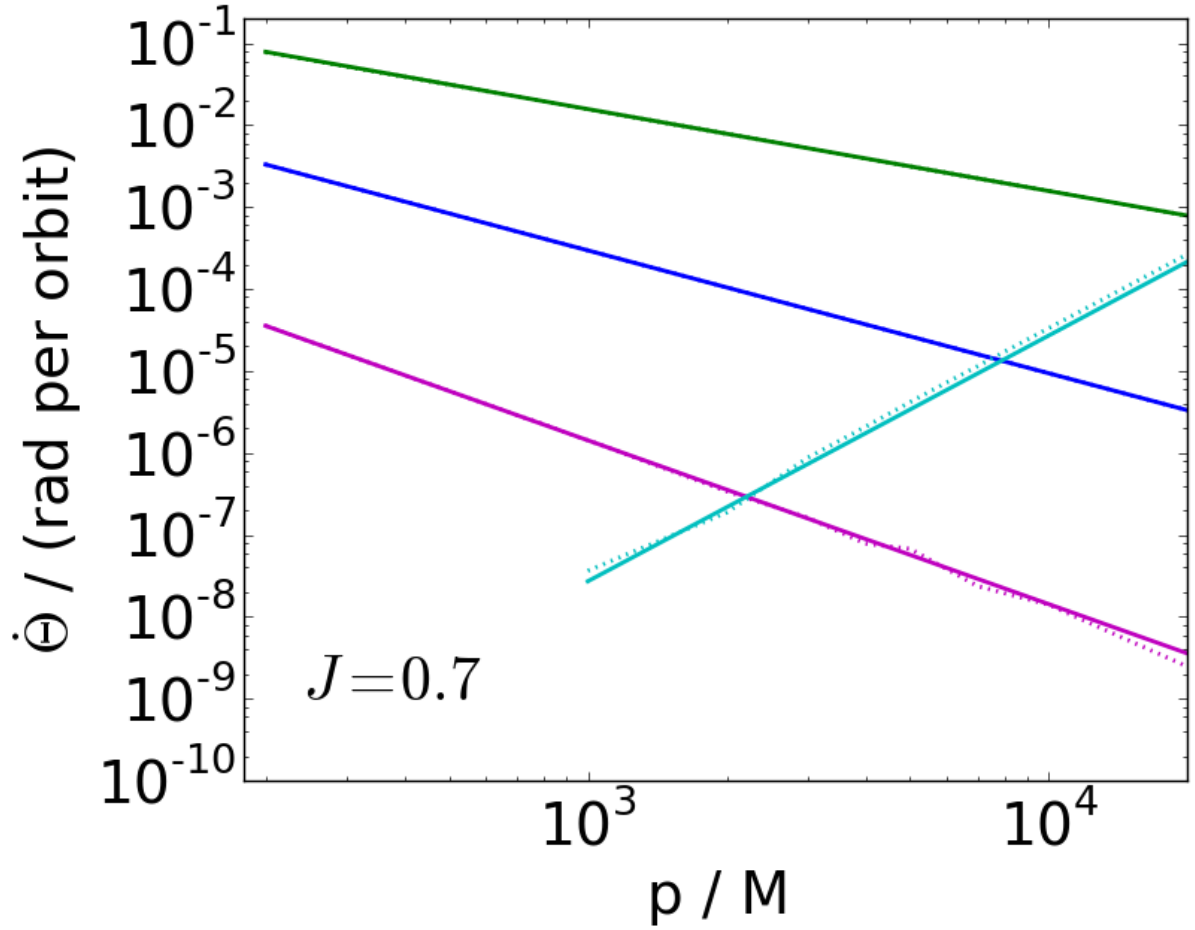


Figure 3 : Relative magnitude of different effects: A plot of different characteristic rates of change for stellar orbits around supermassive black holes, versus semilatus rectum. Solid curves show analytic results; dotted curves were derived from our time-domain evolution code, as validation. The solid green, blue, and purple curves show A_S, A_J, A_Q implicitly defined in Eq. (2.2.2). The cyan curves show the influence of an external quadrupolar potential from ambient stars at a distance of 30 kilo-masses of black hole.

We first generate the orbit of a star with our mixed Python/Fortran code, and get the star's orbital positions, $\vec{r}_i^{bh} = \{x_i^{bh}, y_i^{bh}, z_i^{bh}\}$, in the black hole frame. Then we transformed from a Cartesian coordinates that centered at Sgr A* to the Equatorial RA and Dec, or in terms of components

$$x_i = x_i^{bh} + d \cos \alpha_{bh} \sin \delta_{bh} \quad (2.2.11)$$

$$y_i = y_i^{bh} + d \sin \alpha_{bh} \sin \delta_{bh} \quad (2.2.12)$$

$$z_i = z_i^{bh} + d \cos \delta_{bh} \quad (2.2.13)$$

where d is the distance from the Earth to the center of black hole, α_{bh} and δ_{bh} are the RA and DEC of the black hole, x axis points to the First Point of Aries, and z axis points to the same direction as that in the black hole coordinates. The black hole Cartesian coordinates and the Earth Cartesian coordinates are only a translation of their origins described by \vec{d} . Then we convert the positions of the star from the Cartesian coordinate system that centers at the Earth to the Equatorial coordinate system,

$$\alpha_i = \tan^{-1} \frac{y_i}{x_i} \quad (2.2.14)$$

and

$$\delta_i = \sin^{-1} \frac{z_i}{\sqrt{x_i^2 + y_i^2 + z_i^2}} \quad (2.2.15)$$

where α_i is zero in the x-axis direction, and increases to 2π along the celestial equator counterclockwise as viewed from the North pole, and δ_i is zero in the celestial equator, positive to the north and negative to the south of the celestial equator. We subtract from $\{\alpha_i, \delta_i\}$ a reference position such as the astrometry position of Sgr A*, $\{\alpha_0, \delta_0\}$, and get the observed RA and DEC offsets relative to Sgr A*, $\{\Delta\alpha_i, \Delta\delta_i\}$, that are similar to those in the real data, where $\Delta\alpha_i = \alpha_i - \alpha_0$ and $\Delta\delta_i = \delta_i - \delta_0$. Notice the position of Sgr A* does not necessarily co-locate the center of the black hole. The difference between them can be modeled as five parameters, including the relative position of the black hole to the Sgr A*, $\Delta\alpha_{bh}$ and $\Delta\delta_{bh}$, and the uniform RA and DEC velocities and radial velocity, $\{v_{\alpha_{bh}}, v_{\delta_{bh}}, v_{r,bh}\}$, of the black hole relative to the Sgr A*. The radial velocities of the

stellar orbit are evaluated as $v_{r,i} = \vec{v}_i \cdot \hat{r}_i$, where $\hat{r}_i = \vec{r}_i/r_i$ are the unit vectors of line of sight.

Based on our model, the following parameters are measured from the data: the six orbital parameters of the star $\{a, e, \Phi_0, \alpha, \beta, \gamma\}$ (where a is semi-major axis, e is eccentricity, Φ_0 is the initial orbital phase at some moment, and the other three are Euler angles following a z-x-z definition), the three black hole spin components $\vec{J} = \{J_x, J_y, J_z\}$, the mass of the black hole M , the position of the black hole relative to the Sgr A* (or any reference for offsets measurements) $\{d, \Delta\alpha_{bh}, \Delta\delta_{bh}\}$ (where d is the distance from Sgr A* to us and the other two indicate the black hole's astronomical position), and the motion of the black hole relative to the Sgr A* $\{v_{\alpha_{bh}}, v_{\delta_{bh}}, v_{r,bh}\}$. To test the no hair theorem, we also use two more parameters, the quadrupole term, Q_2 , of black hole potential and the quadrupole term Q_X due to the external potential of star clusters that extend between $40,000M$ and $80,000M$ to Sgr A*. Throughout the chapter everything is in the units of $M_* = 4.00 \times 10^6 M_\odot$ when we perform calculations.

2.3 Measuring parameters

2.3.1 Bayesian formalism

According to the Bayesian paradigm, a prior distribution $p(\vec{\lambda})$ is used to quantify our knowledge about a set of unobservable parameters $\vec{\lambda}$ in a statistical model when no data are available. We can update our prior knowledge using the conditional distribution of parameters, given observed data, via the Bayes theorem. Suppose that the likelihood, or the distribution of the data from an assumed model that depends on the parameter $\vec{\lambda}$ is denoted by $p(D|\vec{\lambda})$, Bayes theorem updates the prior to the posterior by accounting for the data,

$$p(\vec{\lambda}|D) = \frac{p(D|\vec{\lambda})p(\vec{\lambda})}{p(D)} \quad (2.3.1)$$

where $p(D) = \int p(D|\vec{\lambda})p(\vec{\lambda})d\vec{\lambda}$ is the evidence of the data and also a normalizing constant.

To separate issues pertaining to measurements from physics from simplified models of stellar orbits, we describe results using the real measurement scenario, where only the angular offsets and radial velocity can be measured. [For comparison and to validate our MCMC method, we also employ idealized theoretical measurement scenarios in Appendix 2.C.] This realistic measurement model accounts for all of the parameters described in Section 2.2.3. The probability distribution of the data given parameters $\vec{\lambda}$ is

$$\begin{aligned}
p(\{D\}|\vec{\lambda}) &= \prod_k^{N_{\Delta\alpha}} (2\pi\sigma_{\Delta\alpha_k}^2)^{-1/2} \exp -\frac{[\Delta\alpha(t_k|\vec{\lambda}) - \Delta\alpha_k]^2}{2\sigma_{\Delta\alpha_k}^2} \\
&\times \prod_k^{N_{\Delta\delta}} (2\pi\sigma_{\Delta\delta_k}^2)^{-1/2} \exp -\frac{[\Delta\delta(t_k|\vec{\lambda}) - \Delta\delta_k]^2}{2\sigma_{\Delta\delta_k}^2} \\
&\times \prod_k^{N_{v_r}} (2\pi\sigma_{v_{r,k}}^2)^{-1/2} \exp -\frac{[v_r(t_k|\vec{\lambda}) - v_{r,k}]^2}{2\sigma_{v_{r,k}}^2}
\end{aligned} \tag{2.3.2}$$

where $\Delta\alpha(t_k|\vec{\lambda})$ and $\Delta\alpha_k$ are the theoretical prediction of the RA offset and the real observation, respectively, at epoch t_k ; the notations are similar for the other two observables, i.e., DEC offset and radial velocity; $\sigma_{\Delta\alpha_k}$, $\sigma_{\Delta\delta_k}$, and $\sigma_{v_{r,k}}$ are measurement uncertainties for the observation at t_k . The number of measurements for the three observables are denoted as $N_{\Delta\alpha}$, $N_{\Delta\delta}$, N_{v_r} , respectively. In the equation above, we have assumed that each measurement of each observable has a noise of Gaussian distribution.

In order to determine the best-fit parameters and their uncertainties we use a Markov chain Monte Carlo (MCMC) analysis to sample the posterior distribution function in Eq. (2.3.2). Specifically, we use an ensemble MCMC sampler named EMCEE (Goodman & Weare 2010; Foreman-Mackey et al., 2011).

2.3.2 Fisher matrix

To better understand and validate our MCMC results, and to make efficient projections about future hypothetical measurements, we perform a semi analytic calculation that approximates the likelihood in Eq. (14) by a locally quadratic approximation. The coefficient of the second-order term is known as the Fisher matrix.

The illustration of the mechanics of a Fisher matrix calculation is shown in Appendix 2.C by employing the idealized measurement model in Cartesian coordinates. For real

observations, we can do the same by exploiting in the special case that the observed data is exactly as predicted by some set of model parameters $\vec{\lambda}'$ [i.e., $\Delta\alpha_k = \Delta\alpha(t_k|\vec{\lambda}')$, $\Delta\delta_k = \Delta\delta(t_k|\vec{\lambda}')$, and $v_{r,k} = v_r(t_k|\vec{\lambda}')$]. Using a first-order Taylor series expansion $\Delta\alpha(t_k|\vec{\lambda}) - \Delta\alpha(t_k|\lambda') \simeq \delta\lambda^a \partial\Delta\alpha(t_k)/\partial\lambda_a$ for the RA offset $\Delta\alpha$ versus parameters $\vec{\lambda}$ (here λ^a are the elements of $\vec{\lambda}$ and same index a means contraction) and similar for the other two observables, we find that the conditional probability of the data given $\vec{\lambda}$ can be approximated by

$$\ln p(\{D\}|\vec{\lambda}) = \text{const} - \frac{1}{2}\Gamma_{ab}\delta\lambda_a\delta\lambda_b \quad (2.3.3)$$

$$\Gamma_{ab} = \sum_k \left[\frac{C_{\lambda_a, \Delta\alpha_k} C_{\lambda_b, \Delta\alpha_k}}{\sigma_{\Delta\alpha_k}^2} + \frac{C_{\lambda_a, \Delta\delta_k} C_{\lambda_b, \Delta\delta_k}}{\sigma_{\Delta\delta_k}^2} + \frac{C_{\lambda_a, v_{r,k}} C_{\lambda_b, v_{r,k}}}{\sigma_{v_{r,k}}^2} \right] \quad (2.3.4)$$

where Γ_{ab} is the Fisher matrix. For a parameter of two values λ_a and λ'_a of $\delta\lambda_a$ difference that results in two orbits, the components in Eq.(2.3.4) for this parameter are

$$C_{\lambda_a, \Delta\alpha_k} \equiv \frac{\partial\Delta\alpha(t_k)}{\partial\lambda_a} = \frac{\Delta\alpha(t_k|\lambda_a) - \Delta\alpha(t_k|\lambda'_a)}{\delta\lambda_a} \quad (2.3.5)$$

$$C_{\lambda_a, \Delta\delta_k} \equiv \frac{\partial\Delta\delta(t_k)}{\partial\lambda_a} = \frac{\Delta\delta(t_k|\lambda_a) - \Delta\delta(t_k|\lambda'_a)}{\delta\lambda_a} \quad (2.3.6)$$

$$C_{\lambda_a, v_{r,k}} \equiv \frac{\partial v_r(t_k)}{\partial\lambda_a} = \frac{v_r(t_k|\lambda_a) - v_r(t_k|\lambda'_a)}{\delta\lambda_a} \quad (2.3.7)$$

Having estimated the Fisher matrix and hence approximated $p(\{D\}|\vec{\lambda})$ by a Gaussian, we can further construct marginalized distributions for subset variables λ_A in $\vec{\lambda} = (\lambda_A, \lambda_a)$ by integrating out the variables λ_a . In the gaussian limit, this integration implies the marginalized distribution has a covariance matrix $\bar{\Gamma}_{AB}$ given by

$$\bar{\Gamma}_{AB} = \Gamma_{AB} - \Gamma_{Aa}[\Gamma^{-1}]_{ab}\Gamma_{bB} \quad (2.3.8)$$

Because the second term is negative, the marginalized distribution is always wider: adding additional uncertain degrees of freedom leads to less accurate measurements.

The Fisher matrix is a cross check for the parameter estimations obtained from MCMC. Drawing in the best-fit parameters estimation, the Fisher matrix can give the estimates of the uncertainties of parameters in a few seconds, whereas it takes MCMC a couple of days in our problem. A Fisher matrix can also let us test how sensitively the measurement accuracy and hypothesis tests depend on stellar parameters.

To illustrate the utility of the Fisher matrix in a concrete scenario, we consider a synthetic stellar orbit similar to S2, which is a star that is located close to the radio source Sagittarius A*, orbiting it with an orbital period of about 16 years. As described in the Appendix using an analytic measurement model and as we verify numerically, we can show that highly eccentric orbits with smaller pericenter distance provide the best constraints on BH spin J , because with the same semi-major axis a more highly eccentric orbit is closer to the BH and thus more impacted by the BH spin. This is why S2 can provide more information (as is the case in our simulations) about the black spin than what S102 can do for the same total observation time interval and the same arrangement of measurements during that time interval even though S102 has a shorter period and thus a smaller semi-major axis. We also point it out that if we have another orbit similar to S2 and we observe both of them equally frequently and for the same amount of time duration, we are expected to see an improvement of a factor of $\sqrt{2}$ in the measurement uncertainty of black hole spin from Fisher matrix studies. We can make the same conclusion if we observe S2 alone twice as often. The simulations in 2.4.2 utilized this property. However, if we can not observe as often as needed to measure the black hole spin, the solution would be either we improve the telescope performance or find a closer star to the Galactic center.

2.3.3 Results on the real data

After testing the validity of our mixed Python/Fortran program using a highly idealized measurement scenario (see Appendix 2.C.3), we use real observed data to measure the

parameters of Galactic center orbit of S2 and the properties of the black hole as reported elsewhere (Ghez et al. 2008; Gillessen et al. 2009). Our results agree with their work within systematic and statistical errors. This shows that our program works well with real observations and therefore the validity of using it is assured to calculate several hypotheses in Section 2.4 with real data.

Keck S2 data (Ghez et al. 2008) are used to estimate the parameters assuming the black hole is not free to move relative to us. The best-fit parameters and their uncertainties are shown in Table 1. The black hole is assumed to be Schwarzschild.

VLT S2 data in (Gillessen et al. 2009) are also used to estimate the parameters, see Table 1. The χ^2 are about 200 and the reduced χ^2 is about 1 for the number of degree of freedom being 143, the degree of freedom of the data subtracted by the number of parameters. Notice that for two measurements that were taken at the same time, the mean of the two measurements of $\{\Delta\alpha_i, \Delta\delta_i\}$ is used as the measurement that happened at that time and the larger error bars are used as the error bars of the observables.

Table 1 : Orbital parameters for S2 and the black hole properties with Keck data and VLT data

Parameter (Symbol) [Unit]	Keck best-fit	VLT best-fit	VLT best-fit w/o 2002
Semi major axis (a) [M_*]	$2.45 \times 10^4 \pm 440$	$2.636 \times 10^4 \pm 446$	$2.452 \times 10^4 \pm 594$
Eccentricity (e)	0.9048 ± 0.0038	0.8953 ± 0.0040	0.9038 ± 0.0060
Initial phase (Φ_0) [radians]	3.178 ± 0.0029	3.031 ± 0.0032	3.038 ± 0.0040
Euler angle 1 (α) [radians]	0.268 ± 0.008	0.186 ± 0.0076	0.227 ± 0.0136
Euler angle 2 (β) [radians]	1.464 ± 0.013	1.490 ± 0.016	1.444 ± 0.0252
Euler angle 3 (γ) [radians]	3.936 ± 0.013	4.047 ± 0.012	4.030 ± 0.0120
Distance (d) [kpc]	7.328 ± 0.017	8.422 ± 0.288	7.571 ± 0.382
RA of BH (α_0) [radians]	$1.4166 \times 10^{-8} \pm 4.42 \times 10^{-9}$	$4.99 \times 10^{-9} \pm 3.15 \times 10^{-9}$	$9.86 \times 10^{-9} \pm 3.34 \times 10^{-9}$
DEC of BH (δ_0) [radians]	$-4.2962 \times 10^{-8} \pm 6.543 \times 10^{-9}$	$-1.84 \times 10^{-8} \pm 7.41 \times 10^{-9}$	$-1.575 \times 10^{-8} \pm 1.026 \times 10^{-8}$
Mass (M) [$10^6 M_\odot$]	4.468 ± 0.236	4.492 ± 0.244	3.624 ± 0.272
Spin (J)	not sure	not sure	not sure
Reduced χ^2 [1]	1.4	1.0	1.0

The table shows the estimation of the six parameters of S2 orbits and four parameters of the Galactic center black hole from Keck data using our MCMC program. The best-fit parameters are consistent with Ghez's and Gillessen's analyses within 2σ and the uncertainties are consistent. The second, third, and fourth rows are the best-fits of the parameters and their uncertainties with Keck data, VLT data, and VLT data subtracted by its data in 2002 to compare with Keck data as Keck does not contain observations in 2002, respectively.

We point out the fact that the spin of the black hole is not testable with the two data sets. Here $M_* = 4 \times 10^6 M_\odot$ is used as a scale of black hole mass.

2.4 Testing various Hypotheses

2.4.1 Bayesian hypothesis selection

We assume that the observed orbital data D to have arisen under one of the two hypotheses H_1 and H_2 according to probability density $P(D|H_1)$ or $P(D|H_2)$ and for given prior probabilities $P(H_1)$ and $P(H_2) = 1 - P(H_1)$, we obtain from Bayes's theorem

$$P(H_i|D) = \frac{P(D|H_i)P(H_i)}{P(D|H_1)P(H_1) + P(D|H_2)P(H_2)} \quad (2.4.1)$$

$(i = 1, 2)$

and

$$\frac{P(H_1|D)}{P(H_2|D)} = \frac{P(D|H_1) P(H_1)}{P(D|H_2) P(H_2)} \quad (2.4.2)$$

where we define the Bayes factor as

$$B_{12} = \frac{P(D|H_1)}{P(D|H_2)} \quad (2.4.3)$$

When the two hypotheses are equally probable, the Bayes factor B_{12} is equal to the posterior odds in favor of H_1 .

If for H_1 and H_2 we choose models M_1 and M_2 parametrised by model parameter vectors θ_1 and θ_2 , we then have to select between the two models using the Bayes factor,

$$B_{12} = \frac{P(D|M_1)}{P(D|M_2)} = \frac{\int P(\theta_1|M_1)P(D|\theta_1, M_1)d\theta_1}{\int P(\theta_2|M_2)P(D|\theta_2, M_2)d\theta_2} \quad (2.4.4)$$

where $P(\theta_1|M_1)$ is the prior probability distribution function of parameter vector θ_1 in M_1 .

2.4.2 Does the Galactic center BH have spin

An intriguing question that has aroused perpetual interest is whether the Galactic center black hole has spin. Working in the framework of GR, we choose the same parameter vector for both non-spin (model M_1) and spin (M_2) models that address the S2 orbit around the Galactic center black hole, i.e., $\theta_1 = \theta_2 = \{a, e, \Phi_0, \alpha, \beta, \gamma, d, \alpha_0, \delta_0, M, \mathbf{J}, Q\}$, and apply Bayesian statistics to answer the question.

Our models M_1 and M_2 are nested, i.e., M_2 reduces to M_1 when the spin J or dimensionless spin $\chi = J/M^2$ acquires 0. For a smooth, marginalized posterior probability distribution $P(J, M_2|D)$ that has a maximum and is obtained from an MCMC sampling, we

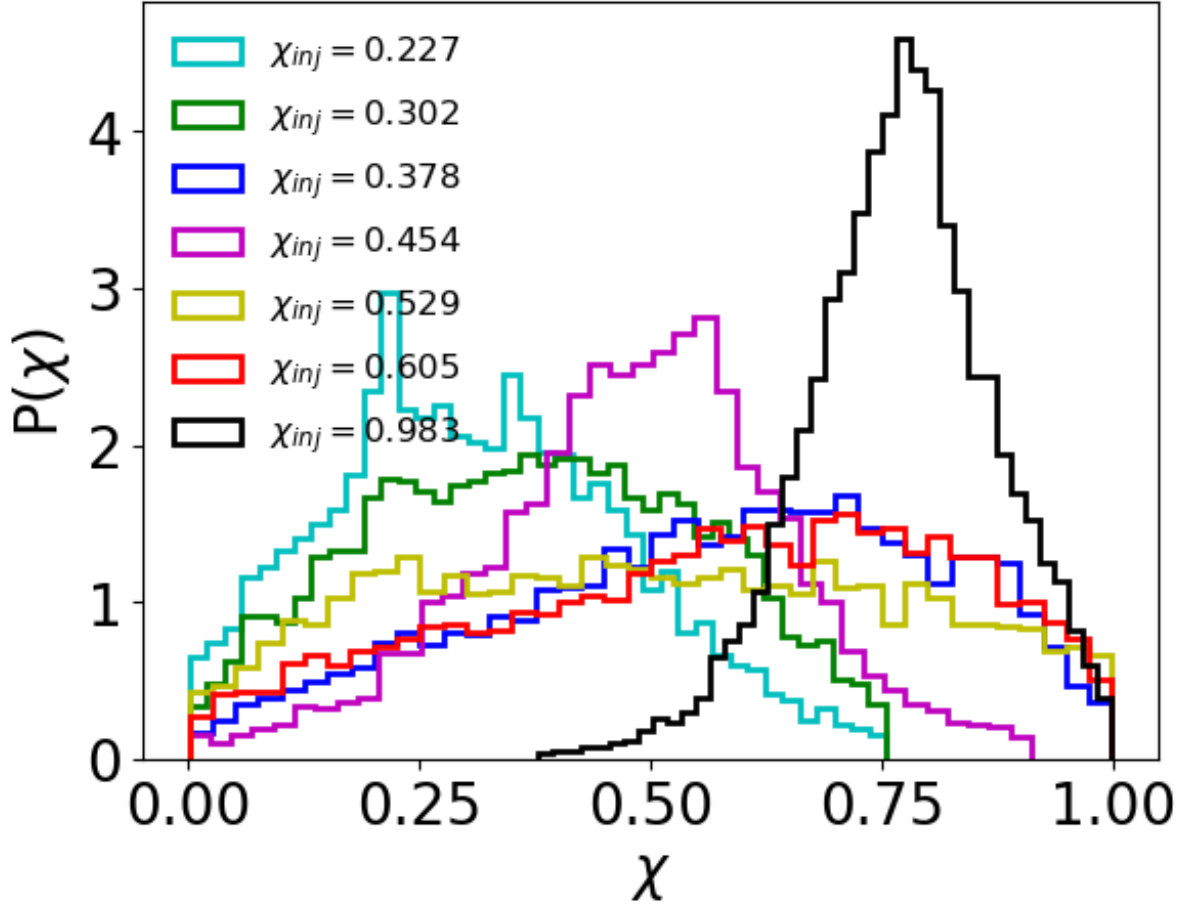


Figure 4 : The figure shows the marginalized posteriors of dimensionless spin $\chi = J/M^2$ with different injected values χ_{inj} and their corresponding quadrupole variables $Q_2 = -J_{inj}^2/M$. The range of spin J is $[0, M^2]$, where $M = 1.15M_*$ and $M_* = 4.0 \times 10^6 M_\odot$. The measurement uncertainties $\{\sigma_{\Delta\alpha} = \sigma_{\Delta\delta} = 10 \mu\text{as}, \sigma_{v_r} = 500 \text{ m/s}\}$ are the limit of GRAVITY at the distance of 8 kpc. The star has an S2-ish orbit and is observed once per day for an entire orbit of 16 years.

define the 90% credible interval to be $\chi \in [\chi_L, \chi_H]$ such that $\int_{\chi_L}^{\chi_H} P(\chi, M_2|D)d\chi = 0.90$ with $P(\chi_L, M_2|D) = P(\chi_H, M_2|D)$. Because a symmetric 90% CI will always exclude $\chi = 0$, we also evaluate the Savage-Dickey ratio (the ratio of the posterior to the prior of χ), which provides an estimate for the Bayes factor in favor of nonzero versus zero spin. For Keck data of S2 up to 2008 in Table 3 in (Ghez et al. 2008) and VLT data up to 2009 in (Gillessen et al. 2009), respectively, we use our MCMC code to obtain their posteriors for dimensionless spin χ and quadrupole term Q , and both of the posteriors are uniform distributions. Notice that Q is treated as a variable, see more details in Section 2.4.3. Therefore, we cannot say with any confidence that the Galactic center black hole has spin with either data set.

What measurements of star S2 can allow us to constrain black hole spin? We assume

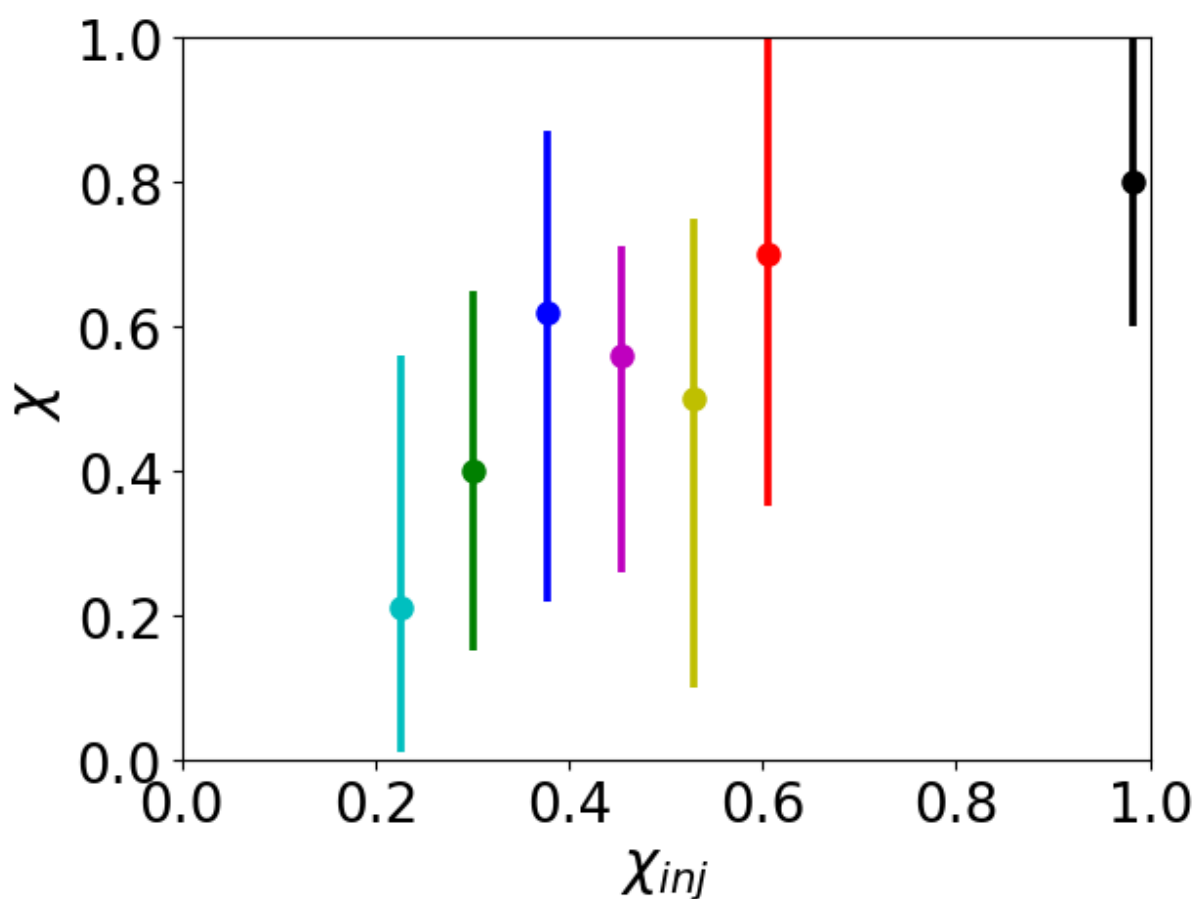


Figure 5 : Peak value and 90% credible interval as a function of injected dimensionless spin χ_{inj} for the best achievable measurement accuracies of GRAVITY using Galactic center orbits in the near future with $\{\sigma_{\Delta\alpha} = \sigma_{\Delta\delta} = 10 \mu as, \sigma_{v_r} = 500 m/s\}$. Dots show the maxima of posterior estimates of χ ; bars indicate the 90% confidence interval.

some future achievable observation accuracy and use our code to conduct fake/virtual observations of a star similar to S2 around a black hole similar to the Galactic Center one with an injected spin value J_{inj} . We also assume that each measurement of the star orbit, i.e., the three observables including two angular offsets and radial velocity, is a Gaussian distribution in each observable. Then we use MCMC code to find the best fit values and marginalized posterior distributions of the parameters, especially the black hole spin, given the fake observed data, D_f . The parameters we use for the black hole are $M = 4.6 \times 10^6 M_\odot = 1.15M_*$ and $d = 8.0 kpc$ which are determined by the observed S2 orbit, the injected χ values are from 0.3 to 0.98. The orbit has $a = 2.65 M_*$, $e = 0.8847$, $\Phi_0 = -0.1$ (which corresponds to Aug, 2017 for S2, and assume that is when we start the virtual observations) and three Euler angles that have the values of an S2 orbit. The measurement accuracies are $\sigma_{\Delta\alpha_i} = \sigma_{\Delta\delta_i} = 10 \mu as$ and $\sigma_{v_{r,i}} = 500 m/s$, which are the limits of GRAVITY instrument (GRAVITY Collaboration 2017). We get from MCMC the marginalized posterior $P(\chi, M_2|D_f)$ for the fake observed data with that injected spin value χ_{inj} . We then do the same for different injected values of black hole spin. Fig 4 shows the marginalized posteriors of spin χ for different injected values χ_{inj} . All of the fake observations are conducted once per day for 830 weeks, or 16 years, about an entire orbit.

From a marginalized posterior of black hole spin, 90% credible interval is calculated. The same procedure is repeated for different injected spin values. Fig 5 shows the credible interval of black hole spin as a function of injected spin value. Each bar is the 90% credible interval that corresponds to an injected dimensionless spin χ_{inj} and the big round dot in the bar is the best fit value of black hole spin for the observations of the orbit around the injected spin.

The uncertainty of measuring spin is about ± 0.3 at the 90% credible interval. If the black hole has spin lower than 0.3 or higher than 0.7, then the maximum a posteriori (MaP) spin will be offset from the true value both because of the noise in the orbital data and also due to the edge effect of the Gaussian distribution of the posterior as $\chi \in [0, 1]$. Many people believe that the Galactic center black hole has a high spin due to its accretion of matter of angular momentum and thus getting transferred to black hole spin. This systematic offset suggests the MaP spin point estimate may be a misleading summary statistic in the most astrophysically relevant scenario.

2.4.3 No-hair theorem

According to the black hole no-hair theorem, a black hole is completely characterized by its mass M , angular momentum (or spin) J , and charge q . For an astrophysical black hole which is electrically neutral, it is fully described by two quantities, M and J . As a consequence, the quadrupole moment Q_2 of its external spacetime is given by $Q_2 = -J^2/M$. The quadrupole moment can cause the stellar orbits around the black hole to precess, and the precession rate is on the order of μas for a highly eccentric orbit with orbital period of years which makes it possible for us to use the stellar orbit data from the modern infrared telescopes to test the no-hair theorem. In reality, there are perturbing external quadrupole moments Q_x (see Section II, V) due to the S star cluster, dark matter halos, and intermediate-mass black holes that are close to the SMBH, etc. This should also be taken into consideration. In this study, we employ the most optimistic possible scenario, equivalent to perfect knowledge of any external tidal potential.

In order to test the no-hair theorem, we treat the quadrupole moment of the black hole as an independent variable Q_2 that does not rely on J and M . Now we have $13 + 1$ parameters. By applying our MCMC program to the VLT orbital data of S2 we can obtain the marginalized posterior probabilities of spin J and quadrupole moment Q_2 , which are both flat distributions. This means current measurement accuracies and the amount of existing data are not sufficient for us to draw a conclusion on no-hair theorem. This is not surprising because we cannot even constrain spin yet.

What kind of observations of S2 will allow us to test the theorem in the future? Similar to what we do in Section IV, C, we assume that the black hole spin has some value (or injected value) and some direction, both of which are randomly chosen. We also assume the measurement accuracies take certain achievable values within a few years, specifically $\{\sigma_{\Delta\alpha} = \sigma_{\Delta\delta} = 10 \mu as, \sigma_{v_r} = 500 m/s\}$, and use our program to generate fake observed orbital data for an S2-ish star (same semi-major axis and eccentricity) around our SMBH with the assumed injected spin. This simulates the real observation scenarios. We virtually observe the S2-ish star once per day for 2000 weeks, which is nearly 40 years and about 2.5 orbits. We then use MCMC to obtain the marginalized posterior probability for Q_2 . We do the same for other choices of assumed injected spin values. The posteriors $p(Q_2)$ for different injected values of spin are all flat distributions. This means, we cannot constrain the quadrupole term or the no-hair theorem even if we observe S2 once per day for 40 years with the observation accuracy limit of GRAVITY telescope. This is mainly because the star is not close enough to the SMBH to be affected by the BH's quadrupole moments although its periapsis is at about $2500 M$ of SMBH. In order to use

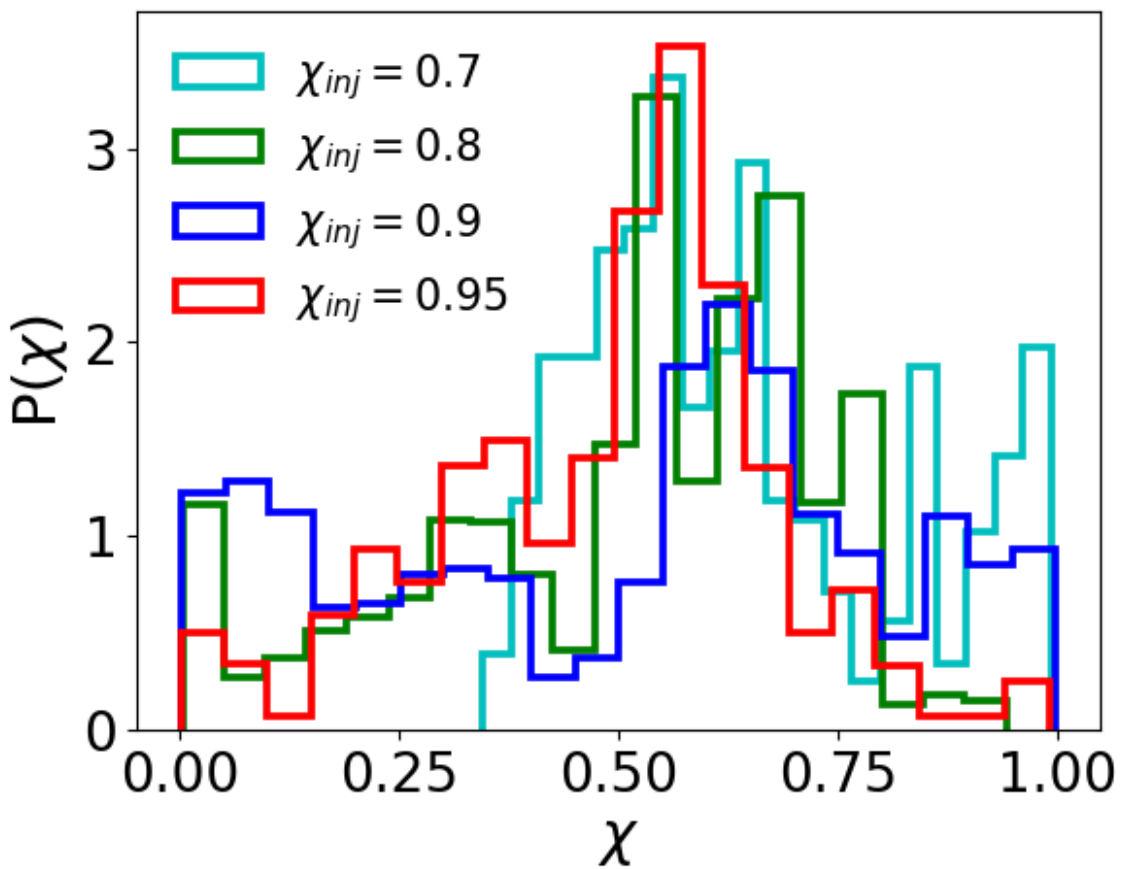
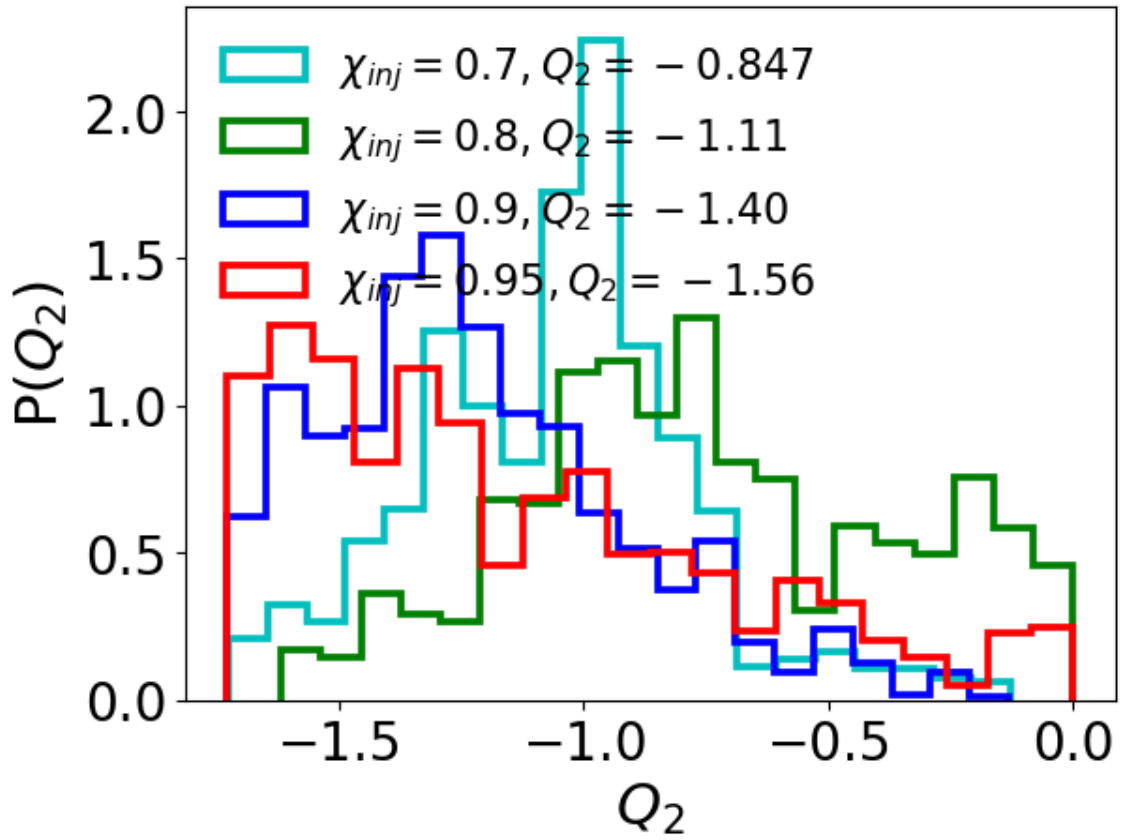


Figure 6 : The top figure shows the marginalized posteriors of quadrupole Q_2 with different injected values χ_{inj} and their corresponding injected quadrupole values $Q_{2,inj} = -\chi_{inj}^2 M^3$, where $M = 1.2M_*$. The bottom figure shows the posteriors of dimensionless spin χ for different injected values of χ . The measurement uncertainties are $\{\sigma_{\Delta\alpha} = \sigma_{\Delta\delta} = 10 \mu as, \sigma_{v_r} = 500 m/s\}$. The star has an orbit that is half the semi-major axis of S2 and the other parameters the same. It is observed once per week for an entire orbit of 300 weeks.

S2 to constrain quadrupole term Q_2 , we will have to improve our angular measurement accuracy, compared to GRAVITY's limits, by at least two orders of magnitude and the radial velocity accuracy by one order of magnitude.

Since S2 with even GRAVITY will not work, what kind of star orbits do we need to test the no-hair theorem then? We assume that we are lucky enough to find a star that has half the semi-major axis of S2 (500 AU) and all the other parameters the same as S2. This star has an orbital period of 285 weeks and we observe it once per week for 300 weeks in our simulation assuming that $\{\sigma_{\Delta\alpha} = \sigma_{\Delta\delta} = 10 \mu as, \sigma_{v_r} = 0.5 km/s\}$. If we injected different values of $Q_2 = -J^2/M$ with $J = \chi M^2$ and $M = 1.2M_*$ we can measure the quadrupole moment Q_2 as shown in Figure 6. In this figure, also plotted is the measurement of χ for various injected values.

2.5 Conclusions

Three main results come out of this work. Firstly, we conclude that we are not able to test the black hole spin and no-hair theorem with the current data from KECK and/or VLT observations up to 2009. Moreover, with the current best measurement accuracies, i.e., an angular accuracy of $40 \mu as$ and a radial velocity accuracy of $30 km/s$, we are neither able to tell whether the black hole spins even if we observe the orbit of S2 alone once per week for 100 years, nor are we able to tell whether the no hair theorem is correct if we observe S2 once per week for 400 years. The simulations for the above two cases simply return the priors, where we use flat priors in the parameters J and Q_2 .

Secondly, we give the strategies of future observations of how to test black hole spin with S2 observations. The strategies are based on future measurement accuracies. With the future observation accuracies of GRAVITY telescope if it is to point at the Galactic center, an angular accuracy of $10 \mu as$ and a radial velocity accuracy of $500 m/s$, we can test whether the black hole spins at 90% confidence if S2 is observed once per day for 16 years. However, we will still not be able to test the black hole no-hair theorem in 40 years or 2.5 full orbits using GRAVITY's measurement power with S2 as shown by another simulation.

Thirdly, we show that in order to test no-hair theorem with GRAVITY's resolution we need to find a closer star, such as a star that is half the distance or closer to the Galactic center and has other orbital parameters similar to that of S2 such that the orbits can be influenced much more by the spin and the quadrupole term of the black hole's gravitational potential. If the semi-major axis of the star is half that of the S2

and all other parameters the same, we can start to test whether no-hair theorem is valid within 6 years of weekly observations.

We also want to point out that the quadrupole moment of the potential is due to that of the black hole, but it could also be due to the observed stellar structure in the vicinity of Sgr A*, a dark matter halo or an intermediate mass black hole, which will be taken care of in the future work.

Appendix 2.A Equations of motion

In this appendix, we point out that different properties of an ensemble of stellar orbits probe different physics. For example, the orbit location probes different parts of the potential: distant orbits preferentially probe an external potential while nearby orbits probe the black hole. Similarly, different symmetry-breaking effects only occur from certain physical processes; for example, spherically symmetric potentials cannot cause the orbital plane to precess, while quadrupolar Newtonian potentials and frame dragging cause an ensemble of orbits to evolve in distinctly different ways. By isolating these symmetries and their impact on observations, we can easily model how a collection of measurements of several stellar orbits can best constrain properties of the galactic center environment.

In the text, we adopted simple approximations to general relativity at low post-Newtonian order, neglecting many common factors like the mass ratio. Because orbital perturbations we hope to identify are small, influences from small factors like mass ratio ($\simeq 10^{-6}$) can be of similar order to the minute effects we seek to identify at targeted separations. For this reason, in this section we carefully review relevant post-Newtonian expressions, targeting typical separations (i.e., 10 year orbits) and post-Newtonian accuracy ideally comparable to the targeted astrometric resolution of $\mu\text{as}/\text{yr}$ at 8 kpc (i.e., $\simeq 0.2M/\text{yr}$, or $\Delta v/c \simeq 10^{-7}$).

Post-Newtonian theory for binary and N-body motion is well-developed; see (Merriitt 2013) for a review in the context of stellar orbits around supermassive black holes; (Apostolatos et al. 1994) for a discussion of orbit-averaged spin-precession; and (Blanchet 2013), (Will 1985) for technically sophisticated and highly detailed discussions in general and for binary motion, specifically.

2.A.1 Post-Newtonian Two-body equations of motion

Working to v^2 (1PN) beyond Newtonian order in velocity and leading-order in spin-orbit coupling, the post-Newtonian Lagrangian for two-body motion has the form (Merritt 2013)

$$\mathcal{L} = \eta M \left[\frac{1}{2}v^2 + \frac{GM}{r} + \frac{1}{8}(1 - 3\eta)v^4 + \frac{GM}{2r}(3 + \eta)v^2 + \eta\dot{r}^2 - \frac{GM}{r} \right] + \mathcal{L}_{spin} + \mathcal{L}_{quad} \quad (2.A.1)$$

using units with $c = 1$ for simplicity. Here \mathcal{L}_{spin} and \mathcal{L}_{quad} terms are due to black hole spin and quadrupole moment. This Lagrangian corresponds to the Hamiltonian (Buonanno et al. 2006)

$$H = \mu[H_N + H_{1PN} + H_{SO}] \quad (2.A.2)$$

$$H_N = \frac{p^2}{2} - \frac{M}{r} \quad (2.A.3)$$

$$H_{1PN} = \frac{1}{8}(3\eta - 1)p^4 - \frac{1}{2}((3 + \eta)p^2 + \eta p_r^2)\frac{M}{r} + \frac{M^2}{2r^2} \quad (2.A.4)$$

$$H_{SO} = 2\frac{\mathbf{L}_N/\mu \cdot \mathbf{J}}{r^3} \quad (2.A.5)$$

These approximations, plus the limit $\eta \rightarrow 0$, reproduce the equations of motion adopted in the text. These Hamiltonian expressions also enable straightforward derivation of the orbit-averaged precession equations. As a concrete example, the contribution of black hole spin to the orbit-averaged precession equations for L_N, A_N follow from the Lie algebra

$$(\partial_t L_a)_{SO} = \{L_a, H_{SO}\} = \frac{2\epsilon_{abc}J_b L_c}{r^3} \quad (2.A.6)$$

$$\begin{aligned} (\partial_t A_a)_{SO} &= \{(p \times L - M\hat{r})_a, H_{SO}\} = \{(p \times L - M\hat{r})_a, \frac{1}{r^3}\}(2\vec{J} \cdot \vec{L}) + \{(p \times L - M\hat{r})_a, L_d\}2J_d/r^3 \\ &= -3\frac{\epsilon_{abc}r_b L_c}{r^5}(2\vec{J} \cdot \vec{L}) + \epsilon_{abc}\frac{2J_b}{r^3}A_c \end{aligned} \quad (2.A.7)$$

using $\{L_a, V_b\} = \epsilon_{abc}V_c$ for any vector V rotating with L (here, $\vec{L}, \vec{p}, \vec{r}$). Both orbit averages can be performed trivially, substituting $\vec{r} = p(\hat{x} \cos \theta + \hat{y} \sin \theta)/(1 + e \cos \theta)$ and $dt = d\theta L/r^2$ for the special case $\vec{A} = e\hat{x}$; we find

$$\langle r^{-3} \rangle = \frac{2\pi}{P} \frac{M}{p^3} \quad (2.A.8)$$

$$\langle r \cos \theta r^{-5} \rangle = \frac{2\pi}{P} \frac{eM}{p^3} \quad (2.A.9)$$

Critically, the second term does *not* orbit-average to zero. We therefore find

$$\langle (\partial_t A)_{SO} \rangle = \frac{2M}{p^3} \left[\vec{J} - 3(\vec{J} \cdot \hat{L})\hat{L} \right] \times A \quad (2.A.10)$$

Are these approximations adequate? First and foremost, as emphasized in the text, most post-Newtonian and mass ratio effects do not break symmetry in a way that can be confused with the influence of precession: even if they *did* matter quantitatively, they wouldn't matter qualitatively. Second, for a *single* star, the back-reaction of the star on the BH's orbit is small at typical high mass ratio ($\eta \simeq 10^{-6}$); the leading-order effect is purely Newtonian, corresponding to orbits around the center of mass; and higher-order PN effects are suppressed by $O(v^2) \simeq M/r \simeq 10^2 - 10^3$. For a single star, the finite mass ratio is a minute perturbation at separations where precession can be measured astrometrically; see 3.

As emphasized in the text, however, this modification does not break symmetry and therefore does not significantly influence the quantitative accuracy to which precession-induced modulations can be measured.

2.A.2 Post-Newtonian N-body equations of motion

When many bodies are included, we must carefully account for the often significant perturbations from neighboring stars, as well as the collectively weakly significant reaction of the black hole to the ambient stellar potential.

Finally, the BH spin will precess to conserve total angular momentum as the stars precess (Merritt 2013) due to Lens-Thirring effects, as well due to the ambient gravitational potential (Han, W.-B 2014). As the spin precesses, the leading-order spin-orbit precession will be modulated, an effect that can be comparable to quadrupolar precession effects from the central supermassive black hole.

Appendix 2.B Fisher matrix for Newtonian orbits

To constrain properties of the galactic center, we must first identify the Newtonian orbit. In this section we review how to calculate the Fisher matrix for Newtonian orbital parameters using our toy-model likelihood equation for special cases and in relative generality.

2.B.1 Fisher matrix for Keplerian orbits

In the discussion above, we adopted as coordinates the initial velocity and position. This choice of coordinates is particularly compatible with our equations of motion and subsequent analytic calculations (e.g., including non-Newtonian perturbations). While straightforward for brute-force calculations, the above approach is rarely analytically

tractable. Alternatively, the perturbed orbit Δr can be reduced to (a) changes of a, e and the Newtonian orbital phase Φ_o and (b) changes in the orientation of the orbit. Using the chain rule, we can build up the total perturbation as a additive contributions from both factors, each individually simple and particularly tractable in suitable coordinates.

Specifically, using as coordinates the orientation of the orbital frame (3 parameters) as well as a, e, Φ_o (3 parameters), we can express

$$\Delta \vec{r}(t) = \vec{C}_a(t)\Delta a + \vec{C}_e\Delta e + \vec{C}_\Phi\Delta\Phi_o + (-i\mathcal{L}_\beta\vec{r})\Delta\Theta^\beta \quad (2.B.1)$$

where $C_{\alpha,X}$ for $\alpha = x, y, z$ are the Cartesian components of the vectors \vec{C}_X and where $\Delta\Theta^\beta$ is a small (constant) rotation vector and \mathcal{L}_α are the generators of rotations. As a concrete example, for circular orbits $\vec{r} = a(\cos\Omega_N t\hat{x} + \sin\Omega_N t\hat{y})$

$$\vec{C}_a = \hat{r} + \frac{\partial\Omega_N}{\partial a}ta\hat{v} \quad (2.B.2)$$

$$\vec{C}_\Phi = a\hat{v} \quad (2.B.3)$$

$$\vec{C}_e = 0.5a\{-3 + \cos(2\Omega_N t)\}\hat{x} + \sin(2\Omega_N t)\hat{y} \quad (2.B.4)$$

$$-i\mathcal{L}_x\vec{r} = [\hat{y}\hat{z} - \hat{z}\hat{y}]_{ab}\vec{r}_b = -a\hat{z}(\hat{r} \cdot \hat{y}) \quad (2.B.5)$$

$$-i\mathcal{L}_y\vec{r} = [-\hat{x}\hat{z} + \hat{z}\hat{x}]_{ab}\vec{r}_b = a\hat{z}(\hat{r} \cdot \hat{x}) \quad (2.B.6)$$

$$-i\mathcal{L}_z\vec{r} = [\hat{x}\hat{y} - \hat{y}\hat{x}]_{ab}\vec{r}_b = a\hat{x}(\hat{r} \cdot \hat{y}) - a\hat{y}(\hat{r} \cdot \hat{x}) = -a\hat{v} \quad (2.B.7)$$

and rotations around z are degenerate with the change in orbital reference phase Φ_o .

In terms of these coordinates, the Fisher matrix for the idealized measurements in Eq. (2.C.1) can be expressed in the particularly analytically tractable form

$$\Gamma_{\alpha\beta} = \frac{N}{\sigma_r^2} \begin{bmatrix} \int \frac{dt}{T} \sum_b C_{b,a}C_{b,a} & \int \frac{dt}{T} \sum_b C_{b,a}C_{b,e} & \int \frac{dt}{T} \sum_b C_{b,a}C_{b,\Phi} & \int \frac{dt}{T} \sum_b C_{b,a}[-i\mathcal{L}_\beta\vec{r}]_b \\ \int \frac{dt}{T} \sum_b C_{b,e}C_{b,a} & \int \frac{dt}{T} \sum_b C_{b,e}C_{b,e} & \int \frac{dt}{T} \sum_b C_{b,e}C_{b,\Phi} & \int \frac{dt}{T} \sum_b C_{b,e}[-i\mathcal{L}_\beta\vec{r}]_b \\ \int \frac{dt}{T} \sum_b C_{b,\Phi}C_{b,a} & \int \frac{dt}{T} \sum_b C_{b,\Phi}C_{b,e} & \int \frac{dt}{T} \sum_b C_{b,\Phi}C_{b,\Phi} & \int \frac{dt}{T} \sum_b C_{b,\Phi}[-i\mathcal{L}_\beta\vec{r}]_b \\ \int \frac{dt}{T} \sum_b C_{b,a}[-i\mathcal{L}_\beta\vec{r}]_b & \int \frac{dt}{T} \sum_b C_{b,e}[-i\mathcal{L}_\beta\vec{r}]_b & \int \frac{dt}{T} \sum_b C_{b,\Phi}[-i\mathcal{L}_\beta\vec{r}]_b & \int \frac{dt}{T} [\mathcal{L}_\alpha\vec{r}] \cdot [\mathcal{L}_\beta\vec{r}] \end{bmatrix} \quad (2.B.8)$$

We confirm this representation reproduces the results provided above. Being analytically tractable even for eccentric orbits, this general form is particularly well-suited to marginalization via Eq. (2.3.8).

For circular orbits, the expressions involved can be approximately evaluated, using

the following rules

$$\langle \hat{r}_a \hat{r}_b \rangle = \frac{1}{2} [\delta_{ab} - \hat{L}_a \hat{L}_b] \quad (2.B.9)$$

$$\langle \hat{v}_a \hat{v}_b \rangle = \frac{1}{2} [\delta_{ab} - \hat{L}_a \hat{L}_b] \quad (2.B.10)$$

$$\langle \hat{r}_a \hat{v}_b \rangle = 0 \quad (2.B.11)$$

and by applying these rules, we find

$$\Gamma_{aa} = \frac{N}{\sigma_r^2} \int \frac{dt}{T} \sum_b C_{b,a} C_{b,a} = \frac{N}{\sigma_r^2} \int \frac{dt}{T} (1 + t^2 a^2 (\partial \Omega_N / \partial a)^2) \quad (2.B.12)$$

$$\Gamma_{\Phi\Phi} = \frac{Na^2}{\sigma_r^2} \quad (2.B.13)$$

$$\Gamma_{ee} = \frac{5Na^2}{2\sigma_r^2} \quad (2.B.14)$$

$$\Gamma_{ae} = 0 \quad (2.B.15)$$

$$\Gamma_{a\Phi} = \Gamma_{a\Theta_z} = \frac{N}{\sigma_r^2} \int \frac{dt}{T} t a^2 (\partial \Omega_N / \partial a) \quad (2.B.16)$$

$$\Gamma_{e\Phi} = 0 \quad (2.B.17)$$

$$\Gamma_{\Theta_x a} = \Gamma_{\Theta_y a} = \Gamma_{\Theta_x e} = \Gamma_{\Theta_y e} = \Gamma_{\Theta_x \Phi} = \Gamma_{\Theta_y \Phi} = 0 \quad (2.B.18)$$

$$\Gamma_{\Theta_x \Theta_x} = \Gamma_{\Theta_y \Theta_y} = \frac{Na^2}{2\sigma_r^2} \quad (2.B.19)$$

$$\Gamma_{\Theta_x \Theta_y} = \frac{Na^2}{\sigma_r^2} \quad (2.B.20)$$

$$\Gamma_{\Phi \Theta_z} = -\frac{Na^2}{\sigma_r^2} \quad (2.B.21)$$

The terms in this circular-orbit Fisher matrix have qualitatively different behavior. On the one hand, changes in the orbital period (a) lead to significant, increasing dephasing across multiple orbits; as a result, the orbital radius can be measured with high accuracy, increasing rapidly as the measurement interval increases [$\Gamma_{aa} \propto (\omega t)^2 N (a/\sigma_r)^2$]. By contrast, all other changes in a circular orbit are *geometrical*, producing *small or variable* separations. While our ability to measure these parameters also increases with the number of measurements ($\propto N \propto T$), the accuracy to which these parameters can be measured is significantly smaller. Finally, the circular-orbit Fisher matrix decomposes trivially into diagonal terms (almost all) plus one 2×2 block ($\ln a, \Phi$); this nearly-degenerate 2×2 block can be trivially diagonalized

$$\Gamma_{ab} = \frac{Na^2}{\sigma_r^2} \begin{bmatrix} 1 + \frac{T^2}{3} a (\partial_a \Omega)^2 & \frac{T}{2} a (\partial_a \Omega) \\ \frac{T}{2} a (\partial_a \Omega) & a^2 \end{bmatrix} = \frac{Na^2}{\sigma_r^2} \begin{bmatrix} 1 + \frac{3}{4} \Phi_{orb}^2 & -\frac{9}{8} \Phi_{orb} \\ -\frac{9}{8} \Phi_{orb} & \frac{9}{4} \Phi_{orb}^2 \end{bmatrix} \quad (2.B.22)$$

using $Ta\partial_a\Omega_N = -3\Phi_{orb}/2$ for $\Phi_{orb} = \Omega_N t$ the orbital phase. The relative significance of the two terms depends on how many orbital cycles have occurred.

2.B.2 Unknown black hole mass

Adding additional parameters, like the black hole mass, is straightforward:

$$\Delta\vec{r}(t) = \sum_A \vec{C}_\lambda \Delta\lambda \quad (2.B.23)$$

For circular orbits, the effect of a perturbed black hole mass is *very similar* to a perturbed orbital separation, producing a significant dephasing with time without any (small) change in position:

$$\vec{C}_M = \frac{\partial\Omega_N}{\partial M} ta\hat{v} \quad (2.B.24)$$

Because the Newtonian orbital period only depends on $\sqrt{M/a^3}$, these two parameters are nearly degenerate in the Fisher matrix: we can only measure one combination (the orbital period!) reliably. Marginalizing out the unknown orbital radius a , we find the Fisher matrix for black hole parameters does *not* depend as sensitively on the stellar mass. For circular orbits specifically, all parameters except M, a, Φ separate, allowing us to marginalize only a 3-dimensional matrix

$$\Gamma_{MM} = \frac{Na^2t^2}{3\sigma_r^2} \left(\frac{\partial\Omega_N}{\partial M} \right)^2 \quad (2.B.25)$$

2.B.3 Unknown black hole spin

The black hole spin enters via $\vec{\Omega}$ in a particularly simple way at leading order: $\partial\Omega^\alpha/\partial J_\beta = \delta_\beta^\alpha Z_J$. For example, the Fisher matrix over J components has the form

$$\Gamma_{\alpha\beta} = \frac{N}{\sigma_r^2} \int \frac{dt}{T} \frac{\partial\Omega^\alpha}{\partial J^\alpha} \frac{\partial\Omega^\beta}{\partial J^\beta} \langle t^2 [\mathcal{L}_a r_o] \cdot [\mathcal{L}_b r_o] \rangle \quad (2.B.26)$$

$$\simeq \frac{N}{\sigma_r^2} \frac{\partial\Omega^\alpha}{\partial J^\alpha} \frac{\partial\Omega^\beta}{\partial J^\beta} \frac{T^2}{3} \text{Tr}[\mathcal{L}_a I \mathcal{L}_b^T] \quad (2.B.27)$$

$$\simeq \frac{NZ_J^2 T^2}{3\sigma_r^2} \int_0^P \frac{dt}{P} \text{Tr}[\mathcal{L}_a I \mathcal{L}_b^T] \quad (2.B.28)$$

$$= \frac{NZ_J^2 T^2 [a(1-e^2)]^4}{3\sigma_r^2 PL} \text{Tr}[\mathcal{L}_a (A_1 \hat{x}\hat{x} + (A_2 - A_1)\hat{y}\hat{y}) \mathcal{L}_b^T] \quad (2.B.29)$$

where

$$A_1 \equiv \int_0^{2\pi} d\theta \frac{\cos^2 \theta}{(1 + e \cos \theta)^4} = \frac{(1 + 4e^2)\pi}{(1 - e^2)^{7/2}} \quad (2.B.30)$$

and

$$A_2 \equiv \int_0^{2\pi} d\theta \frac{1}{(1 + e \cos \theta)^4} = \frac{(2 + 3e^2)\pi}{(1 - e^2)^{7/2}} \quad (2.B.31)$$

Both integrals can be performed analytically when T/P is an integer; in this special case we find

$$A_2 \simeq \frac{T}{P} \int_0^{2\pi} d\theta \frac{1}{(1 + e \cos \theta)^4} = 2\pi T/P \frac{(1 + \frac{3}{2}e^2)}{(1 - e^2)^{7/2}} \quad (2.B.32)$$

$$A_1 = \pi T/P \frac{1 + 4e^2}{(1 - e^2)^{7/2}} \quad (2.B.33)$$

Using the explicit form of the generators \mathcal{L} in this frame, we find

$$\text{Tr}[\mathcal{L}_a(A_1 \hat{x}\hat{x} + (A_2 - A_1)\hat{y}\hat{y})\mathcal{L}_b^T] = \begin{bmatrix} A_2 - A_1 & 0 & 0 \\ 0 & A_1 & 0 \\ 0 & 0 & A_2 \end{bmatrix} \quad (2.B.34)$$

The $\Gamma_{J_a J_b}$ is then a coefficient times a matrix

$$\Gamma_{J_a J_b} = \frac{2NT^2(1 - e^2)^{1/2}}{3\pi\sigma_r^2 a^4} \begin{bmatrix} A_2 - A_1 & 0 & 0 \\ 0 & A_1 & 0 \\ 0 & 0 & A_2 \end{bmatrix} \quad (2.B.35)$$

$$\Gamma_{aJ_x} = \frac{4\pi NT^2}{\sigma_r^2 a^5} \text{Tr}[(J_x \mathcal{L}_x + J_y \mathcal{L}_\dagger + J_z \mathcal{L}_z)[\hat{x}\hat{x} + \hat{y}\hat{y}]\mathcal{L}_x^T] \quad (2.B.36)$$

$$\Gamma_{aJ_y} = \frac{4\pi NT^2}{\sigma_r^2 a^5} \text{Tr}[(J_x \mathcal{L}_x + J_y \mathcal{L}_\dagger + J_z \mathcal{L}_z)[\hat{x}\hat{x} + \hat{y}\hat{y}]\mathcal{L}_y^T] \quad (2.B.37)$$

$$\Gamma_{aJ_z} = \frac{-8\pi NT^2}{\sigma_r^2 a^5} \text{Tr}[(J_x \mathcal{L}_x + J_y \mathcal{L}_\dagger + J_z \mathcal{L}_z)[\hat{x}\hat{x} + \hat{y}\hat{y}]\mathcal{L}_z^T] \quad (2.B.38)$$

$$\Gamma_{eJ_x} = \Gamma_{eJ_y} = 0 \quad (2.B.39)$$

$$\Gamma_{eJ_z} = \frac{NT}{\sigma_r^2 a} \quad (2.B.40)$$

$$\Gamma_{\Phi_0 J_x} = \Gamma_{\Phi_0 J_y} = \Gamma_{\Phi_0 J_z} = 0 \quad (2.B.41)$$

$$\Gamma_{\Theta_x J_x} = \frac{NT}{2\pi\sigma_r^2 a} \text{Tr}[\mathcal{L}_x[A_1 \hat{x}\hat{x} + (A_2 - A_1)\hat{y}\hat{y}]\mathcal{L}_x^T] \quad (2.B.42)$$

$$\Gamma_{\Theta_y J_y} = \frac{NT}{2\pi\sigma_r^2 a} \text{Tr}[\mathcal{L}_y[A_1 \hat{x}\hat{x} + (A_2 - A_1)\hat{y}\hat{y}]\mathcal{L}_y^T] \quad (2.B.43)$$

$$\Gamma_{\Theta_z J_z} = \frac{-NT}{2\pi\sigma_r^2 a} \text{Tr}[\mathcal{L}_z[A_1 \hat{x}\hat{x} + (A_2 - A_1)\hat{y}\hat{y}]\mathcal{L}_z^T] \quad (2.B.44)$$

Appendix 2.C Likelihood and MCMC

2.C.1 Bayesian formalism

To separate issues pertaining to measurement from physics from dynamics, we describe results using three measurement scenarios: (a) an idealized model, where the position or velocity of each star can be measured at known times, as if via an array of local observers surrounding the black hole; (b) a plausible model, where only the radial velocity and transverse angle can be measured, on known null rays; and (c) a model for pulsar timing.

Specifically, our first measurement model assumes each star's position \vec{r}_α is measured to be $\vec{x}_{\alpha,k}$ on times t_k with measurement error σ_r . We will henceforth use greek subscripts α to index stars *or* parameters; small roman subscripts like k to index measurements; and large roman symbols to denote vector components. Since local measurements are performed, the distance to the black hole (and astrometry) do not enter into the analysis. For this model, the probability distribution of the data is

$$p(\{d\}|\lambda) = (2\pi\sigma_r^2)^{-3N/2} \exp - \sum_{\alpha,k} \frac{(\vec{r}_\alpha(t_k|\lambda) - \vec{x}_k)^2}{2\sigma_r^2} \quad (2.C.1)$$

Because of its simplicity, we will use this analytically trivial model when illustrating how physics break degeneracies.

A more realistic measurement model accounts for the unknown distance to the galactic center; the unknown mass of the galactic center black hole; and the fact that only

projected sky positions $\vec{\theta}_k$ and radial velocities $v_{r,k}$ can be measured. For this model, the probability distribution of the data are

$$p(\{d\}|\lambda) = (2\pi\sigma_\theta^2)^{-2N/2} \exp - \sum_{\alpha,k} \frac{(P_\perp \vec{r}_\alpha(t_k|\lambda) - \vec{\theta}_k R)^2}{2\sigma_\theta^2} \\ \times (2\pi\sigma_v^2)^{-N/2} \exp - \sum_{\alpha,k} \frac{(\hat{N} \cdot \partial_t \vec{r}_\alpha(t_k|\lambda) - v_N)^2}{2\sigma_v^2} \quad (2.C.2)$$

combined with a prior for R , the distance to the galactic center. A more realistic model still accounts for light propagation time across the stellar orbit (Zhang et al. 2015); light bending near the black hole; note we are in harmonic coordinates; higher order terms in the doppler equation (Zucker & Alexander 2007; Zucker et al. 2006)

Finally, the orbit of a pulsar around a black hole can be reconstructed by timing. Pulsar timing corresponds to fitting a model to pulse arrival times, to insure they arrive in regular intervals in the source frame. Roughly speaking, the model corresponds to fitting the proper time of the pulsar's orbit, which can be measured to some accuracy.

2.C.2 Fisher matrix

To illustrate the mechanics of a Fisher matrix calculation, we employ the idealized measurement model of Eq. (2.C.1) in the special case that the observed data is exactly as predicted by some set of model parameters λ' [i.e., $\vec{x}_k = \vec{r}(t_k|\lambda')$]. Using a first-order Taylor series expansion $\vec{r}(t_k|\lambda) - \vec{r}(t_k|\lambda') \simeq \delta\lambda^b \partial \vec{r} / \partial \lambda_b$ for the position versus parameters λ , we find the conditional probability of the data given λ can be approximated by

$$\ln p(\{d\}|\lambda) = \text{const} - \frac{1}{2} \Gamma_{ab} \delta\lambda_a \delta\lambda_b \quad (2.C.3)$$

$$\Gamma_{ab} = \sum_{\alpha,k} \frac{1}{\sigma_r^2} \frac{\partial \vec{r}_\alpha}{\partial \lambda_a} \frac{\partial \vec{r}_\alpha}{\partial \lambda_b} \quad (2.C.4)$$

This expression applies in general, no matter how the solution $r(t)$ is solved or approximated. By using an approximate analytic solution – the orbit-averaged secular solution [Eq. (2.2.10)] – we can estimate the accuracy to which parameters can be measured using a simple orbit average over a Newtonian solution. For example, for parameters λ which do not appear in the unperturbed Newtonian solution, like the black hole spin J or external potential, the Fisher matrix takes the form

$$\Gamma_{ab} = \sum_k \frac{t_k^2}{\sigma_r^2} \frac{\partial \Omega^A}{\partial \lambda_a} \frac{\partial \Omega^B}{\partial \lambda_b} (-i\mathcal{L}_A \vec{r}_o(t_k))^C (-i\mathcal{L}_B \vec{r}_o(t_k))^C \quad (2.C.5)$$

In fact, as a first approximation, these components of Fisher matrix can be approximated using the orbit's moment of inertia $I_{ab,N} = \langle r_{0,a} r_{0,b} \rangle$:

$$\Gamma_{ab} \simeq \frac{t^3}{3N} \frac{\partial \Omega^A}{\partial \lambda_a} \text{Tr}[(-i\mathcal{L}_A) I (-i\mathcal{L}_A)^T] \quad (2.C.6)$$

Having estimated the Fisher matrix and hence approximated $p(\{d\}|\lambda)$ by a gaussian, we can further construct marginalized distributions for λ_A in $\lambda = (\lambda_A, \lambda_a)$ by integrating out the variables λ_a .

2.C.3 Toy model: tests in \vec{r} using MCMC

We show that MCMC and numerical and analytic Fisher agree via toy models: As a concrete example, in the Cartesian coordinates with its origin at the black hole center, $\{x_i, y_i, z_i\}$ as the observables, we model a Newtonian circular orbit with parameters $a, e, \Phi_0, \alpha, \beta$, and an elliptical orbit with $a, e, \Phi_0, \alpha, \beta, \gamma, J_x, J_y, J_z$. Figure 7 shows the results of measuring the semi-major axis of a circular orbit, treating only the semi-major axis as uncertain and treating all orbital parameters as uncertain. It also shows the results of measuring the magnitude of black spin.

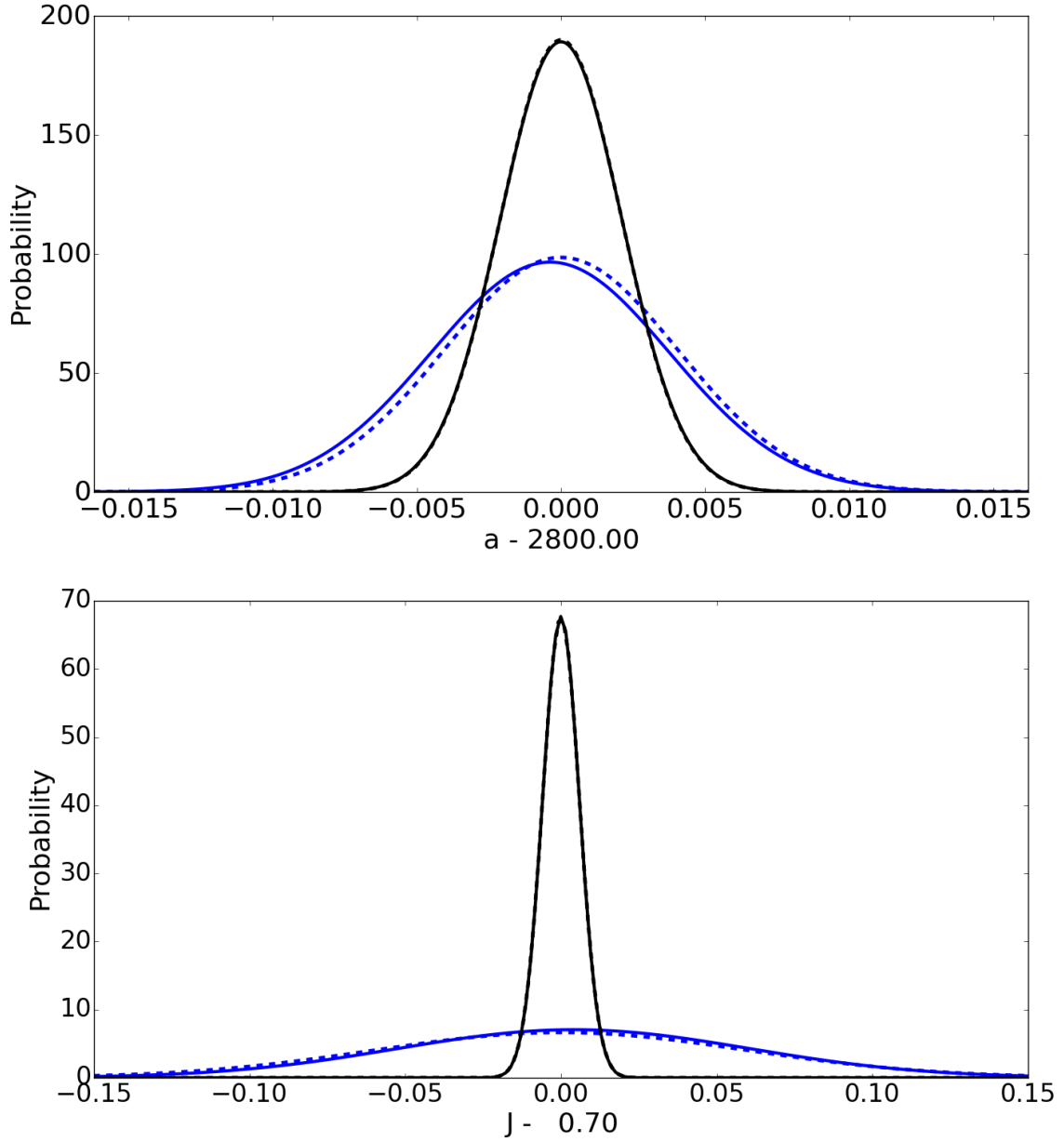


Figure 7 : Measuring properties of an orbit and a BH: circular orbits: *Top panel*: Demonstration of how accurately a Newtonian circular orbits' radius can be measured, assuming the only unknown parameter is the orbital radius (black) and assuming no parameters are known (blue). For comparison, the dotted curves show the results of our Fisher matrix calculations. This figure uses simplified measurement model of Eq. (2.C.1), with $a = 2800M$, $N = 700$, $\sigma_r = 1.0M$, $e = 0.01$, $T = 100$ weeks, $\Delta t = 1$ day. *Bottom panel*: Demonstration of how accurately the black hole spin J can be measured, assuming the only unknown parameter is the black hole spin magnitude $\chi = J/M^2$ and assuming both the orbit and black hole spin vector are unknown (blue). Evaluated using the same initial parameters as above, except $\sigma_r = 0.1M$ and evolved according to Eq. (2.2.1).

Chapter 3

Testing Chameleon Field Theory with Cepheids in Extragalactic Dwarf Galaxies

3.1 Introduction

3.1.1 History of the Problem

Einstein's theory of general relativity (GR) has been tested on the scales ranging from millimeter to the solar system (Will 2005). The spectacular discovery of the acceleration of the Universe fifteen years ago has motivated modified theories of gravity (MG) on large scales such as galactic and cosmological scales.

These attempts introduce a new scalar degree of freedom that is active on large scales but is screened on small scales to match experiments (Hui et al. 2009). One of them is called chameleon field that couples non-minimally to matter via a universal fifth force and leads to enhancements of the gravitational force (Jain et al. 2012), which is also cited as JVS in this dissertation. Through self-interactions and coupling to matter, chameleons have a mass that depends on the local matter density. This force is suppressed in high potential regions (screen) and not suppressed in low potential regions (unscreened).

The screening mechanism implies that modified gravity exist where Newtonian gravity

is weak. Viable screening theories make remarkable predictions aiming at testing the fundamental nature of gravity on a wide range of scales (Chang & Hui 2011, Khoury 2013). The oscillations of cepheids may exhibit the effects of MG, e.g., the changes in their pulsation frequencies (Jain et al. 2012, Sakstein 2013).

3.1.2 Chameleon Field Theory

There are two parameters in the chameleon field theory. One is ϕ_* which determines when the force is screened. If the magnitude of the Newtonian potential $\Phi_N \ll \phi_*$, then the object will be unscreened, otherwise the body will be screened. $\phi_* > 10^{-6}$ is ruled out observationally from the potential of the Sun and that of the Milky Way, both of which are about 2×10^{-6} .

The other parameter is α_c that sets the strength of the fifth force in unscreened regions. A completely unscreened object will feel a fifth force that is proportional to the Newtonian gravitational force and the combined force results in a rescaling of Newton's constant G (Jain et al. 2012)

$$G(r) = G(1 + \alpha_c) \quad (3.1.1)$$

For a partially screened object, the total force in the region exterior to the screening radius r_s can be described by a position dependent rescaling of G (Jain et al. (2012))

$$G(r) = G \left[1 + \alpha_c \left(1 - \frac{M(r_s)}{M(r)} \right) \right], \quad M(r) > M(r_s) \quad (3.1.2)$$

where $M(r_s)$ is the mass interior to the screening radius r_s , and $M(r)$ is the mass interior to radius r .

3.1.3 Cepheid Pulsations in GR

Cepheids are massive variable stars whose strong direct relation between their luminosities L and pulsation periods P secures their status as important standard candles for establishing the Galactic and extragalactic distance scales. Stars that have masses $M > 3M_\odot$ cross the Cepheid instability strip, a nearly vertical region that is determined by a star's surface effective temperature $T_{\text{eff}} = 6000 \text{ K}$. While in the instability strip, a Cepheid's

luminosity and radius oscillate with periods on the order of days to months. Observed Cepheids are typically $6M_{\odot}$ to $8M_{\odot}$ stars.

Stars can cross the instability strip multiple times, see Figure 9, which shows the post main sequence evolution of stars. The first crossing of the instability strip is before the star goes up the red giant branch. The second crossing of the instability strip is the first crossing after the tip of the red giant branch when the star is on the lower part of the blue loop. And the third crossing is when it is on the upper part of the blue loop. The second and third crossings of the strip, are probably where Cepheids properties are best understood.

The chapter is organized as follows: In Section 3.2 we introduce the methods we use to calculate the pulsations of Cepheids in both GR and MG. In Section 3.3, we demonstrate the period-temperature relationships of Cepheids obtained with our pulsation frequency solver from the MESA data. This is done in the regime of both GR and MG. We also compare our results with the JVS ansatz. In Section 3.4, we discuss the results and implications to constraints on modified gravity, and summarize the findings we make and list the future work.

3.2 Methods

3.2.1 Building Stars in Chameleon Gravity

We use the stellar evolution code MESA (Paxton et al. 2010) to account for the chameleon scalar field changes to the local gravity and calculate stellar evolutions under these conditions (Chang & Hui 2011). While the scalar field modifies many different aspects of stellar evolution, we focus on the Cepheids in the instability strips because the pulsating frequencies can be measured in distant galaxies. We calculate the pulsation periods of a Cepheid variable star at different surface effective temperatures T_{eff} using the stellar structure calculated by modified MESA.

3.2.2 Radial Pulsations in Chameleon Gravity

In this section we describe the matrix method for obtaining numerical solutions to the linear adiabatic wave equation (LAWE) for arbitrary equilibrium stellar models, see Appendix 3.A for details, and test the validity of the method with numerical implementations for certain selected stellar models with known analytic solutions.

We define $X_i \equiv \frac{\delta r_i}{r_i}$ to rewrite Eq. (3.A.4) for $r_{i+\frac{1}{2}} \gg dr = (r_{i+1} - r_i)$ as

$$\omega^2 X_i = A_i X_{i-1} + B_i X_i + C_i X_{i+1} \quad (3.2.1)$$

where

$$A_i = \frac{4\pi r_i}{DM_i} \Gamma_{1,i-\frac{1}{2}} P_{i-\frac{1}{2}} \left(\frac{3}{2} - \frac{r_{i-\frac{1}{2}}}{r_i - r_{i-1}} \right) \quad (3.2.2)$$

$$B_i = -\frac{4G_i m_i}{r_i^3} + \frac{4\pi r_i}{DM_i} \left[\Gamma_{1,i-\frac{1}{2}} P_{i-\frac{1}{2}} \left(\frac{3}{2} + \frac{r_{i-\frac{1}{2}}}{r_i - r_{i-1}} \right) - \Gamma_{1,i+\frac{1}{2}} P_{i+\frac{1}{2}} \left(\frac{3}{2} - \frac{r_{i+\frac{1}{2}}}{r_{i+1} - r_i} \right) \right] \quad (3.2.3)$$

$$C_i = - \left[\frac{4\pi r_i}{DM_i} \Gamma_{1,i+\frac{1}{2}} P_{i+\frac{1}{2}} \left(\frac{3}{2} + \frac{r_{i+\frac{1}{2}}}{r_{i+1} - r_i} \right) \right] \quad (3.2.4)$$

We use the boundary conditions, $\delta P = 0$, to get B_J ,

$$B_J = \frac{G_J M_J}{r_J^3} \left[-4 + \Gamma_{1,J} \left(\frac{3}{2} + \frac{r_{J-\frac{1}{2}}}{r_J - r_{J-1}} \right) \right] \quad (3.2.5)$$

and A_J

$$A_J = \frac{G_J M_J}{r_J^3} \Gamma_{1,J} \left(\frac{3}{2} - \frac{r_{J-\frac{1}{2}}}{r_J - r_{J-1}} \right) \quad (3.2.6)$$

The matrix, written as Eq. (3.A.12), is solved numerically for the eigenvalues. The square root of the lowest eigenvalue, ω_0^2 , is the fundamental pulsating frequency of the Cepheid; the second lowest, ω_1^2 , is the first overtone, and so on.

We test our code by using polytropes with known analytic frequencies. We also compare the oscillating frequencies of Cepheids with the results using GYRE (Townsend & Teitler 2013), and the differences of the results between their code and ours for the first three eigenmodes are less than 0.01% for the same profile of a $6M_{\odot}$ Cepheid at $T_{\text{eff}} = 6000 K$.

3.3 Results

3.3.1 Stellar Structures in GR and MG

The scalar field can modify the structure of a Cepheid star during its stellar evolution. The change in effective G is given by

$$\Delta G = \langle G \rangle - G \quad (3.3.1)$$

where G is the Newtonian gravitational constant and $\langle G \rangle$ is given by averaging $G(r)$ with Jain et al. (2012)

$$\langle G \rangle = \frac{1}{R} \int_0^R G(r) dr \quad (3.3.2)$$

Table 2 shows the changes in effective G by chameleon fields that have different values of field parameters α_c and ϕ_* . The larger the α_c and ϕ_* are, the more the chameleons affect the rescaling of gravity.

Figure 8 shows the distributions of effective gravitational constant $G(r)$ inside Cepheids of $6M_{\odot}$ at effective temperature $T_{\text{eff}} \approx 6000K$. Each line is a profile of $G(r)$ of a Cepheid that has a metallicity of either $Z = 0.002$ or $Z = 0.02$. The radii of the Cepheids are scaled to 1.

Table 2 : The changes in effective G for different values of parameters α_c and ϕ_* for a $6M_\odot$ Cepheid at $T_{\text{eff}} \approx 6000K$ on the third crossing.

α_c	ϕ_*	$\Delta G/G$
1/3	10^{-8}	0.0024
1/3	10^{-7}	0.022
1/3	10^{-6}	0.17
1	10^{-8}	0.0072

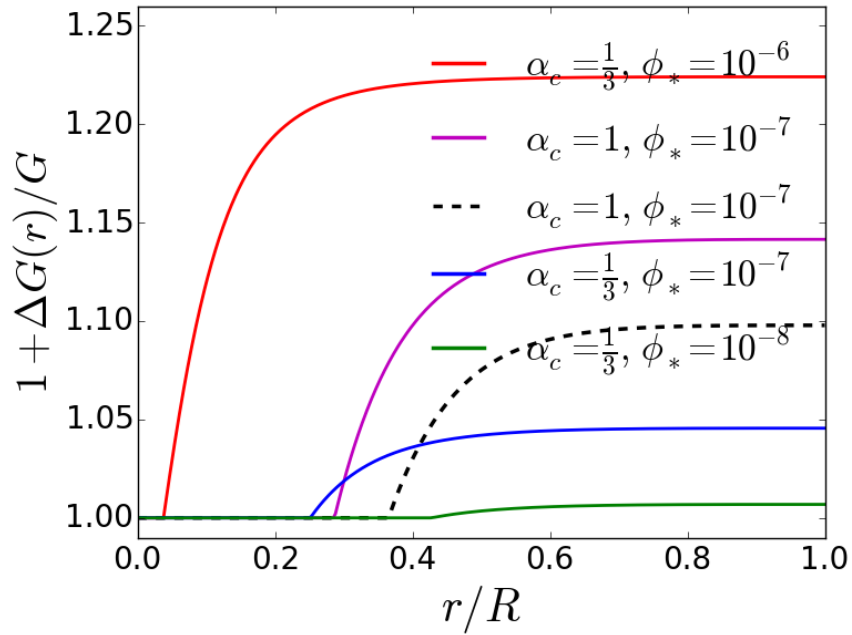


Figure 8 : The profiles of effective gravitational constant $G(r)$ for stars of $6M_\odot$ at $T_{\text{eff}} \approx 6000K$. The solid lines have metallicity $Z = 0.002$ and the dashed line has $Z = 0.02$. They are a third crossing Cepheids for $Z = 0.002$ and $\phi_* = 10^{-6}$ and a first crossing Cepheid for $Z = 0.02$ because they do not have the second crossings. The rest are second crossing Cepheids with $Z = 0.002$.

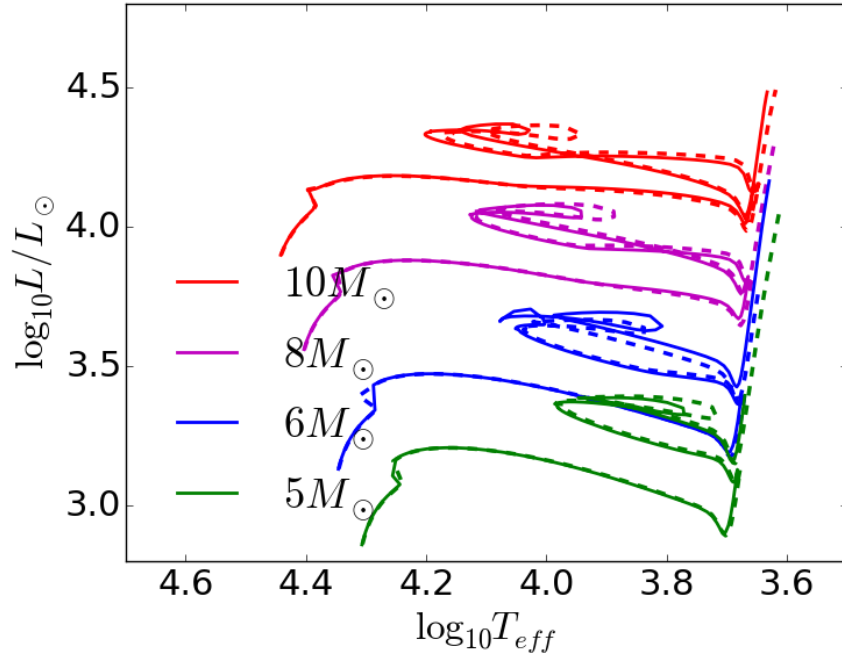


Figure 9 : The post-main sequence HR diagram (L - T_{eff}) for stars of masses $5M_{\odot}$ (green), $6M_{\odot}$ (blue), $8M_{\odot}$ (purple), and $10M_{\odot}$ (red) in both GR (dashed lines) and MG (solid lines) regimes. The chameleon field is $\alpha_c = \frac{1}{3}$ and $\phi_* = 10^{-7}$.

3.3.2 Eigenmodes of a Cepheid in GR and MG

Chameleon scalar fields, compared to GR, can change the eigenmodes of a Cepheid. Figure 10 shows for a $6M_{\odot}$ Cepheid the change in unperturbed radius, $\xi = dr/r_0$, as a function of radius that is scaled to one, and also the fundamental modes, first overtones, and second overtones of a Cepheid in different scalar fields ($\alpha_c = \frac{1}{3}$ and $\phi_* = 10^{-8}$, $\phi_* = 10^{-7}$, and $\phi_* = 10^{-6}$, respectively) at effective temperature $T_{\text{eff}} \approx 5900K$.

The effects of a chameleon scalar field on Cepheids' pulsation periods can be used to constrain the values of chameleon fields because period is a property of a Cepheid that can be measured accurately. We will discuss this in detail in Subsections 3.3.3 and 3.3.4.

3.3.3 Comparison with JVS ansatz

We compare our calculations of the Cepheids' oscillation frequencies with the ansatz given by JVS (Jain et al. 2012). Their ansatz states that the relation between the change in pulsation period and the modified is

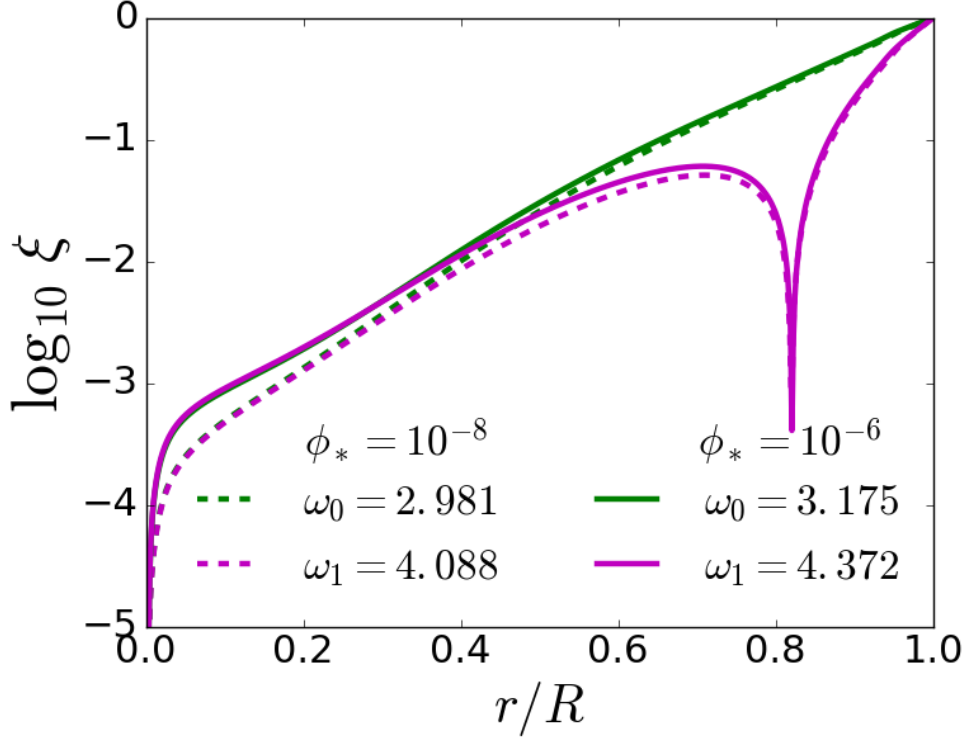


Figure 10 : The change in unperturbed radius, $\xi = dr/r_0$, of a $6M_{\odot}$ Cepheid as a function of radius and eigenmodes of Cepheids with metallicity $Z = 0.002$ in different chameleon fields, where $\alpha_c = \frac{1}{3}$ and ϕ_* varies. The stars on the top panel are at $T_{\text{eff}} \approx 5900K$ and the ones on the bottom panel (commented out in the draft) are at $T_{\text{eff}} \approx 6200K$. The dotted, dashed, and solid lines correspond to $\phi_* = 10^{-8}$, $\phi_* = 10^{-7}$, and $\phi_* = 10^{-6}$, respectively. The blue, purple, and green lines are fundamental modes, first overtones, and second overtones, respectively. The second and third crossings of instability strips are within the range of $3.73 < \log T_{\text{eff}} < 3.83$ or $5370K < T_{\text{eff}} < 6760K$.

$$\frac{\Delta\Pi}{\Pi} = -\frac{1}{2} \frac{\Delta G}{G} \quad (3.3.3)$$

where Π is the pulsating period of a Cepheid star, and ΔG is defined in Eq. 3.3.1.

Figure 11 shows the ratio of the change in fundamental period of a Cepheid due to a chameleon field to that without chameleon fields, $\Delta\Pi/\Pi_{\text{GR}}$, as a function of effective temperature of the Cepheid along its stellar evolution. The solid lines show our results while the dashed lines show the predictions from JVS's ansatz. Each subfigure shows this relation in a different chameleon field. From the top to bottom, the three scalar fields all have $\alpha_c = \frac{1}{3}$, but $\phi_* = 10^{-8}$, 10^{-7} , 10^{-6} , respectively. In this figure the Cepheids have metallicity $Z = 0.002$. We can see that the first two chameleon fields make a Cepheid star in the mass range $5M_{\odot}$ to $10M_{\odot}$ oscillate more quickly by 4% to 15%, depending on

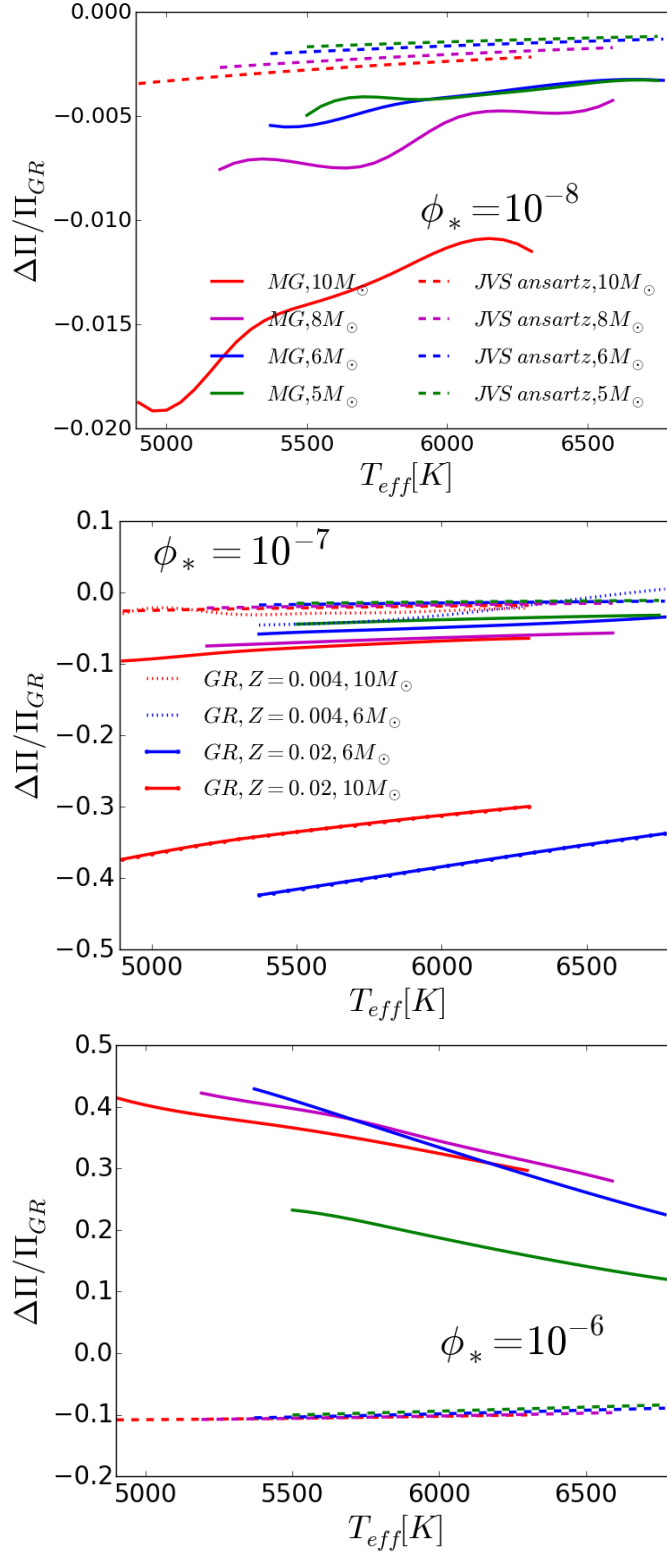


Figure 11 : The change in fundamental period $\Delta\Pi/\Pi_{GR}$ versus T_{eff} relations for stars of $5M_{\odot}$, $6M_{\odot}$, $8M_{\odot}$, and $10M_{\odot}$ with $\alpha_c = \frac{1}{3}$. Metallicity $Z = 0.002$ unless specified. The top figure has $\phi_* = 10^{-8}$, the middle figure has $\phi_* = 10^{-7}$, and the bottom figure has $\phi_* = 10^{-6}$. Solid lines are our MG results and dashed lines are plotted from JVS ansatz. The Cepheids in the first two subfigures are all at second crossings and in the third one are at the third crossings. In the second subfigure, the difference $\Delta\Pi$ are between $Z = 0.004$ and $z = 0.002$ in GR for the two dotted lines.

the mass and the temperature of the star and the scalar field it is in, whereas the third chameleon field speeds up the fundamental pulsations of a Cepheid by 12% to 45%.

We can note that the absolute values of the changes in fundamental modes due to the three scalar fields from our numerical calculations are a factor of 3 or 4 more than those predicted by JVS's ansatz for all stellar masses and temperatures. Moreover, we predict faster pulsations due to the first two scalars fields and slower pulsations due to the third scalar field, whereas they predict faster pulsations for all three scalar fields. The transition happens when $10^{-7} < \phi_* < 10^{-6}$ and $\alpha_c = \frac{1}{3}$. However, since the third scalar field is ruled out, the negative sign in Eq. 3.3.3 still holds in the regions where chameleons possibly exist.

3.3.4 Effects of metallicity

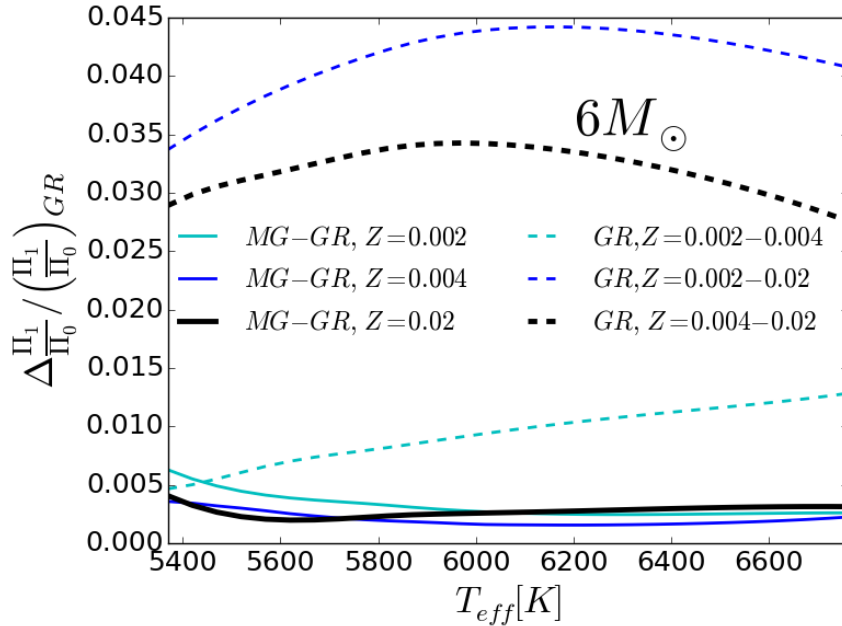


Figure 12 : The dependence of $\Delta \frac{\Pi_1}{\Pi_0} / \left(\frac{\Pi_1}{\Pi_0} \right)_{GR}$ vs T_{eff} relation on metallicity in GR regime, and on with and without a chameleon field of $\alpha_c = \frac{1}{3}$, $\phi_* = 10^{-7}$ for stars of $6M_\odot$.

Metallicity is another important factor that can change a star's pulsation modes and Π_1/Π_0 ratio, with other parameters of the star fixed. We show in Figure 12 the effects of metallicity of a $6M_\odot$ second crossing Cepheid star on its Π_1/Π_0 ratio. In both GR and MG regimes, with the latter has $\alpha_c = \frac{1}{3}$ and $\phi_* = 10^{-7}$, larger metallicity ($Z = 0.02$)

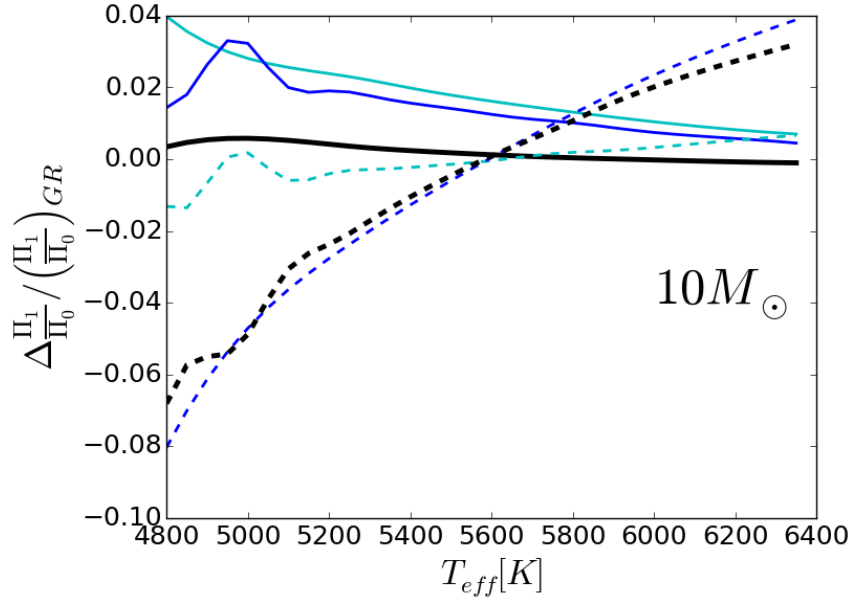


Figure 13 : The dependence of $\Delta \frac{\Pi_1}{\Pi_0} / \left(\frac{\Pi_1}{\Pi_0} \right)_{GR}$ vs T_{eff} relation on metallicity in GR regime, and on with and without a chameleon field of $\alpha_c = \frac{1}{3}, \phi_* = 10^{-7}$ for stars of $10M_{\odot}$.

increases this ratio by about 4% comparing to that of $Z = 0.002$. This is comparable to the effect of chameleon field, where with and without chameleons, the ratio Π_1/Π_0 is changed by about 1%. Therefore, it is very difficult to constrain the scalar field if our measurements of stars metallicities are not good enough. Yet this is usually the case because our tests work better when we use extragalactic galaxies, whose metallicities are usually not well determined - at least not good enough for our tests.

3.4 Discussions

In this section we discuss about the implications of the work for constraints on modified gravity. First, the MG theories modify the periods of Cepheids by a substantial amount, 12–45%. However, the metallicity of a star plays an equally important role as chameleon field does in the variations of a star's pulsation period. Therefore, the metallicity and MG effects are potentially difficult to disentangle.

Appendix 3.A Matrix Method

In this section we shall provide a matrix method for obtaining numerical solutions to the linear adiabatic wave equation (LAWE) for arbitrary equilibrium stellar models, and shall test the validity of the method with numerical implements for certain selected stellar models with known analytic solutions.

We start with three equations (Cox 1980): Eq. (5.36),

$$\frac{\delta P}{P_0} = \Gamma_{1,0} \frac{\delta \rho}{\rho_0} \quad (3.A.1)$$

where the subscript 0 means the unperturbed solutions, Eq. (7.4)

$$\frac{\delta \rho}{\rho_0} = -3\xi - r_0 \frac{\partial \xi}{\partial r_0} \quad (3.A.2)$$

where $\xi = \frac{\delta r}{r_0}$, and Eq. (8.60),

$$\omega^2 \delta r_i = -\frac{4G_i m_i}{r_i^3} \delta r_i + 4\pi r_i^2 \frac{(\delta P)_{i+\frac{1}{2}} - (\delta P)_{i-\frac{1}{2}}}{DM_i} \quad (3.A.3)$$

where m_i is the mass interior to the interface i , and $DM_i \equiv \frac{1}{2}(m_{i-\frac{1}{2}} + M_{i+\frac{1}{2}})$ is the "effective" mass that determines the inertia associated with the i^{th} interface, where $M_{i-\frac{1}{2}}$ is the mass of the i^{th} zone, which is between the $i-1^{\text{th}}$ and i^{th} interfaces. The zones are numbered $1, 2, \dots, J$, from the inside out, and there are $J+1$ interfaces, numbered $0, 1, 2, \dots, J$.

By defining $X_i \equiv \frac{\delta r_i}{r_i}$, we can rewrite Eq. (3.A.3) as

$$\omega^2 X_i = -\frac{4G_i m_i}{r_i^3} X_i + 4\pi r_i \frac{(\delta P)_{i+\frac{1}{2}} - (\delta P)_{i-\frac{1}{2}}}{DM_i} \quad (3.A.4)$$

Plugging Eq. (3.A.2) into Eq. (3.A.1) and using $X_i \equiv \frac{\delta r_i}{r_i}$, we have

$$(\delta P)_{i+\frac{1}{2}} = -\Gamma_{1,i+\frac{1}{2}} P_{i+\frac{1}{2}} \left(3X_{i+\frac{1}{2}} + r_{i+\frac{1}{2}} \frac{X_{i+1} - X_i}{r_{i+1} - r_i} \right) \quad (3.A.5)$$

and substituting this into Eq. (3.A.4), we can express $X_{i\pm\frac{1}{2}}$ in terms of $X_{i\pm 1}$ and X_i for $r_{i+\frac{1}{2}} \gg (r_{i+1} - r_i)$ and then rewrite Eq. (3.A.4) as

$$\omega^2 X_i = A_i X_{i-1} + B_i X_i + C_i X_{i+1} \quad (3.A.6)$$

where

$$A_i = \frac{4\pi r_i}{DM_i} \Gamma_{1,i-\frac{1}{2}} P_{i-\frac{1}{2}} \left(\frac{3}{2} - \frac{r_{i-\frac{1}{2}}}{r_i - r_{i-1}} \right) \quad (3.A.7)$$

$$B_i = -\frac{4G_i m_i}{r_i^3} + \frac{4\pi r_i}{DM_i} \left[\Gamma_{1,i-\frac{1}{2}} P_{i-\frac{1}{2}} \left(\frac{3}{2} + \frac{r_{i-\frac{1}{2}}}{r_i - r_{i-1}} \right) - \Gamma_{1,i+\frac{1}{2}} P_{i+\frac{1}{2}} \left(\frac{3}{2} - \frac{r_{i+\frac{1}{2}}}{r_{i+1} - r_i} \right) \right] \quad (3.A.8)$$

$$C_i = - \left[\frac{4\pi r_i}{DM_i} \Gamma_{1,i+\frac{1}{2}} P_{i+\frac{1}{2}} \left(\frac{3}{2} + \frac{r_{i+\frac{1}{2}}}{r_{i+1} - r_i} \right) \right] \quad (3.A.9)$$

Note: Cox says that the matrix is symmetric. However, in our notation A_{i+1} cannot possibly be equal to C_i . — This is because we define X_i in a different way than they do.

Notice that we cannot get A_0 , B_0 , B_J , and C_J directly from their definitions thus the first row of the matrix given by Eq.'s (3.A.7), (3.A.8), and (3.A.9) does not exist, but for the matrix elements on the surface we can use the boundary conditions to get B_J ,

$$B_J = \frac{G_J M_J}{r_J^3} \left[-4 + \Gamma_{1,J} \left(\frac{3}{2} + \frac{r_{J-\frac{1}{2}}}{r_J - r_{J-1}} \right) \right] \quad (3.A.10)$$

and for A_J we have

$$A_J = \frac{G_J M_J}{r_J^3} \Gamma_{1,J} \left(\frac{3}{2} - \frac{r_{J-\frac{1}{2}}}{r_J - r_{J-1}} \right) \quad (3.A.11)$$

Therefore, the matrix is

$$\begin{pmatrix} B_1 & C_1 & 0 & 0 & 0 & 0 \\ A_2 & B_2 & C_2 & 0 & 0 & 0 \\ 0 & A_k & B_k & C_k & 0 & 0 \\ 0 & 0 & A_{J-2} & B_{J-2} & C_{J-2} & 0 \\ 0 & 0 & 0 & A_{J-1} & B_{J-1} & C_{J-1} \\ 0 & 0 & 0 & 0 & A_J & B_J \end{pmatrix} \quad (3.A.12)$$

The square root of the lowest eigenvalue ω_0^2 of matrix (3.A.12) is the fundamental pulsating mode of the Cepheid, and that of the second lowest ω_1^2 is the first overtone, and so on. The eigenvalues are solved numerically.

Polytropes: The validity of the code is checked by using polytropes. We perturb those stars to obtain their pulsating eigenmodes numerically and compare them with the analytic solutions in Cox's Table 8.1.

The shape of the pressure of a polytrope as a function of radius r is

$$P(r) = K_0 \rho(r)^{\frac{n+1}{n}} \quad (3.A.13)$$

where K_0 is a constant and n is an index.

The constant K_0 is given by taking the values at the center of the star,

$$\frac{\rho_c}{m_p} kT = P_c = K_0 \rho_c^{\frac{n+1}{n}} \quad (3.A.14)$$

which results in

$$K_0 = \frac{\rho_c^{\frac{1}{n}}}{m_p} kT_c \quad (3.A.15)$$

where m_p is the mass of a proton, k is a constant, and T_c is the temperature at the center of the star, which can be taken as the temperature at the center of the Sun.

The general form for pressure is

$$P(r) = \frac{\rho_c^{\frac{1}{n}}}{m_p} kT_c \rho(r)^{\frac{n+1}{n}} \quad (3.A.16)$$

and central pressure

$$P_c = \frac{\rho_c^{\frac{n+2}{n}}}{m_p} kT_c . \quad (3.A.17)$$

For $n = 3$, the constant K_0 is

$$K_0 = \frac{\rho_c^{\frac{1}{3}}}{m_p} kT_c \quad (3.A.18)$$

and the pressure is

$$P(r) = K_0 \rho(r)^{\frac{4}{3}} = \frac{\rho_c^{\frac{1}{3}}}{m_p} k T_c \rho(r)^{\frac{4}{3}} . \quad (3.A.19)$$

We also have

$$\frac{dP}{dr} = -\frac{GM(r)}{r^2} \rho(r) \quad (3.A.20)$$

$$\frac{dM}{dr} = 4\pi r^2 \rho(r) . \quad (3.A.21)$$

For small r , say $r = 10,000 \text{ cm}$,

$$M(r) = \frac{4\pi}{3} r^3 \rho_c . \quad (3.A.22)$$

For small r , we have $\rho(r) = \rho_c$ and plug into the above equation for $M(r)$

$$P(r) - P_c = -\frac{GM(r)}{r^2} \rho(r) r = -\frac{4\pi}{3} G r^2 \rho_c^2 . \quad (3.A.23)$$

Once we have P_c , ρ_c , and $\frac{dP}{dr}|_c$, we can evolve for $P(r)$, $\rho(r)$, and $M(r)$. Then we can solve for the perturbation solutions.

The other method is taking $M(r)$ as the variable to get $P(M)$. We have

$$\frac{dP}{dM} \frac{dM}{dr} = -\frac{GM(r)}{r^2} \quad (3.A.24)$$

plug (3.A.21) into the above equation and get

$$\frac{dP}{dM} = -\frac{GM(r)}{r^2} \frac{dr}{dM} = -\frac{GM(r)}{4\pi r^2} \quad (3.A.25)$$

Figure 14 shows our numerical solutions using the matrix method comparing to the pulsating frequencies of Polytropes with known analytic solutions. Table 3 shows our numerical solutions compared to the analytic ones. The accuracy of the eigenvalues depends on the number of zones for a Polytrope. The more zones used, the closer numerical solutions to the eigenvalues are to the analytic ones. In this table we use about 1000 zones.

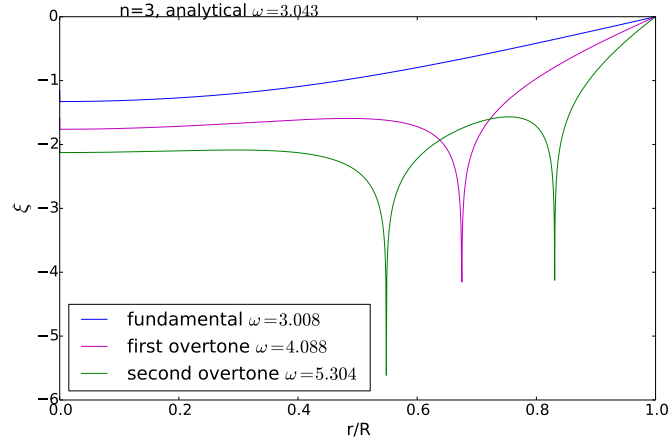


Figure 14 : The eigenmodes of Polytrope $n = 3.0$ with Hong's code. ($n = 3.5$, and $n = 4.0$ are commented out.)

Table 3 : Comparison of Analytic and Numerical Solutions to Fundamental Periods of Selected Stellar Models in GR.

Model	Γ_1	$\Pi_0/\Pi_0, \text{analytic}$
Polytrope $n = 3.0$	$5/3$	3.008/3.043
Polytrope $n = 3.5$	$5/3$	3.523/3.56

Chapter 4

Determining Hubble Constant With Gravitational-wave and Electromagnetic Observations

4.1 Introduction

One of the greatest discoveries in the 20th century is that the Universe is expanding as originally shown in Edwin Hubble's 1929 article "A relation between distance and radial velocity among extra-galactic nebulae". Hubble's law states that a galaxy's distance is proportional to its recessional velocity or redshift as shown in the Hubble diagram. The proportionality constant is named Hubble constant, H_0 . To measure H_0 we need two ingredients: one is the distance to a point and the other is the redshift of a freely falling body at that point.

Hubble originally measured a value of $H_0 = 500 \text{ km/s/Mpc}$. Later observations led to a range between 50 km/s/Mpc and 100 km/s/Mpc (Freedman 2017). There are mainly two methods to measure the Hubble constant with solely electromagnetic observations. The classical and local route to an accurate value of H_0 is through the calibration of Cepheids or the more luminous Type Ia supernovae providing distances extending well into the distant smooth Hubble flow, and the refinements among teams yield values of

$73.24 \pm 1.74 \text{ km/s/Mpc}$ (Riess et al. 2016). The measurements of the fluctuations in the cosmic microwave background (CMB) from the Big Bang provide a relatively new means of estimating the value of the Hubble constant. This very different approach leads to a derived value of $67.8 \pm 0.9 \text{ km/s/Mpc}$ (Planck Collaboration 2016), which is over $3 - \sigma$ discrepant with the most recent Riess et al. (2016) value. It is certainly worth noting that the local measurement of H_0 is based on the astrophysics of stars, and the CMB results are based on the physics of the early universe: the results are entirely independent of each other. However, the currently estimated error bars do not overlap (Bernal et al. 2016). How to explain the discrepancy? The obvious possibility is that one or both of the methods may suffer from unknown systematic errors. Another possibility is that there is underlying new physics (Bernal et al. 2016; Freedman 2017).

An independent and complementary way to measure Hubble constant makes use of both gravitational-wave and electromagnetic observations. Gravitational wave observations can directly provide distance information to merging binaries (Abbott 2017a). The association of a redshift via EM observations then allows determination of H_0 .

Measuring the Hubble constant with gravitational waves naturally fall into two categories. One is when the host galaxy or electromagnetic counterpart of a gravitational wave signal progenitor can be identified such that the redshift of the gravitational-wave event can be measured, and thus to estimate the Hubble constant using the directly measured distance from the gravitational-wave observation (Holz & Hughes 2005; Nissanke 2010, 2013; Chen et al. 2017). The multi-messenger observations allow us to use compact binaries as standard sirens, the gravitational-wave analog of an astronomical standard candle, to measure the Hubble constant. The measurement of H_0 combines the distance to the source inferred purely from the gravitational-wave signal with the recession velocity inferred from measurements of the redshift using electromagnetic data. This approach does not require any form of cosmic “distance ladder”, and the gravitational wave analysis can be used to estimate the luminosity distance out to cosmological scales directly, without the use of intermediate astronomical distance measurements. We call this method H_0 via counterpart. On 17 August, 2017, the Advanced LIGO and Virgo detectors observed

GW170817 (Abbott 2017a), a gravitational-wave signal from the merger of binary neutron stars. The detection was also made in electromagnetic waves. Less than 2 seconds after the merger, a gamma-ray burst (GRB 170817A) was detected within a region of the sky consistent with the LIGO-Virgo-derived location of the gravitational-wave source (Abbott 2017d; Goldstein 2017; Savchenko 2017). Subsequent observations by optical astronomy facilities made the identification of an optical transient signal within ≈ 10 arcsec of the galaxy NGC 4993, which is within the 90% LIGO-Virgo localization. That this optical transient is associated with GW170817 is supported by observations of the subsequent evaluation of the source (Abbott 2017e; Coulter 2017; Valenti 2017; Arcavi 2017) in addition to the results of searches of the LIGO-Virgo error box (Soares-Santos 2017). With this first detected BNS merger, the LVC were able to apply the H_0 via counterpart method (LIGO 2017) to determine the Hubble constant to be $70.0_{-8.0}^{+12.0} km/s/Mpc$. This is consistent with existing measurements, while being completely independent of them.

The other category is when we cannot identify the host galaxy because there is no associated electromagnetic signals observed in the same region where a gravitational wave happened. In the case of absence of a host galaxy, we use a galaxy catalog as the prior information (Schutz 1986; Del Pozzo 2012; Pozzo 2014; Chen et al. 2017) for where the gravitational wave could happen because we assume that the gravitational wave originated from a compact binary system located in a galaxy or the vicinity of a galaxy. We usually call this method H_0 statistical.

There are circumstances where we do not have electromagnetic counterpart observations for a gravitational wave. For example, the Sun could block the electromagnetic signals that accompanied a gravitational wave. Binary black hole mergers are not expected to give an electromagnetic signal. Some people suggested that in these cases, we simply not use these gravitational wave events. However, the fraction of gravitational waves that are associated with or can be observed with their electromagnetic counterparts is unknown to us. If the fraction is very small, we do not want to waste these events without their counterparts because we can still estimate Hubble constant even though much less accurately for an individual event without its counterpart. With enough events,

H_0 statistical may produce a better combined posterior estimate of H_0 than the H_0 via counterpart method does. Not only the gravitational waves without their counterparts but within about 0.1 redshift are helpful for H_0 statistical studies because we can use the publicly available galaxy catalog, but also the ones at higher redshift ($z > 0.1$) without their counterparts but well localized and have their corresponding galaxy catalogs from the followups of astronomers. For the latter, there are proposals of effort on the galaxy catalog for each gravitational wave event from private discussions with LSC members. Therefore, the H_0 statistical method is well worth studying.

In the remaining sections of this chapter, we summarize an approach to measuring the Hubble constant based on the original suggestion of Schutz (Schutz 1986) and along the lines investigated by Pozzo (2014). The method is summarized in Sec. 4.2. The application of the method to a mock-data-challenge undertaken by the LIGO-Virgo Cosmology group is summarized in Sec. 4.3. The chapter finishes with an application to GW170817 in which I reproduce the results from LIGO (2017).

4.2 Methodology

Let d represent the data from gravitational-wave observations and $h(\lambda, \alpha, \delta, z, H_0)$ represent a gravitational-wave signal from a compact binary merger. The parameters explicitly needed for this computation are right ascension α , declination δ , redshift z , and the Hubble constant H_0 . The masses, spins, and all other parameters except those explicitly needed for this calculation are represented by λ . The probability of d given that the signal is present is $p[d|h(\lambda, \alpha, \delta, z, H_0)]$; the probability of d in the absence of a signal is $p[d|0]$.

We further introduce the prior probability distribution $p(\alpha, \delta, z, H_0)$. Details of this distribution function will be discussed below in 4.2.3. For now, we note that catalogs of galaxies can be used to build distribution functions although care is needed to deal with incompleteness of those catalogs. On the other hand, electromagnetic observations that identify the host galaxy of the gravitational-wave source would give a very compact

distribution and provide a better measurement of the Hubble constant. The following formalism covers both cases at the same time provided one ignores the dependence of electro-magnetic follow-up on the original gravitational-wave observation. This latter issue will be the subject of future work.

4.2.1 Single observation

The posterior over H_0 given the observations d is

$$p(H_0|d) = \left(p[d|h] p_1 + p[d|0] p_0 \right)^{-1} \int \left\{ p[d|h(\lambda, \alpha, \delta, z, H_0)] p(\lambda) p(\alpha, \delta, z, H_0) p_1 \right\} d\alpha d\delta dz d\lambda \quad (4.2.1)$$

where

$$p[d|h] = \int \left\{ p[d|h(\lambda, \alpha, \delta, z, H_0)] p(\lambda) p(\alpha, \delta, z, H_0) \right\} d\alpha d\delta dz d\lambda dH_0 . \quad (4.2.2)$$

The prior $p(\alpha, \delta, z, H_0)$ is discussed in Sec. 4.2.3. We now introduce the likelihood

$$\mathcal{L}(\alpha, \delta, z, H_0|d) = \int \frac{p[d|h(\lambda, \alpha, \delta, z, H_0)] p(\lambda)}{p[d|0]} d\lambda \quad (4.2.3)$$

and define

$$\mathcal{E} = p[d|h]/p[d|0] . \quad (4.2.4)$$

At this point, we make the simplifying assumption that there is a signal present in the data with unknown parameters, i.e. $p_0 = 0$. The posterior on H_0 can now be written as

$$p(H_0|d) = \mathcal{E}^{-1} \int \mathcal{L}(\alpha, \delta, z, H_0|d) p(\alpha, \delta, z, H_0) d\alpha d\delta dz \quad (4.2.5)$$

It is useful to convert this expression into an expression that uses the gravitational-wave posterior which is usually computed using a uniform in spatial volume prior. Thus

$$p_{\text{gw}}(\alpha, \delta, r|d) d\alpha d\delta dr = \mathcal{L}(\alpha, \delta, r|d) V^{-1} \Theta(r) r^2 \cos(\delta) d\alpha d\delta dr \quad (4.2.6)$$

$$= \mathcal{L}(\alpha, \delta, cz/H_0|d) V^{-1} \Theta(cz/H_0) (c/H_0)^3 z^2 \cos(\delta) d\alpha d\delta dz \quad (4.2.7)$$

$$= p_{\text{gw}}(\alpha, \delta, z|d) d\alpha d\delta dz \quad (4.2.8)$$

which allows us to rewrite

$$\mathcal{L}(\alpha, \delta, cz/H_0|d) = \frac{(H_0/c)^3 V p_{\text{gw}}(\alpha, \delta, z|d)}{\Theta(cz/H_0) z^2 \cos(\delta)} . \quad (4.2.9)$$

Note that V is independent of H_0 within this approximation and is given by

$$V = 4\pi \int_0^\infty \Theta(r)r^2 dr \quad (4.2.10)$$

where $\Theta(r)$ is supposed to be the gravitational-wave searching efficiency but it is taken to be a step function instead because in practice, the parameter estimation studies are done using a large distance cut-off which is equivalent to using a step function for the efficiency. Substituting Eq. (4.2.9) into Eq. (4.2.5) gives

$$p(H_0|d) = \frac{H_0^3 V}{c^3 \mathcal{E}} \int p_{\text{gw}}(\alpha, \delta, z|d) \frac{p(\alpha, \delta, z, H_0)}{\Theta(cz/H_0)z^2 \cos(\delta)} d\alpha d\delta dz \quad (4.2.11)$$

4.2.2 Multiple observations

This generalizes to multiple observations as follows. Consider N binary mergers each occurring at different coalescence times $t_{c,j}$. The posterior over the Hubble constant then is

$$p(H_0|d) = \mathcal{E}^{-1} \prod_{j=1}^N \left\{ \int d\alpha d\delta dz \mathcal{L}_j(\alpha, \delta, z, H_0|d_j) p(\alpha, \delta, z, H_0) \right\} \quad (4.2.12)$$

where d_j is the data from each observation and $p[d|h]$ in Eq. (4.2.4) is replaced by

$$p[d|h] = \int \prod_j \left\{ \int d\alpha d\delta dz d\lambda p(\lambda) p_j[d_j|h(\lambda, \alpha, \delta, z, H_0)] p(\alpha, \delta, z, H_0) \right\} dH_0. \quad (4.2.13)$$

Equations (4.2.12), (4.2.13) and (4.2.4) determine the posterior on the Hubble constant. As we proceed to an actual measurement, the inclusion of nuisance parameters to address various systematic and statistical errors will be important.

4.2.3 Prior

The prior is taken to be

$$p(\alpha, \delta, z, H_0) = \epsilon(cz/H_0) p_g(\alpha, \delta, z, H_0) f(H_0) \quad (4.2.14)$$

where $\epsilon(cz/H_0)$ is the gravitational-wave search efficiency, $p_g(\alpha, \delta, z, H_0)$ is the spatial distribution of host locations, and $f(H_0)$ is given by

$$f(H_0) = \left[\int \epsilon(cz/H_0) p_g[\alpha, \delta, z, H_0] d\alpha d\delta dz \right]^{-1}. \quad (4.2.15)$$

to make the marginalized prior in H_0 the prior in H_0 or $p(H_0)$. The $p(H_0)$ can be any form, and in our studies we take it to be flat or $1/H_0$. The gravitational-wave search efficiency depends on the instrumental sensitivity and the analysis method used to identify signals, but not on the specific data used to make this measurement.

For multiple events, in order not to count the prior $p(H_0)$ multiple times we take the function $f(H_0)$ to be dependent on the number N of the total events. In this case, the prior is

$$p(\alpha_1, \dots, \alpha_N, \delta_1, \dots, \delta_N, z_1, \dots, z_N, H_0) = \prod_{j=1}^N \epsilon(cz_j/H_0) p_g(\alpha_j, \delta_j, z_j, H_0) f(H_0) \quad (4.2.16)$$

$$= [\epsilon(cz/H_0) p_g(\alpha, \delta, z, H_0) f(H_0)]^N \quad (4.2.17)$$

and the marginalized prior in H_0 is

$$f(H_0) = \frac{p(H_0)^{\frac{1}{N}}}{\int \epsilon(cz/H_0) p_g(\alpha, \delta, z, H_0) d\alpha d\delta dz} \quad (4.2.18)$$

where we recover Eqn. 4.2.15 for the single detection case when $N = 1$.

Now consider a galaxy catalog which provides the spatial location, size, luminosity, and other measures of mass for each galaxy. We model the contribution from each galaxy as a Gaussian

$$f_j(\alpha, \delta, z, H_0) = \frac{1}{\sqrt{(2\pi)^3} \sigma_{\alpha_j} \sigma_{\delta_j} \sigma_{z_j}} \exp \left[-\frac{1}{2} \left\{ \frac{(\alpha - \alpha_j)^2}{\sigma_{\alpha_j}^2} + \frac{(\delta - \delta_j)^2}{\sigma_{\delta_j}^2} + \frac{(z - z_j)^2}{\sigma_{z_j}^2} \right\} \right] \quad (4.2.19)$$

weighted by its blue luminosity. An alternative is to model the galaxies as delta-functions similarly weighted. Both approaches should yield equivalent results once systematic effects are properly dealt with. The former more easily includes information about the size and shape of the galaxies, but it has weaknesses for sparsely sampled posteriors.

In addition to these contributions, it is extremely important to account for those galaxies that we have not yet identified. We do this by introducing a completion function so that the blue luminosity (or other galaxy mass weight) is

$$p_g(\alpha, \delta, z, H_0) = \hat{L}^{-1} \left[\sum_j L_{j,70} f_j(\alpha, \delta, z, H_0) + L_* \mathcal{F}(z) \cos(\delta) \right]. \quad (4.2.20)$$

Under the assumption that the redshift of each galaxy is directly measured, this function does not depend on H_0 . In reality, there will be some dependence on H_0 introduced for nearby galaxies and/or galaxies not sufficiently far away to be fully in the Hubble flow. Over large scales, this distribution function in Eqn. 4.2.20 should be constant per unit co-moving volume. In the local Universe, this is approximately equivalent to the integral over right ascension and declination being proportional to z^2 .

The efficiency function $\epsilon(z, H_0)$ is ultimately determined using injections into the gravitational-wave data and searching for them. Some important intuition can be obtained by introducing a cut-off at luminosity distance r_H and defining

$$\epsilon(cz/H_0) = \Theta(r_H H_0/c - z) . \quad (4.2.21)$$

The final result should be relatively insensitive to the particular form of this function provided it introduces a cutoff in luminosity distance to which the search is sensitive. This should be checked.

4.3 Mock Data Challenge

This section reports work carried out in collaboration with the LIGO-Virgo Cosmology group and will be part of a paper which is in preparation by that group. The mock galaxy catalogs used here were generated by collaborators in the University of Glasgow.

4.3.1 Simulation

To measure the Hubble constant with the approach described above, we used the second observing scenario studies from the first-two years (F2Y's) study (Singer 2014). The paper focuses on two observing scenarios representing the evolving configuration and capability of the Advanced GW detector array. The first, in 2015, is envisioned as a three-month science run. LIGO Hanford and LIGO Livingston Observatories are operating with an averaged $(1.4, 1.4)M_\odot$ BNS range between 40 and 80 Mpc . The second, in 2016-2017, is a six-month run with H and L operating between 80 and 120 Mpc and the addition of Advanced Virgo with a range between 20 and 60 Mpc . For each of the two scenarios

synthetic detector streams were made by placing post-Newtonian inspiral signals into two months of colored Gaussian noise. There was an average waiting time of ≈ 100 sec between coalescences. At any given time, one BNS inspiral signal was entering LIGO's sensitive band while another binary was merging, but both signals were cleanly separated due to their extreme narrowness in time-frequency space. The power spectral density (PSD) estimation used enough averaging that it was unaffected by the overlapping signals. Component masses were distributed uniformly between 1.2 and $1.6 M_{\odot}$. Each NS was given a randomly oriented spin with a maximum magnitude of $\chi = c|S|/Gm^2 \leq 0.05$, where S is the star's spin angular momentum and m is its mass.

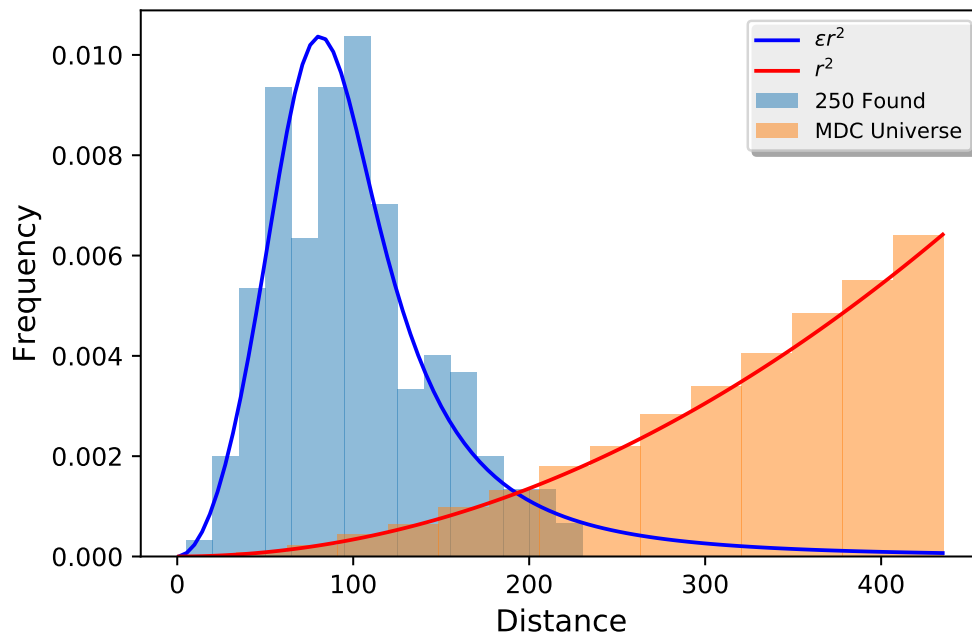


Figure 15 : The normalized histogram of the distances of the found injections (blue) and test galaxy catalog (orange) from the 2016 MDC simulation set. The blue line is uses the gravitational-wave detection efficiency $\epsilon(r)$ while the red line is just a simple r^2 curve.

4.3.2 Found injections

The F2Y's MDC made 100,000 of injections and found about 1000 events for the two scenarios. In our study, the MDC uses only the 2016-2017 observing scenario, which

includes 250 found injections that have gone through parameter estimation using LALInference. The distance distribution of the found injections is in Fig. 15. Also plotted is the distribution of the galaxy catalog for the MDC, which is introduced in the last section. We can see that the galaxy distance distributes as a function of distance squared, the found injections peak at around 100 Mpc. This is mainly because the 2016-2017 scenario operates between 80 to 120 Mpc and it is proportional to the distance squared multiplied by the detection efficiency ϵ as shown by the blue solid line in the figure.

We also show in Fig. 16 the function $f(H_0)$ that produces a flat prior in H_0 is comparable with a cubic scaling of H_0 which is as expected for a smooth, uniform distribution in volume as is the case for the MDC galaxy catalog, which will be introduced in the next subsection.

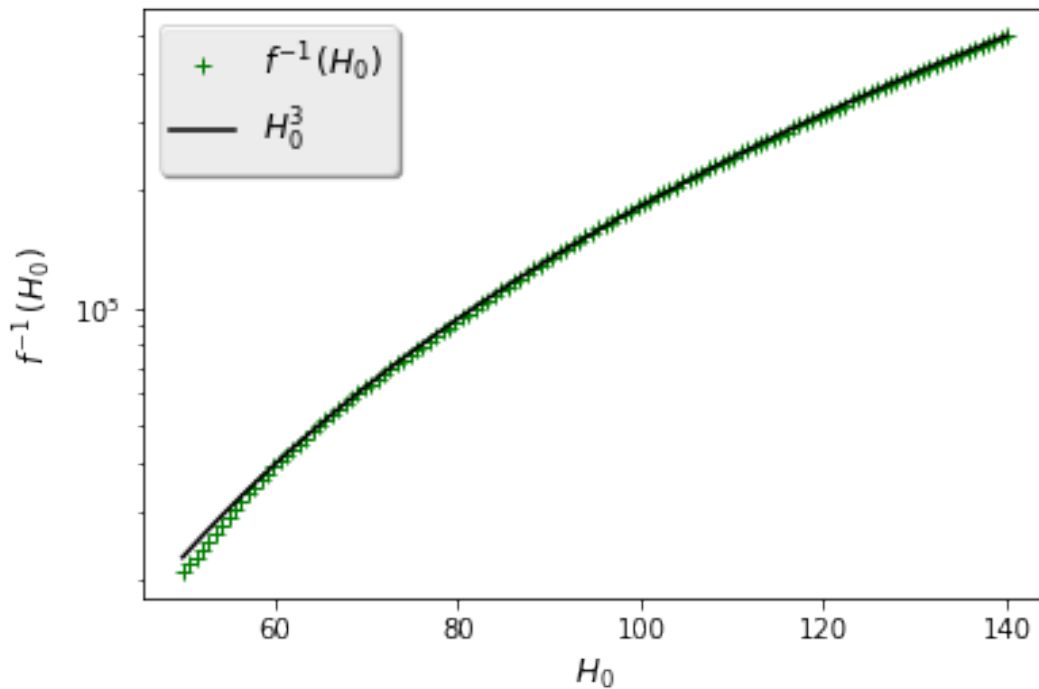


Figure 16 : For the galaxy catalog in the MDC v1, the function $f(H_0)$ determined to produce a uniform prior $p_H(H_0)$ compared with a power-law in H_0 . The cubic scaling is expected for a smooth, uniform in volume distribution at large luminosity distance.

4.3.3 Galaxy catalogs

The full galaxy catalog of the MDC in our studies, which is called MDC v1, contains 48,906 galaxies. Each has its right ascension (RA), declination (Dec), and redshift z . The RA's and the Dec's are uniformly distributed in the whole sky. The redshifts of the galaxies range from close to 0 to 0.1011 and their distribution is proportional to z^2 . The cosmology used for making the injections of GW sources corresponds to $H_0 = 70 \text{ km/s/Mpc}$.

We also construct incomplete galaxy catalogs from the complete one. First the model universe from MDC v1 is extended such that when the apparent magnitude cut is applied, the redshift distribution of the limited catalogue trails to zero without a hard cut off. The redshift goes up to 0.45 in this extended catalog. Luminosities are then assigned randomly to galaxies within the universe, from a Schechter function parametrised by $\alpha = -1.07$, and a lower limit of $L = 0.001L_*$, where $L_* = 1.2 * 10^{10} h^{-2} L$. and $h = 0.7$.

Three galaxy catalogs are then truncated from the extended version of MDC v1 by applying apparent magnitude cuts. They are named MDC v2.1, v2.2, and v2.3 and have different levels of completeness that correspond to approximately 25, 50, and 75% of the 250 GW detections with hosts contained in the catalogs.

4.3.4 Combined H_0 posterior

We apply the method discussed in Sec. 4.2 to the 250 events using various galaxy catalogs. We first show the proof of principle calculations with an empty galaxy catalog. Without any information of the galaxies, the posterior of H_0 from each event is expected to be the same as the prior in H_0 . In the case we choose a flat prior, we expect to obtain a flat posterior from each event. The combined posterior with 250 events are also expected to be flat. These are illustrated in Fig. 17, which also proves the validation of our code.

We then calculate the posteriors from the events using the complete galaxy catalog MDC v1. Fig. 18 shows the combined posteriors of the Hubble constant as events are added to the combination. The thicker the lines the more events are added. Combining all the 250 events, the peak value of H_0 is about 69.5 km/s/Mpc and the $1 - \sigma$ error of

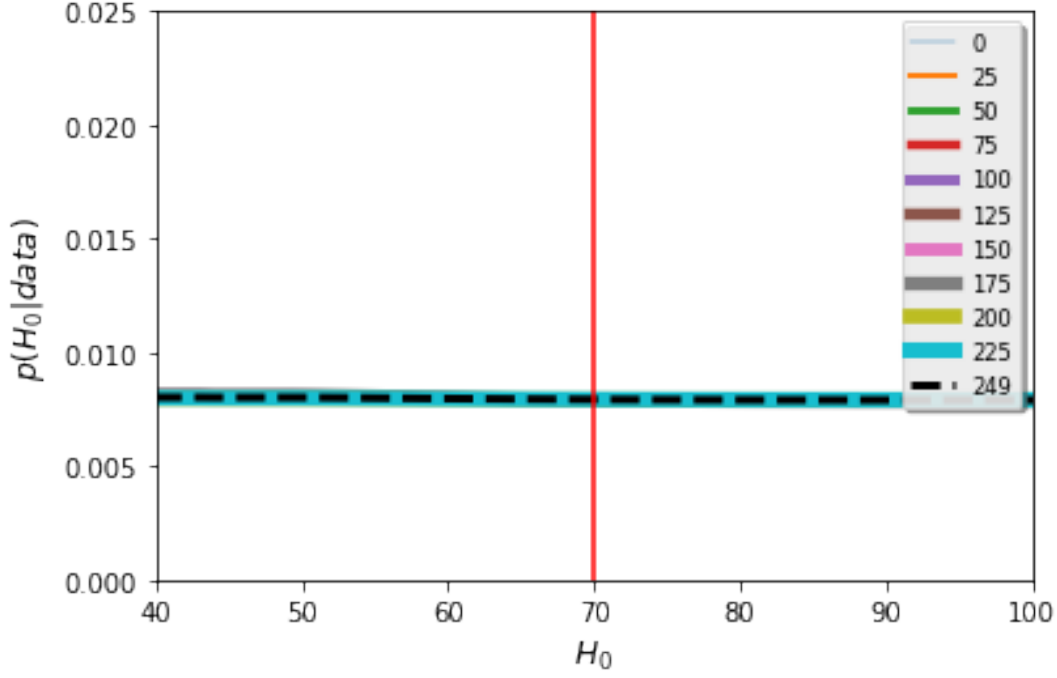


Figure 17 : The posterior distribution of H_0 using the KDE method for the 250 coming from the MDC simulation with an empty galaxy catalog.

H_0 , i.e., σ_{H_0} , is 1.5 km/s/Mpc or an accuracy about 2%.

We make a plot of the peak value of H_0 and its $1 - \sigma$ error bar as a function of the number of (i.e., the first N) GW events in Fig. 19. The ordering of the number follows that the events are always grouped in the order that they are designated, MDC 1 through MDC N . We can see that the more GW events we use, the closer the peak value to the “real” value and the smaller the $1 - \sigma$ error bar.

We also expect the $1 - \sigma$ error in H_0 to be inversely proportional to the square root of the number of events,

$$\sigma_{H_0} = C_\sigma / \sqrt{N} \quad (4.3.1)$$

where C_σ is a proportional constant. To check this, we group the events and use them. For each number N of events, we have $250/N$ groups of N events. For each group, we combine their posteriors and get a combined posterior. We then take the $1 - \sigma$ error bar of the combined posterior for a group of events. We repeat this for other groups of N events. In the end, we get an average value of σ_{H_0} and its standard deviation for the groups of N events. We take several values of N , for example 10, 20, 30, 40, 50, 60, etc,

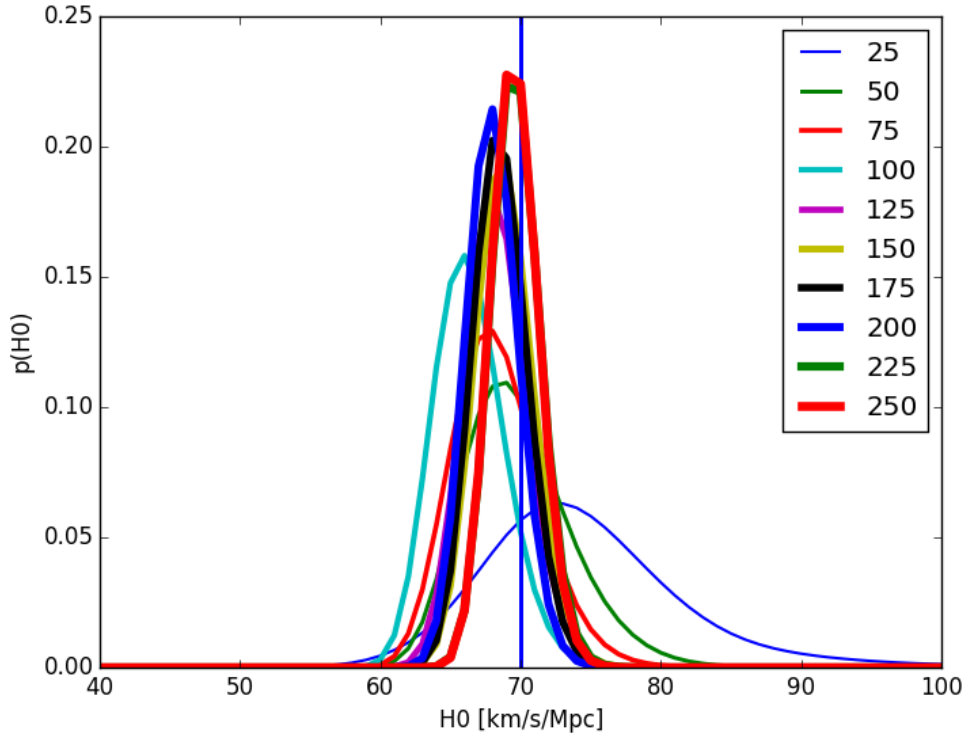


Figure 18 : The posterior distribution of H_0 using the KDE method for the 250 coming from the MDC simulation. The angular selection uses all galaxies having a posterior sample within $80 \text{ kpc}/r$ of the galaxy center. The catalog used to determine the spatial distribution of signals is also used in the recovery step. The red vertical line corresponds to the peak value. The light lines are the posteriors as each event is added.

and repeat the process. The averaged σ_{H_0} and the standard deviation of σ_{H_0} as a function of N are shown in the cyan dots and black bars in Fig. 20. The thin black dashed line shows the best fit, with the proportional constant $C_\sigma = 25.57 \text{ km/s/Mpc}$.

Further, we study the effects of incompleteness of a galaxy catalog on the H_0 measurement. Figs. 4.3.4, 4.3.4, and 4.3.4 show the posteriors calculated from the 250 events using 75%, 50%, 25% complete catalogs. With the 75% complete catalog MDC v2.3 and using the 250 events, we get the peak value of H_0 , as shown by the thick red solid line, close to the injected value and the $1 - \sigma$ error being slightly larger than with the full catalog MDC v1. The results in 50% complete catalog MDC v2.1 case are similar to the 75% complete case with only further larger $1 - \sigma$ error in H_0 . For the 25% case, the peak value of the combined posterior from the 250 event is about 68 km/s/Mpc and $1 - \sigma \text{ error}$

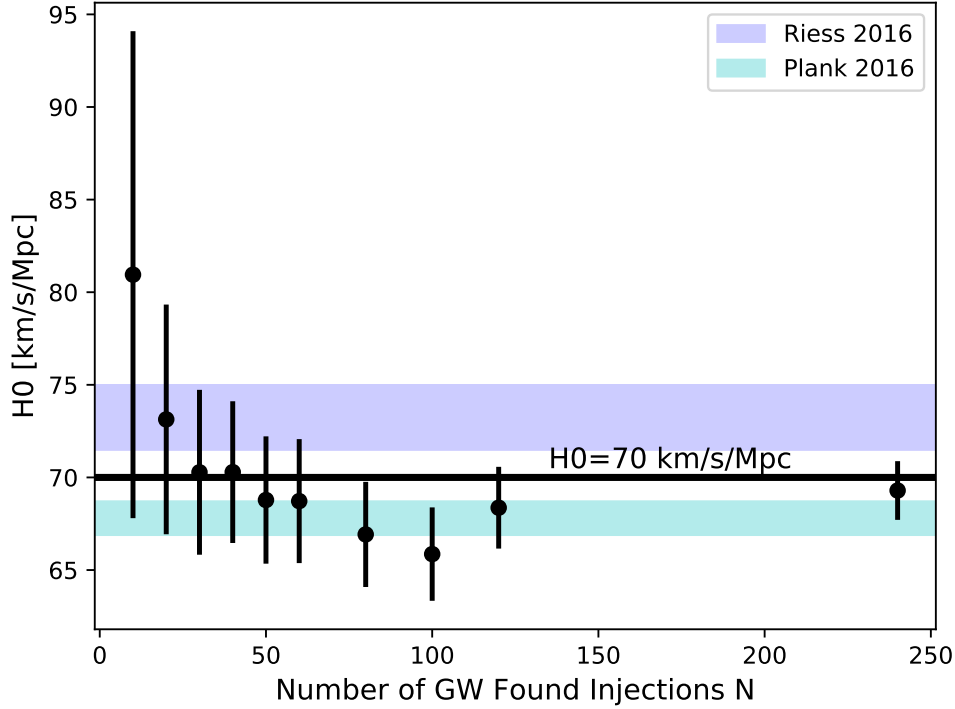


Figure 19 : The peak values and one-sigma errors of Hubble constant as a function of the number of GW events in MDC simulations starting from MDC 1 and moving up in number to MDC 250 using the KDE method. The “real value” or the injected value for the simulations is 70km/s/Mpc . The colored bars show the one-sigma errors of H_0 measured by other teams, where the blue and the cyan colors correspond to results in Riess et al. (2016), and Planck Collaboration (2016), respectively.

is 4.6 km/s/Mpc , which triples the σ_{H_0} in the case with MDC v1. Note that the number of the events are ordered as in the F2Y’s MDC which have more events injected in closer galaxies in the first half of the events than the second half.

4.4 Results with electromagnetic counterparts for GW170817

Now we move to the application of the counterpart method to GW170817, which is the only observed BNS merger with its host so far. While we focus on using the statistical association between galaxies and gravitational-wave observations to estimate the Hubble constant. The methodology is easily adapted to the situation where electromagnetic observations either identify a counterpart or constrain the source to not be in a particular galaxy set. In this approach, the spatial distribution function $p_g(\alpha, \delta, z, H_0)$ is modified

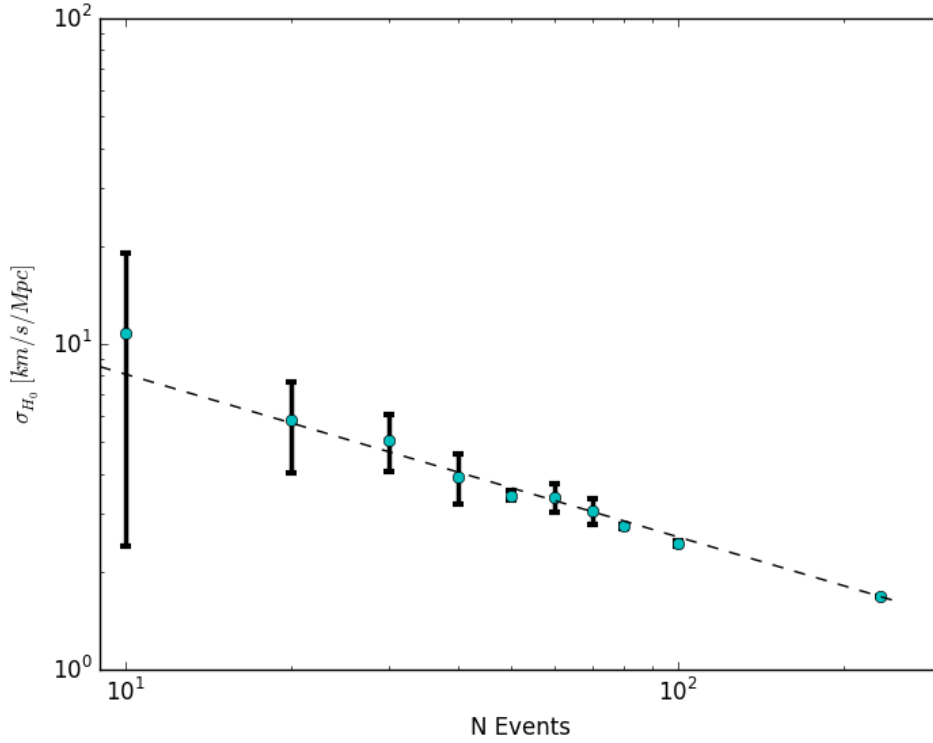


Figure 20 : The log-log plot of the one-sigma error of Hubble constant and its standard deviation (error bars) as a function of the number of GW events in MDC simulations using the KDE method.

on an event-by-event basis as a result of the electromagnetic follow-up observations. For example, the confident identification of the counterpart in NGC4993 for GW170817 immediately introduces a likelihood function that selects only this galaxy when constructing the prior.

Applying counterpart formalism to GW170817 using recession velocity 3017 ± 166 km/s for the single galaxy NGC4993 gives the result shown in Fig. 22 and $70.8^{+11.5}_{-7.7}$ km/s/Mpc. This is consistent with LIGO's other pipelines that calculate the H_0 value (LIGO 2017).

4.5 H_0 statistical results for GW170817

In this section instead of using the observed host galaxy of GW170817 we use a galaxy catalog as the prior information for the location of the GW170817. A number of galaxy

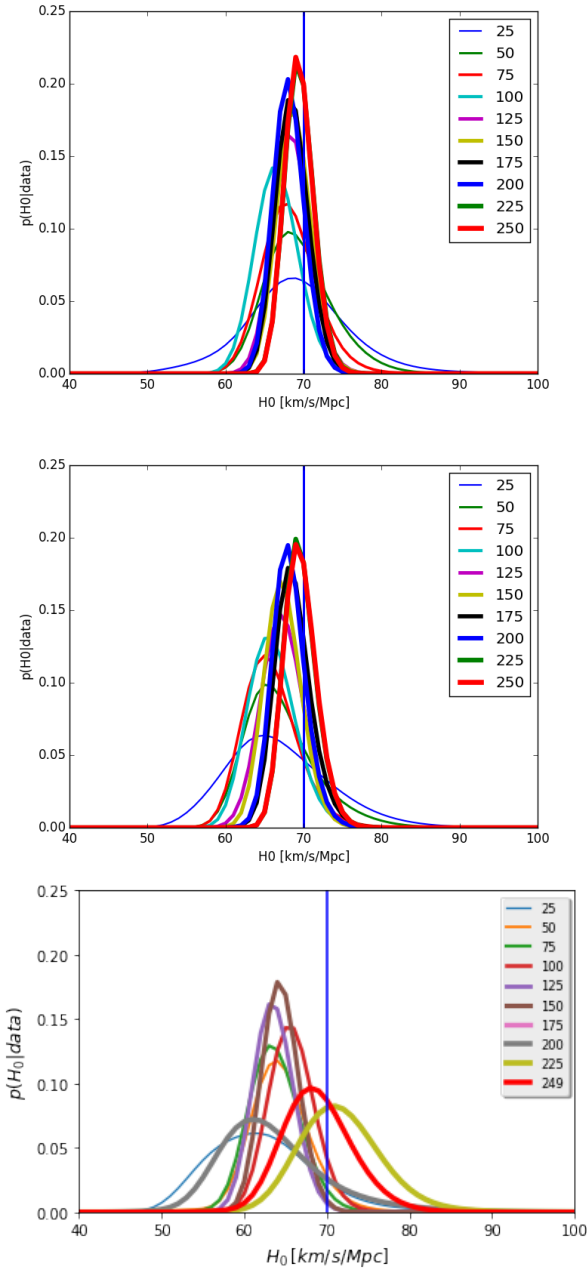


Figure 21 : The posterior distributions of H_0 using the KDE method for the 250 coming from the F2Y's MDC simulation with the 75%, 50%, 25% complete galaxy catalogs.

catalogs are available Kopparapu et al. (2008); White et al. (2011); Dalya et al. (2016) with their incompleteness being at different levels and they can be exploited to construct the known matter distribution. However, each of these has their limitations. The original gravitational-wave catalog developed by Kopparapu et al. (2008) only includes

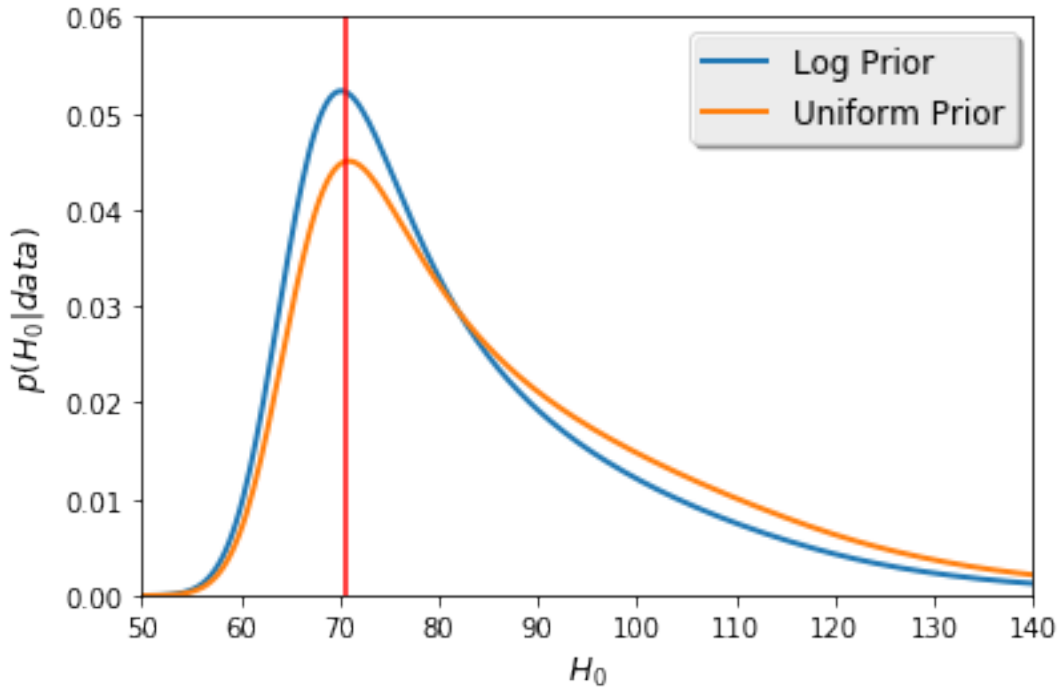


Figure 22 : The posterior over H_0 using the information from the identification of the electromagnetic counterpart. The gravitational-wave samples were generated using the fixed position of the counterpart in NGC4993.

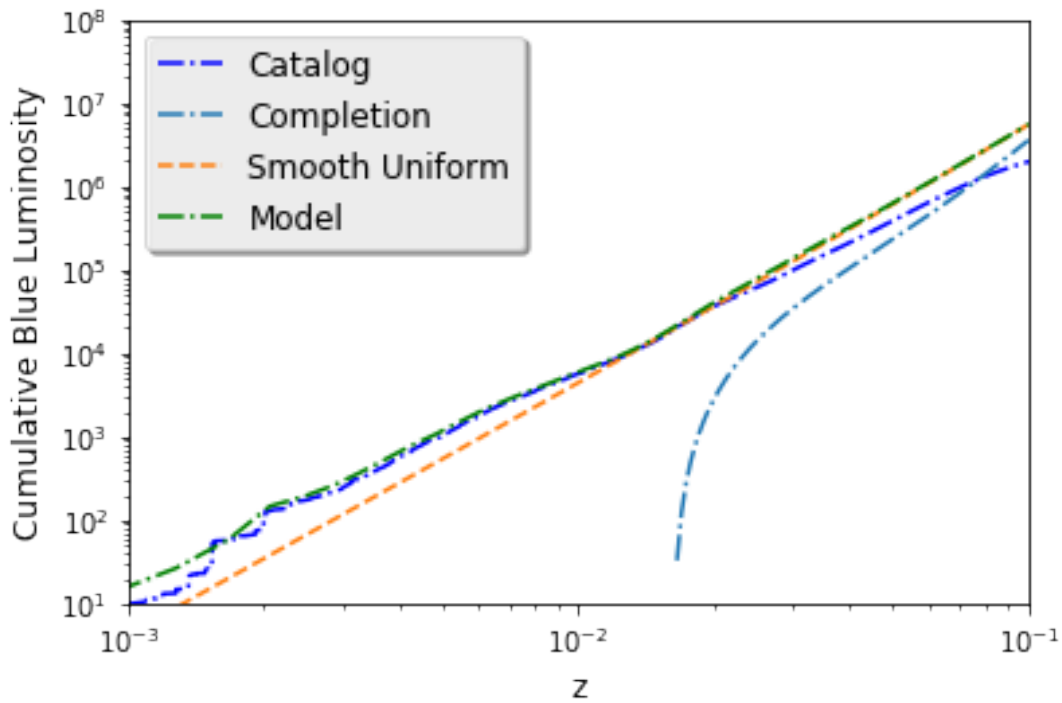


Figure 23 : Cumulative blue luminosity as a function of redshift.

information up to 2007; the GWGC of White et al. (2011) has more recent information, but more information is available now. In this study, we have used version 2 of the GLADE catalog Dalya et al. (2016) which is estimated to be complete to about 73 Mpc. The unnormalized and angle-integrated distribution $\int_0^z dz' \int d\alpha d\delta L_B(\alpha, \delta, z', H_0)$ for $H_0 = 70\text{km/s/Mpc}$ is shown in Fig. 23.

This is equivalent to the cumulative blue luminosity as a function of redshift which is also shown for the GLADE catalog. The uniform density fit from Kopparapu et al. (2008) is also shown. The function \mathcal{F} is approximated by a second-order polynomial in z . As shown in Fig. 23, this approach does a reasonably good job of addressing the lack of completeness.

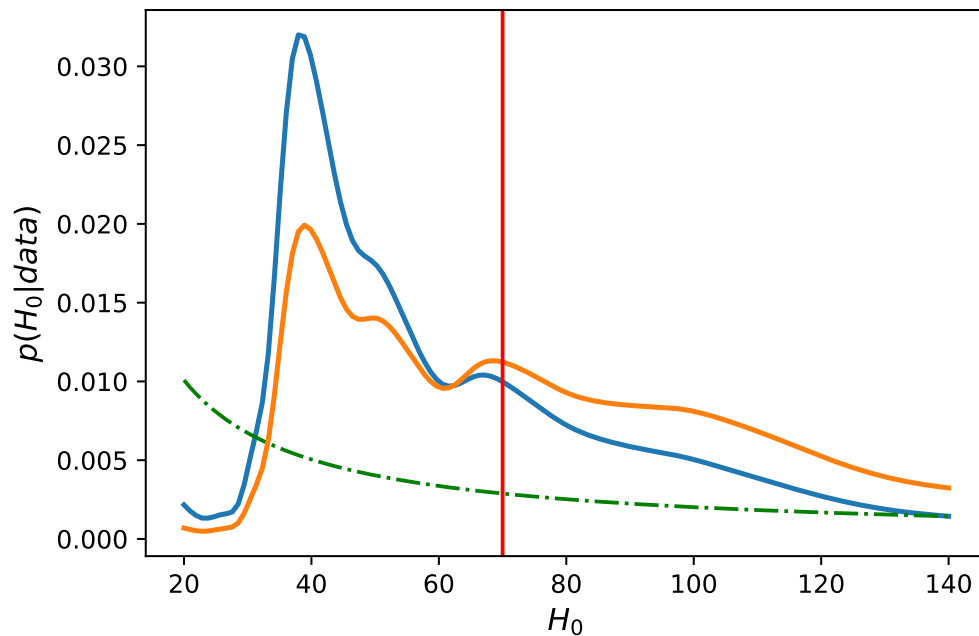


Figure 24 : The posterior over H_0 using Glade v2.2. The gravitational-wave samples, generated using standard uniform in volume priors, were used to build a KDE of the posterior distribution from the gravitational-wave data and the galaxies were approximated as delta functions.

Using the galaxy catalog (v2.2 of Glade) and the simplified efficiency given in Eq.(4.2.21) with $r_H = 100$ Mpc, the statistical result is shown in Fig. 24. We can see that with the statistical method, there are several bumps in the posterior of Hubble constant. These peaks result from the non-uniform distribution of the galaxies. One of

the bumps, as indicated by the vertical red line in Fig. 24, falls around the measured peak value from the $H_0 +$ counterpart method with the GW170817 event and its host galaxy NGC4993. Even though the mostly likely peak value is not the same as that from the counterpart method, we should know that this is as expected from the distribution of the matter in the catalog. With multiple events, we should be able to combine the posteriors from individual events and get the correct peak value. The related studies are demonstrated in Sec. 4.3 with the MDCs.

Chapter 5

Conclusions

5.1 Summary

The first direct detection of gravitational waves (GWs) on Sep 14, 2015 by advanced Laser Interferometer Gravitational-wave Observatories (LIGO) opened a new era of astronomy. Within and outside of the LIGO-Virgo Scientific Collaboration I studied several aspects of the gravitational wave astronomy and tested the theories of general relativity and modified gravity. Before and during aLIGO's first observing run, I investigated the constraints that can be placed on the astrophysics of the Galactic Center super massive black hole as well as strategies for future observations. I also studied the chameleon field theory using the pulsations of Cepheid variable stars in dwarf galaxies. During the first observing run, I worked on the gravitational wave searching pipeline GstLAL, analyzed two chunks of real data to search offline for gravitational waves, and found a lower-significance trigger LVT151012. During the second observing run and after we detected the first binary neutron star (BNS) merger and its EM counterpart NGC4993, I applied my tools on the event and constrained H_0 with and without its EM counterpart. I have also been collaborating within the LSC Cosmology group to further study the statistical method of measuring H_0 using the data from a Mock Data Challenge (MDC).

Using the Galactic Center stellar orbits, we use Markov Chain Monte Carlo (MCMC) method as well as the analytic model (Fisher matrix) we developed to understand what

correlations are well-constrained and why. We conclude that existing astrometric measurements cannot constrain the spin of the Galactic Center black hole. Extrapolating to the precision and cadence of future experiments, we anticipate that the black hole spin can be measured, extending previously-observed stellar orbits. Our calculations show that we can measure the black hole spin to a precision of 0.3 at 90% confidence with daily orbital observations of star S2 for 16 years using telescopes that have an angular resolution of $10 \mu\text{as}$ and a radial velocity resolution of 500 m/s . If in addition future measurements include discovery of a new, tighter stellar orbit, then future data could conceivably enable tests of strong field gravity, by directly measuring the black hole quadrupole moment. Our simulations show that with a star similar to S2 but half the distance to the Galactic Center and a telescope of resolutions stated above, we can start to test the no hair theorem with weekly orbital observations of 300 weeks or 6 years.

We also demonstrate the testing of chameleon field theory on stellar structure scales with the distance indicator Cepheid variable stars. Using the numerical results obtained for the evolutions of stars from MESA, we calculate the pulsation rates of Cepheid variable stars with both the theory of GR and the chameleon field theory. We compare our results with JVS ansartz, and show that the effects of chameleons on the changes of Cepheids periods from our numerical calculations are several times larger than those from their ansartz. We also calculate the effects of scalar fields on the ratios of pulsation modes and show that colder and more massive Cepheid stars are more favorable for testing chameleon fields. Very importantly, our study find that metallicity has a comparable effect on the pulsations of Cepheids than chameleon scalar fields. Therefore, it should be carefully taken into account of in the future efforts of constraining the chameleon filed theory. We also point out the obstacles we are facing. One is the lack of observational data that requires the overtone Cepheids to be located in extragalactic galaxies. The second is that it is difficult to constrain the metallicity of a galaxy very accurately, especially in extragalactic galaxies. The error of metallicity is typically 100% or larger which affect the pulsation rates to the same extent as the chameleon field parameters do.

I run end-to-end simulation with the O1data from LIGO's first observing run to build

method and tools to of measuring the Hubble constant with both GW events and galaxy catalogs in the case that the EM counterpart of a GW is not identified. Using the method and tools, we apply to the first detected BNS event GW170817 with and without its host galaxy NGC4993. We estimate that the Hubble constant is $H_0 = 70.8^{+11.5}_{-7.7} \text{ km/s/Mpc}$ given the redshift of the host. Pretending we do not know the host galaxy and use a galaxy catalog GLADE as the prior information of the possible position of the BNS event, we estimate the Hubble constant to be likely to take several values because several bumps show in the posterior, among those bumps there is one sits around the “real” value. We also apply the method to the found injections in the 2016-2017 scenario of the first two years’ MDC and estimate how well we can measure the Hubble constant with multiple events. We find that with 250 events, we can constrain H_0 to an accuracy of 1.5 km/s or 2%. This method can be applied to future telescopes as well.

5.2 Future Work

To extrapolate the work presented in this thesis, several efforts have been ongoing or can be made in the future as planed.

The Hubble constant measurement with the Mock Data Challenge can be further studied in the following aspects:

- The effects of incompleteness of galaxy catalog on the H_0 determination. The galaxy catalog we observe in real world is usually not complete to the distance at which we need to study H_0 . The studies and results we obtain from the MDC simulation with galaxy catalog with various incompleteness can indicate how the value of H_0 could be affected in reality.
- The effects of the value of the fraction of the gravitational waves detected with their EM counterparts on the H_0 measurement. Due to various mechanisms such as the Sun can block a fraction of EM counterparts of the gravitational waves to be detected, it is worth studying the how the fractional value can affect our measurement when we combine the methods with and without the EM counterparts.

Furthermore, to continue and extrapolate my end-to-end simulation on the Hubble constant measurement to future observations, it is well worth making use of the scenario studies planned before O3 observing run, which is scheduled later this year. The scenario study can be used as an end-to-end simulation of H_0 determination using galaxy catalogs in mimicked O3 observation scenarios. Several factors can have effects on and should be accounted for.

- The mimicked Universe was constructed by completion of an observed galaxy catalog using Schechter luminosity function, and the added galaxies are assumed to be uniform in 3D volume. However, this assumption does not take into account of large scale structures, of which the most commonly used quantitative measure is the galaxy two-point correlation function, which traces the amplitude of galaxy clustering as a function of scale.
- The GW sources were injected in the centers of the galaxies. In fact, some of them can happen off the galaxies due to the mechanism called neutron star kicks.
- The modeled rate of BNS mergers were proportional to the blue luminosity of a galaxy because most of previous research used similar approaches. This assumption is not accurate because the first BNS event was detected in an elliptical galaxy whose blue luminosity was small which would indicate a small possibility of detection. The above factors are the main ones that I want to study to see how Hubble constant constraint can be affected with end-to-end simulation of BNS mergers. Besides, the methodology can also be applied to binary black hole (BBH) and neutron star black hole (NSBH) events, and can be extended to the work on constraining other cosmological parameters.
- There is a 1% calibration error in the gravitational wave strain, which leads to a 1% error in the distance measurement of the GW and effect the gravitational wave. This should be studied carefully.
- Another factor that can affect the distance measurement is gravitational lensing.

This can fold into parameter estimation and result an error in H_0 .

- The scenario study can be used to constrain other cosmological constants such as Ω_m when the GW event happens at redshift higher than, say, 0.1. In this sense, the method can be extrapolated to the next generation telescopes such as Einstein telescope.
- The simulation can be used to study the value of redshift at which we can no longer assume a Euclidean universe by comparing the posteriors of H_0 using Euclidean and non-Euclidean universes and see when the turnover happens.

To summarize, we can see that along with the Hubble constant efforts, many interesting cosmology questions can be asked, studied and maybe answered within the next decade.

Bibliography

Abbott, B. P. *et al.*. 2016a, PRL, 116, 061102

—. 2016b, PRL, 116, 241103

—. 2017a, PRL, 118, 221101

—. 2017b, ApJL, 851

—. 2017c, PRL, 119, 141101

Abbott, B. P. *et al.* 2017d, ApJ, 848

Abbott, B. P. *et al.*. 2017e, ApJ, 848

—. 2017a, PRL, 119, doi:10.1103/PhysRevLett.119.161101

Alexander, T., & Hopman, C. 2009, ApJ, 697, 1861

Alexander, T., & Pfuhl, O. 2014, ApJ, 780, 148

Apostolatos, T. A., Cutler, C., Sussman, G. J., & Thorne, K. S. 1994, PRD, 49, 6274

Arcavi, I. *et al.*. 2017, Nature

Bartos, I., Haiman, Z., Kocsis, B., & Márka, S. 2013, Physical Review Letters, 110, 221102

Bernal, J. L., Verde, L., & Riess, A. G. 2016, Journal of Cosmology and Astroparticle Physics, 2016

- Blanchet, L. 2013, (arXiv:1310.1528)
- Broderick, A. E., Loeb, A., & Reid, M. J. 2011, ApJ, 735, 57
- Buonanno, A., Chen, Y., & Damour, T. 2006, PRD, 74, 104005
- Chang, P., & Hui, L. 2011, ApJ, 732, 25
- Chen, H.-Y., Fishbach, M., & Holz, D. E. 2017, arXiv:1712.06531
- Coulter, D. A. *et al.*. 2017
- Cox, J. P. 1980, The Theory of Stellar Pulsation (Princeton University Press)
- Creighton, J. D., & Anderson, W. G. 2011, Gravitational-Wave Physics and Astronomy: An Introduction to Theory, Experiment and Data Analysis (Wiley-VCH)
- Dalya, G., Frei, Z., Galgoczi, G., Raffai, P., & de Souza, R. S. 2016, <http://aquarius.elte.hu/glade>
- Del Pozzo, W. 2012, PRD, 86, 043011
- Falcke, H., Melia, F., & Agol, E. 2000, ApJL, 528, L13
- Freedman, W. L. 2017, Nature Astronomy, 1, 0169
- Freitag, M., Amaro-Seoane, P., & Kalogera, V. 2006, ApJ, 649, 91
- Genzel, R., Eisenhauer, F., & Gillessen, S. 2010, Reviews of Modern Physics, 82, 3121
- Ghez, A. M., Salim, S., Weinberg, N. N., et al. 2008, ApJ, 689, 1044
- Gillessen, S., Eisenhauer, F., Trippe, S., et al. 2009, ApJ, 692, 1075
- Goldstein, A. *et al.*. 2017, ApJ, 848
- GRAVITY Collaboration. 2017, Astronomy & Astrophysics, 602, arXiv:0711.1677
- Han, W.-B. 2014, Research in Astronomy and Astronphysics, 14, arXiv:1404.5160

- Hartle, J. B. 2003, Gravity: An Introduction to Einsteins General Relativity (ISBN-13:978-0805386622)
- Holz, D. E., & Hughes, S. A. 2005, ApJ, 629, 15
- Hui, L., Nicolis, A., & Stubbs, C. 2009, PRD, 80, 104002
- Hulse, R. A., & Taylor, J. H. 1975, ApJL, 195, L51
- Iorio, L. 2011, PRD, 84, 124001
- Jain, B., Vikram, V., & Sakstein, J. 2012, arXiv:1204.6044
- Khoury, J. 2013, arXiv:1204.6044
- Kopparapu, R. K., Hanna, C., Kalogera, V., et al. 2008, ApJ, 675, 2
- LIGO, *et al.*. 2017, Nature, 551, 85
- Liu, K., Wex, N., Kramer, M., Cordes, J. M., & Lazio, T. J. W. 2012, ApJ, 747, 1
- Merritt, D. 2010, ApJ, 718, 739
- . 2013, Dynamics and Evolution of Galactic Nuclei (Princeton University Press)
- Merritt, D., Alexander, T., Mikkola, S., & Will, C. M. 2010, PRD, 81, 062002
- Nissanke, S. *et al.*. 2010, ApJ, 725
- . 2013, arXiv:1307.2638
- Paxton, B., Bildsten, L., Dotter, A., et al. 2010, Astrophys.J.Suppl, 192, 3
- Planck Collaboration. 2016, Astronomy & Astronphysics, 594, A13
- Pozzo, W. D. 2014, J. Phys. Conf. Ser., 484, 012030
- Preto, M., & Amaro-Seoane, P. 2010, ApJL, 708, L42
- Psaltis, D., & Johannsen, T. 2011, Journal of Physics Conference Series, 283, 012030

- Rea, N., Esposito, P., Pons, J. A., et al. 2013a, arXiv:1307.6331
- . 2013b, ApJL, 775, L34
- Riess, A. G., Macri, L. M., Hoffmann, S. L., & et al. 2016, ApJ, 826, 56
- Sadeghian, L., & Will, C. M. 2011, Classical and Quantum Gravity, 28, 225029
- Sakstein, J. 2013, arXiv:1309.0495
- Savchenko, V. *et al.*. 2017, ApJ, 848
- Schutz, B. F. 1986, Nature, 323, 310
- Singer, L. *et al.*. 2014, ApJ, 795, 105
- Soares-Santos, M. *et al.*. 2017, ApJL, arXiv:1710.05459
- The LIGO Scientific Collaboration. 2015, Class. Quantum Gravity, 32, 074001
- Tichy, W., & Flanagan, E. 2011, Phys. Rev. D, 84, arXiv:1101.0588
- Townsend, R. H. D., & Teitler, S. 2013, MNRAS
- Valenti, S. *et al.*. 2017, ApJ, 848
- Wald, R. 1984, General Relativity (University of Chicago Press)
- Weinberg, N. N., Milosavljević, M., & Ghez, A. M. 2005, ApJ, 622, 878
- Wex, N., Liu, K., Eatough, R. P., et al. 2013, in IAU Symposium, Vol. 291, IAU Symposium, 171–176
- Wharton, R. S., Chatterjee, S., Cordes, J. M., Deneva, J. S., & Lazio, T. J. W. 2012, ApJ, 753, 108
- White, D. J., Daw, E. J., & Dhillon, V. S. 2011, Classical and Quantum Gravity, 28, 8
- Will, C. 1985, Theory and Experiment in Gravitational Physics (Cambridge University Press)

Will, C. M. 2005, Living Rev. Rel., 9, 3

—. 2008, ApJL, 674, L25

Will, C. M., & Maitra, M. 2017, PRD, 95, 1

Zhang, F., Lu, Y., & Yu, Q. 2015, ApJ, 809, 127

Zucker, S., & Alexander, T. 2007, ApJL, 654, L83

Zucker, S., Alexander, T., Gillessen, S., Eisenhauer, F., & Genzel, R. 2006, ApJL, 639, L21

CURRICULUM VITAE

Hong Qi

Place of birth: Rushan, Weihai, Shandong, China

EDUCATION

University of Wisconsin - Milwaukee Ph.D. in Physics, expected in May 2018 Thesis advisor: Patrick Brady	Aug 2011 - present
National Astronomical Observatories of China M.Phil. in Astrophysics Advisor: Da-Ming Chen	Sep 2008 - Jun 2011
Beijing University of Aeronautics and Astronautics B.E. in Space Engineering	Sep 2003 - Jul 2007

COLLABORATIONS

LIGO Scientific Collaboration full member since 2015
Global Relay of Observatories Watching Transients Happen (GROWTH) full member since 2016

SELECTED AWARDS

Special Breakthrough Prize in Fundamental Physics and a share of \$3,000,000: awarded as a contributor in the LIGO Scientific Collaboration to the first direct detection of gravitational waves 2016
First Prize in National Mathematical Olympiad Competition of China: elementary school level and won by mostly self studying 1995

SHORT AUTHOR LIST PUBLICATIONS

Determining the Hubble Constant with both Gravitational-wave and Electromagnetic Observations, in preparation
Hong Qi, Chris Pankow, Patrick Brady

Constraining Relativity and Astrophysics with Galactic Center Stellar Orbits: Calibrated against a Fisher Matrix Method, to be submitted to Phys. Rev. D
Hong Qi, Richard O'Shaughnessy, Patrick Brady

Testing Chameleon Field Theory with Cepheids in Extragalactic Dwarf Galaxies, to be submitted to ApJ
Hong Qi, Philip Chang

Analysis Framework for the Prompt Discovery of Compact Binary Mergers in Gravitational-wave Data, Phys. Rev. D 95, 042001, 2017
Cody Messick, Kent Blackburn, Patrick Brady, Patrick Brockill, Kipp Cannon, Romain Carriou, Sarah Caudill, Sydney J. Chamberlin, Jolien D. E. Creighton, Ryan Everett, Chad Hanna, Drew Keppel, Ryan N. Lang, Tjonnie G. F. Li, Duncan Meacher, Alex Nielsen, Chris Pankow,

Stephen Privitera, Hong Qi, Surabhi Sachdev, Laleh Sadeghian, Leo Singer, E. Gareth Thomas, Leslie Wade, Madeline Wade, Alan Weinstein, Karsten Wiesner

The effects of BCGs on the Statistics of Large-separation Lensed Quasars by Clusters, RAA, Vol. 11, No. 9, 2011

Hong Qi, Da-Ming Chen

LONG AUTHOR LIST PUBLICATIONS

<http://arxiv.org> : 443/find/astro-ph/1/au:+Qi_H/0/1/0/all/0/1

SELECTED CONFERENCES AND SEMINARS

LSC-Virgo March 2018 meeting at Sonoma State University Mar 18 - 23, 2018

Determining the Hubble Constant with Both Gravitational-wave and Electromagnetic Observations

· Department of Physics Seminar at UW-Milwaukee Nov 17, 2017

· American Physical Society April Meeting in Washington DC Jan 27 - 31, 2017

· Midwest Pre-O2 Preparation Meeting at Northwestern University Jun 2016

Constraining Relativity and Astrophysics with Galactic Center Stellar Orbits

· Department of Physics Seminar at UW-Milwaukee Apr 1, 2016

LSC-Virgo March 2016 meeting at Caltech Mar 13 - 19, 2016

Open-box Result Report of Gravitational Wave Offline Searches Based on Analysis of 16 Days of Data of O1 Run 4

· LIGO Compact Binary Coalescence Group Weekly Meeting Nov 2015

LSC-Virgo March 2015 meeting at Caltech Mar 15 - 20, 2015

The 23rd Midwest Relativity Meeting at UW-Milwaukee Oct 25 - 26, 2013

TEACHING EXPERIENCE

Teaching Assistant, General Physics Laboratory II (Non-Calculus Treatment) Summer 2012

Teaching Assistant, General Physics I, II (Non-Calculus Treatment) Falls 2012 to 2014, Springs 2013 & 2017

Teaching Assistant, General Physics I, II (Calculus Treatment) Falls 2011 & 2017, Springs 2012 & 2018

SELECTED OUTREACH ACTIVITIES

First Detection of Binary Neutron Star Merger: CSA talk in Milwaukee Nov 2017

My Participation in First Detection of Gravitational Waves: Invited public science talk to retired researchers in Chinese Academy of Sciences in Beijing Apr 2016

First Direct Detection of Gravitational Waves: Coffeeshop Astrophysics (CSA) public science talk with hundreds of audiences in Milwaukee Feb 20, 2016

Supermassive Black Holes: Public science talk at the UWM Manfred Olson Planetarium Apr 2015

UW-Milwaukee Astronomy Club Activities 2011 - 2014